UNIVERSITÀ DEGLI STUDI DI PADOVA

Dipartimento di Fisica e Astronomia "Galileo Galilei"

Master Degree in Physics

Final Dissertation

3D Plasma-Wall Interaction in the RFX-mod device

Thesis supervisor
Dr. Matteo Zuin
Thesis co-supervisors
Dr. Gianluca Spizzo
Dr. Lionello Marrelli

Candidate
Pasquale Porcu

Academic Year 2021/2022

Abstract

This thesis is devoted to the characterisation of the plasma instabilities causing the Plasma Wall Interaction (PWI) observed during a high current discharge by the Optical Camera System in the RFX-mod reversed field pinch (RFP) device, operated by Consorzio RFX in Padova, Italy. The PWI shows two distinct stripes of neutral carbon radiation on the internal graphite wall of the device. The main goal is to simulate and understand the origin of the pattern.

The topic is not specific to the RFP configuration, but is is studied in perspective of ITER, the nuclear fusion experimental reactor which is under construction in Cadarache, south of France. The complicate 3D topology of the plasma which gives birth to the PWI in the case study is investigated via the Hamiltonian guiding center code ORBIT .

A preliminary analysis with a simplified model of 3D topology shows that the maximum toroidal mode number of plasma instabilities involved in the PWI event is higher than the measured $n \leq 23$. This information is important in view of the refurbished RFX-mod2 device.

Further analysis is performed with ORBIT and regards the description of the map of connection lengths to the wall. This map qualitatively reproduces the experimental PWI pattern on the surface of the RFX-mod wall. Finally, it shows that the two stripes of the PWI, represented by low connection lengths, are caused by modes with different poloidal number, $m = 0$ and $m = 1$.

Contents

Introduction

In the current economic scenario characterised by the crisis of the traditional electric energy supply system, the research of new energy sources is continuously expanding. Nuclear fusion reactions represent a possible way to get a huge amount of energy, potentially available for people and factories, with a small environmental footprint.

Since 1950s, several efforts were invested to make fusion a commercial source of energy. Presently, such a goal has not yet been achieved. The major international project finalised at building a commercial fusion reactor is represented by ITER (which stands for *International Thermonuclear Experimental Reactor*) which is currently under construction in Cadarache (France) and whose operations are going to start by December 2025. ITER is a prototype for the creation of the first fusion reactor, DEMO (which stands for *DEMOnstration power plant*), which will be the first plant for commercial purposes and will start operating likely by the end of 2050s. Indeed, the main aim of ITER is to demonstrate that it is possible to realise in laboratory a reproducible and relatively long-lasting controlled nuclear fusion process with a sufficiently high energy gain. On the other hand, the DEMO reactor is designed even to double the energy gain of ITER!

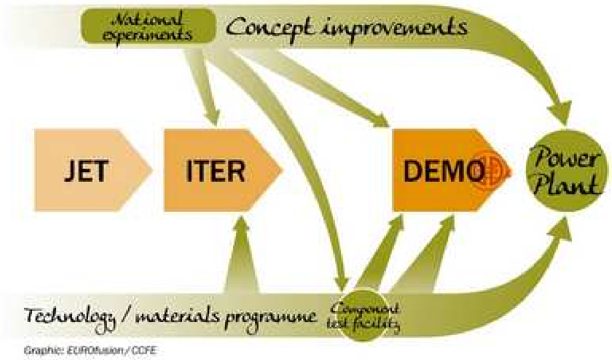

Figure 1: Path from ITER to DEMO. Picture taken from Ref. [1].

Both ITER and DEMO employ the Tokamak magnetic configuration which presently shows the best performance in terms of particle and energy confinement. However, this is not the only available configuration. For example, the Consorzio RFX, located in the area of the Italian National Research Council (CNR) in Padova, Italy, hosts the largest fusion experiment in the world which operates in an alternative configuration, i.e. the Reversed Field Pinch (RFP). Its name is RFX-mod[1], and operated between 2004 and 2015. It consists of a doughnut-shaped chamber (geometrically a torus) with major radius $R_0 = 2$ m and minor radius $a \approx 0.46$ m. Since, this configuration is more compact than a tokamak, the RFP is favored in terms of size and cost. RFX-mod is currently being upgraded and will start operating by the end of 2024.

---

[1] To be precise, RFX-mod's peculiar versatility lets to exploit both Tokamak and RFP configurations. However it works mostly in RFP.

The work presented in this thesis summarises my activity at Consorzio RFX. It was devoted to the study of the impact of tearing modes on Plasma Wall Interaction (PWI) in RFX-mod. The number of tearing modes determining the PWI can change during a plasma discharge. By changing some experimental parameters of the discharge, a situation where there is a dominant tearing mode is observed. In this case, the state of the plasma is described as the ordered *Quasi-Single Helicity* (QSH) state. The QSH is often interrupted by a more chaotic state called *Multiple Helicity* (MH) which is characterised by a broad spectrum of tearing modes. Both in MH and QSH states, the tearing modes tend to align their phases due to non-linear coupling. This condition is called *Locked Mode* (LM), which is observed to be detrimental to magnetic confinement, since it is responsible for a large loss of particles towards the Plasma Facing Components (PFC) of the device, resulting eventually in their damage. Such an event is called *Plasma Wall Interaction* (PWI). More details on the phase locking of tearing modes are given in Chapter 3.

My work was focused on a specific PWI event, whose image was taken with a CCD camera during the RFX-mod experimental campaign, in the discharge #29324 at time $t_{PWI} = 218$ ms**. Therefore, the major goal has been to estimate which modes were more detrimental in generating such PWI**.

For this purpose, several approaches, like the calculation of the magnetic field lines displacements induced by the instabilities, and the description of the plasma magnetic topology both perceived with the ORBIT guiding center code [2] are discussed. In particular, an useful quantity, namely the *Connection Length to the wall*, $L_{c,w}$, has been calculated with ORBIT. $L_{c,w}$ of a given point A is defined as the distance which is traveled by a single charged particle starting from A to hit the first wall, formally:

$$L_{c,w} = \int_{\zeta_A}^{\zeta_w} \frac{B \, \mathrm{d}\zeta}{\vec{B} \cdot \nabla \zeta} \,, \tag{1}$$

where ζ_A and ζ_w represent the initial and final toroidal angles, respectively. This quantity is discussed more in detail in the second Chapter of the thesis, in Section 2.2.3. Particles causing a larger PWI in the RFP are characterised by shorter connection lengths. Therefore, the map of $L_{c,w}$ is expected to follow the pattern of PWI.

The topic of the thesis is not specific to the RFP configuration only. In fact, in the tokamak magnetic perturbations, called RMPs, are imposed by external means to reduce the impact on the PFC of more violent instabilities, called *Edge Localised Modes* (ELMs). The latter are present due to high pressure gradients which often arise in this configuration. Tokamak like ITER can tolerate a limited number of these events. Then, inducing RMPs represent an efficient way to mitigate the effects of such disruptive perturbations. Therefore, the analysis of the way these magnetic perturbations interact to determine particle transport is also in perspective of ITER.

The main property of the non-linear interaction of perturbations, both in tokamaks and RFPs is that it creates regions of magnetic chaos in the plasma. This mechanism reduces large pressure gradients driving ELMs in tokamaks. On the contrary, in the RFP, the ordered QSH is to be preferred to the chaotic MH state since it is characterised by a smaller PWI. The 3D structure of these chaotic regions is investigated by mapping the Connection Length to the wall.

In this thesis, the first two Chapters summarise the context and methods used in the thesis. Starting from Chapter 3, the main original results coming from my analysis are pointed out. The outline is as follows:

- **Chapter 1** describes the basics of a fusion reactor, such as the reaction energy balance and the need for magnetic confinement of charged particles. The plasma equilibrium condition and the instabilities perturbing this state are treated in the framework of the *Magnetohydrodynamics* (MHD), which is a common tool for describing both Tokamak and the RFP configurations.

- In **Chapter 2** a brief description of the RFX-mod experimental setup is pointed out. The major interest is reserved to the *Optical Camera System* (OCS) which hosted the CCD cameras observing the PWI's during the discharge # 29324. The guiding center ORBIT code, which was used for the $L_{c,w}$ calculations, is also briefly discussed.

- **Chapter 3** reports the PWIs description which is based on the comparison between the profile of the ideal displacements of magnetic field lines induced by tearing modes and the toroidal profile of a parameter that quantifies how much the modes are aligned during the Locked Mode, the so-called *Locking-Strength* (LS). A preliminary estimate of the number of modes that were involved in the PWI of interest is provided.
- **Chapter 4** deals with a description based on the characterisation of the plasma magnetic topology during the PWI event of interest by exploiting its representation on a *Poincaré plot*. Some information about which kind of magnetic perturbations have led to the PWI of interest is deduced.
- Finally, **Chapter 5** regards the analysis of the $L_{c,w}$ maps. A further understanding of the phenomenology resulting in the PWI of interest, coming from the comparison between such maps and the image of the PWI taken on camera, is reported.

The thesis ends with a final section of concluding remarks.

Chapter 1

Main aspects of Nuclear Fusion

In this Chapter, a detailed summary of the main concepts to be taken into account in order to successfully exploit nuclear fusion reactions as a commercial energy source are described. Some topics, such as the problem of the energy balance inside a reactor and particle confinement are underlined. The role of magnetic instabilities is further discussed and investigated. A brief theoretical description of the MHD model of tearing modes is also provided, to describe the framework in which the research activity has been carried out.

1.1 The thermo-nuclear fusion reactions

1.1.1 Definition of plasma

Ordinary fluids such as air or water are made by electrically neutral molecules and atoms. Though, by heating a gas to very high temperatures or by passing an electric discharge through it, one in principle can reach a configuration where atoms have been ionised into positively charged nuclei and negatively charged electrons. Such a collection of ions and electrons is called *plasma*. Though, everyday life phenomena, like flames or thunders are made of plasma, plasma is not very common in our daily life. On the contrary, it pervades the universe outside the Earth. For example, shining stars are made by gas heated at high temperatures, so nothing but plasma!

From a phenomenological point of view, a plasma can be simply described as a special kind of fluid which is globally neutral and whose particles are electrically charged and interact with each other through Coulumb's force.

1.1.2 The binding energy per nucleon

The mechanism that powers the stars is led by the *thermo-nuclear fusion reaction*. It is a process where two atomic nuclei join into a heavier nucleus, forming a new element.

The probability to make two nuclei bind together through fusion can be predicted simply with energetic considerations. In fact, each nucleus is composed of a certain number of protons and neutrons which are held together by the nuclear force. Therefore, given a nucleus having a mass M, and made of Z protons and $A - Z$ neutrons, its *binding energy* is defined in this way:

$$E_B = Zm_p + (A - Z)m_n - M \ , \tag{1.1}$$

where m_p and m_n represent respectively the mass of a proton and that of a neutron. Notice that the definition of the binding energy reported in Eq. (1.1) implies that the most stable elements are those which maximise E_B. The binding energy of a certain nucleus can be predicted in the framework of the Liquid Drop Model (LDM) and it can be experimentally measured. Its trend depending on the mass number A is shown in Fig. 1.1.

Therefore, the energy gain related to a general nuclear reaction is quantified as the difference between the sum of the binding energies of the reactants and that of the binding energies of the products, namely:

$$E_{\text{released}} = E_B^{\text{reactants}} - E_B^{\text{products}} \ . \tag{1.2}$$

E_{released} represents the amount of energy that is freed at the end of the reaction as kinetic energy of its products, so the condition to be fulfilled to say a reaction convenient is that E_{released} must be positive.

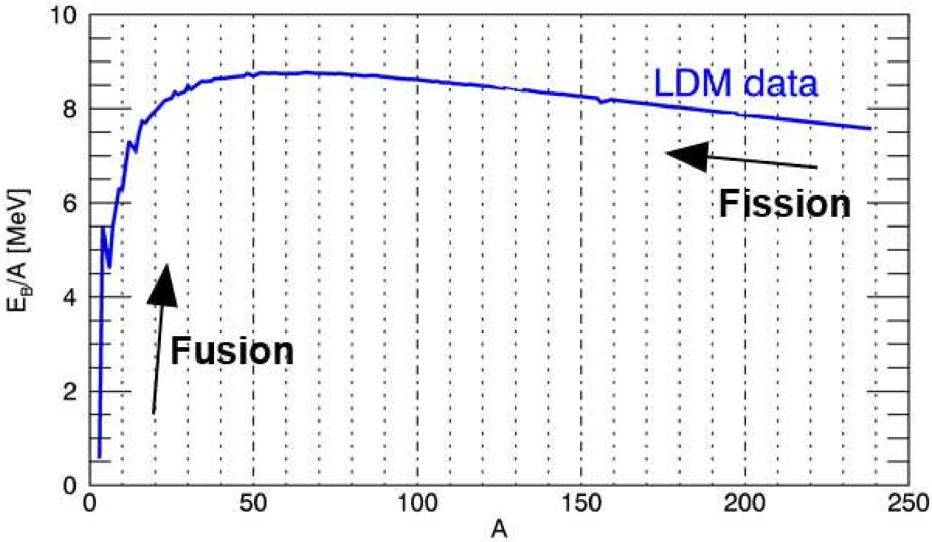

Figure 1.1: Trend of the binding energy per nucleon as a function of the atomic mass number A. The arrows represent the direction that nuclei involved in nuclear fusion and fission reactions follow to reach more stable states. Data are taken from Ref. [3].

Since the binding energy has its maximum at $A = 56$, corresponding to the ^{56}Fe peak, there are two opposite ways to get energy from a nuclear reaction: *fusion*, from light nuclei to a heavier one and *fission*, from a heavy nucleus to lighter ones.

In principle, the energy released by a single nuclear reaction can be collected and properly converted into electric energy for commercial purposes. However, it is a very difficult task and it has not been achieved with fusion yet. This is the reason why, at the moment, fission represents the only way to produce energy by exploiting nuclear reactions. One of the most exploited fission reactions is the following [4]:

$$^{235}_{92}\text{U} + \text{n} \quad \longrightarrow \quad ^{140}_{58}\text{Ce} + ^{94}_{40}\text{Zr} + 2\text{n} + 6\text{e}^- + 206 \text{ MeV} \ , \tag{1.3}$$

where, at the end of the formula, the amount of released energy (E_{released}) from a single reaction is reported. The fission reaction written above has two main advantages. Firstly, while it takes only one neutron to start, at the end two neutrons are produced. This implies that in principle a chain reaction is triggered, making the fission reactor self-sustaining for a long time before it needs to be refueled. The second advantage is linked to the fact that the reaction is started with a neutral particle, so it is relatively easy to overcome the electron barrier surrounding the heavy nucleus that makes start the reaction.

On the other hand, the main lack of exploiting nuclear fission processes as a source of energy is the production of long-lasting radioactive waste which requires special storage for a practically infinite time.

1.1.3 The D-T fusion reaction

As previously mentioned, exploiting fusion reactions is possible as long as one can overcome the energy barrier related to the nuclear force binding nucleons together. These conditions are fulfilled by heating fuel at a very high temperature, namely producing a plasma. Therefore, a fusion reactor can be considered as a device which contains a plasma and employs the fusion reactions which occur inside to generate a, possibly positive, energy output. Such a operation is also called *discharge*[1].

In order to exploit controlled nuclear fusion, the reactions commonly taken into account are the following:

- $\mathrm{D + D \quad \longrightarrow \quad T + p + 4.03\ MeV}$;
- $\mathrm{D + D \quad \longrightarrow \quad {}^3He + n + 3.27\ MeV}$;
- $\mathrm{D + T \quad \longrightarrow \quad {}^4He + n + 17.6\ MeV} \qquad (\star)$;
- $\mathrm{D + {}^3\,He \quad \longrightarrow \quad {}^4He + D + 18.3\ MeV}$.

where D indicates the deuterium hydrogen isotope, ^{2}H, whose nucleus is made of one proton and one neutron. Whereas T represents tritium, ^{3}H, i.e. the hydrogen isotope whose nucleus counts one proton and two neutrons.

Practically speaking, the convenience of a certain reaction with respect to the others is determined by three factors: the probability that the reaction has to happen, the reactants' abundance in nature, and the amount of energy that is released at the end of the reaction. Based on the latter criterion, on the Earth the two most convenient reactions are the last two. Moreover, looking at the trend of the cross-section σ of the reactions as a function of the deuterium reactant kinetic energy, $K_D = \frac{1}{2} m_D v_D^2$ (the graph is reported in Fig. 1.2), one can conclude that the most convenient reaction among those reported above is represented by the D-T one. This is the reason why it is signaled with the $(\star)$ symbol above. A scheme of the D-T reaction is sketched in Fig. 1.3.

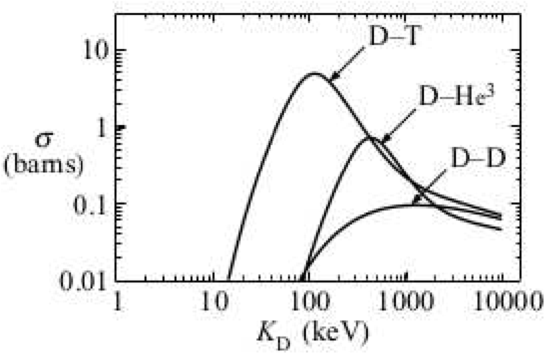

Figure 1.2: Experimentally measured cross-sections for the D-T, D-^{3}He, and D-D fusion reactions as a function of deuterium energy K_D [5].

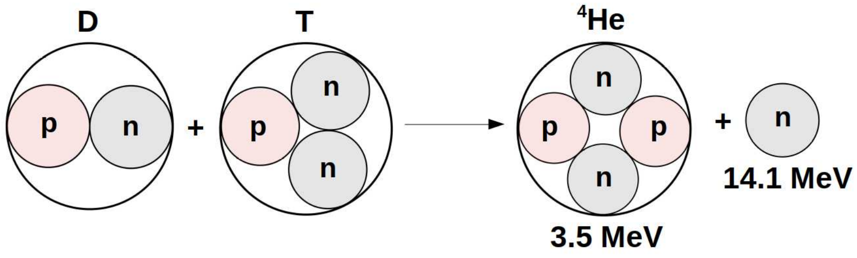

Figure 1.3: In a D-T fusion reaction, a nucleus of deuterium and another nucleus of tritium combine to form an α-particle (namely a nucleus of ^{4}He) with a kinetic energy of 3.5 MeV. In the reaction also a neutron with an energy of about 14.1 MeV is freed. The total energy released in the reaction is thus 17.6 MeV.

The same graph in Fig. 1.2 also shows that the cross-section of the D-T reaction is sufficiently high only for $K_D > 10$ keV. This means that, in principle, a fusion reactor requires high temperatures (around 25 keV) to deliver a sufficient amount of D-T reactions.
Exploiting fusion as a source of energy shows three main advantages [6]: fuel reserves, environmental

---

[1] In this thesis, a single discharge of the RFX-mod device is going to be call also *shot* since its typical duration is 'only' of about ≈ 0.5 s.

impact, and safety. Regarding the first one, there is one deuterium for every 6700 hydrogen atoms. This means that it can be easily extracted, for example from ocean water where it occurs naturally. Instead, tritium is obtained by breeding reactions with the lithium isotope ^{6}Li:

$$^6\mathrm{Li} + n \quad \longrightarrow \quad \mathrm{T} + {}^4\mathrm{He} + 4.8\ \mathrm{MeV}\ . \tag{1.4}$$

The overall reserves of fuel for a D-T fusion reactor are thus limited by the reserves of lithium. But new alternative materials, such as beryllium or lead, to get tritium are being studied [7].

The next advantage regards the environmental impact of fusion. During their activity, fusion reactors do not emit CO_2 or other harmful chemicals into the atmosphere. Instead, from the ecological point of view, the most challenging issue is that concerning the disposal of the blanket surrounding the reactor. In fact, as it has been already mentioned, at the end of the D-T reaction a neutron is released. The major purpose of the blanket is to screen the environment outside the reactor from all the neutrons which come from the reactions by exploiting the same process in Eq. (1.4), so producing tritium meanwhile. As a consequence, the blanket is made mostly of lithium. Since the freed neutrons are very energetic (their energy is about 14 MeV), they cause the structure to become activated. However, these radioactive structural materials have a short lifetime, of the order of 100 years, so they can be more easily stored than those produced with fission. Overall, considering the entire environmental situation, fusion is a very reliable option with respect to other energy sources currently exploited for commercial purposes such as oil, carbon, or the renewable sources too.

The last worthy advantage involves safety. All the fusion reactions reported above do not imply the possibility to form a chain reaction. This means that the reactor requires to be filled almost continuously during its operations. From the safety point of view this implies that, despite what happens in fission, a fusion reactor activity can be stopped immediately if some damage is eventually present. In other words, the possibility of a meltdown is null for a fusion reactor.

1.2 Main features of a fusion reactor

1.2.1 The energy balance

Taking into account the main sources of energy gain and loss, it is possible to approximately predict the operational conditions of a fusion reactor. A precise analysis of this topic can be found in Ref. [8]. Consider a fusion plasma, fully ionised ($n_i = n_e$) and at thermal equilibrium. The power per unit of volume, p_f, released from each one of all the D-T fusion reactions which happen inside the reactor is given by:

$$p_f = n_D n_T \langle \sigma v \rangle E_f\ , \tag{1.5}$$

where n_D and n_T represent respectively the numerical density of deuterium and tritium nuclei in the reactor. E_f is the total energy released during a single reaction, namely $E_f = 17.6$ MeV. $\langle \sigma v \rangle$ is called *reactivity* and is calculated by averaging over the velocities the product between the cross-section, σ, and the relative velocity, v, of two colliding plasma particles, i.e.:

$$\langle \sigma v \rangle = \int_\Omega d^3 v_1 \int_\Omega d^3 v_2\ \sigma(v) v \cdot f_1(v_1) f_2(v_2)\ , \tag{1.6}$$

where v_1 and v_2 represent the velocities of the two particles, and f_1, f_2 are the corresponding distribution functions.

It can be shown that the power p_f is maximised when deuterium and tritium are equally present inside the reactor, i.e. $n_D = n_T = \frac{n}{2}$. In this case, the maximum released power density is given by:

$$p_f^{max} = \frac{1}{4} n^2 \langle \sigma v \rangle E_f\ . \tag{1.7}$$

Since particles are at thermal equilibrium, the mean kinetic energy of a single particle is expressed by $\frac{3}{2}T$, according to the ideal gas law. Therefore, the total kinetic energy per unit of volume of the system, w, is obtained by multiplying the last quantity by $2n$:

$$w = 3nT\ . \tag{1.8}$$

The time evolution of w is expressed with the following power balance:

$$\frac{dw}{dt} = p_H + p_\alpha - p_L - p_R \ . \tag{1.9}$$

On the right-hand side, several contributions of power are reported: p_H is a positive contribution to the energy given with external heating. In a modern reactor, several sources are employed to heat plasma during the discharge, the most used are the Ohmic effect, which is always present, the Radio Frequency Heating, and the Neutral Beam Injection (NBI). The last two are also called *additional* or *external heating sources*. p_α is another positive contribution of energy coming from the α-particles which are produced by each D-T reaction, in the hypothesis that all α-particles remain confined in the reactor. An expression for p_α can be derived by analogy with the Eq. (1.7):

$$p_\alpha = \frac{1}{4} n^2 \langle \sigma v \rangle E_\alpha \ , \tag{1.10}$$

where $E_\alpha = 3.5$ MeV is the kinetic energy of the α-particle at the end of the D-T reaction. p_R is a loss term corresponding to the energy that is radiated out from the plasma, most of this power comes from bremsstrahlung phenomena and it is expressed with the following phenomenological formula [9]:

$$p_R \approx p_b = \alpha_b n^2 T^{\frac{1}{2}} \ , \tag{1.11}$$

where $\alpha_b = 5.35 \cdot 10^{-37}\ \mathrm{Wm^3/keV^{\frac{1}{2}}}$ is a constant. Finally, p_L is a loss term related to the conduction and convection phenomena. In order to quantify this contribution of power, it is convenient to make use of a phenomenological parameter called *energy confinement time*, τ_E, which is defined in this way:

$$p_L = \frac{w}{\tau_E} \ . \tag{1.12}$$

If ideally one considers to *isolate* the fusion plasma, i.e. to switch off all contributions of energy gain and losses, $p_H = p_\alpha = p_R = 0$, Then the Eq. (1.9) becomes:

$$\frac{dw}{dt} = -\frac{w}{\tau_E} \ . \tag{1.13}$$

Namely, τ_E represents the time a fusion plasma survives whenever it is isolated.

1.2.2 The ignition condition

The term *ignition* is used to define the ideal situation when the power p_α coming from fusion reactions balances all the losses. Therefore, in such a situation, the plasma does not need any external heating, but autonomously guarantees the activity of the reactor:

$$p_\alpha > p_L + p_R \qquad \Leftrightarrow \qquad p_H = 0 \ . \tag{1.14}$$

By substituting the ignition condition (1.14) inside the definition of the energy confinement time in Eq. (1.12), one obtains:

$$\tau_E > \frac{w}{p_\alpha - p_R} \ . \tag{1.15}$$

By making explicit $w = 3nT$ at the numerator, and by substituting the expressions for p_α and p_R (taken respectively from Eq. (1.10) and Eq. (1.11)), the ignition condition can be finally written in the following form:

$$n\tau_E > \frac{12T}{\langle \sigma v \rangle E_\alpha - 4\alpha_b T^{\frac{1}{2}}} \ . \tag{1.16}$$

The trend of the $n\tau_E$ product for the D-T reaction as a function of the temperature T is shown in Fig. 1.4. It has a minimum close to $T = 25$ keV. The requirement for ignition at this temperature is:

$$n\tau_E > 1.5 \cdot 10^{20}\ \mathrm{m}^{-3}{\cdot}\mathrm{s}\ . \tag{1.17}$$

However, since τ_E is itself a function of the temperature, for practical reasons it is better to write the ignition requirement as a product of n, τ_E, and T. In the temperature range $10 - 20$ keV, the reactivity is well represented with the approximation:

$$\langle \sigma v \rangle = 1.1 \times 10^{-24} \cdot T^2_{[\mathrm{keV}]}\ \mathrm{m}^3{\cdot}\mathrm{s}^{-1}\ . \tag{1.18}$$

Taking into account $E_\alpha = 3.5$ MeV, the ignition condition thus becomes:

$$nT\tau_E > 3 \cdot 10^{21}\ \mathrm{m}^{-3}{\cdot}\mathrm{keV} \cdot \mathrm{s}\ . \tag{1.19}$$

This is a very convenient form to represent the ignition condition since it brings out explicitly the requirements on density, temperature, and confinement time to build an efficient fusion reactor. In other words, it claims that, in order to make a fusion reactor properly work in a regime of positive energy output, one needs to put enough fuel for a sufficiently long time, and heated at a sufficiently high temperature. The condition would be reached for example with $n = 10^{20}$ m^{-3}, $T = 10$ keV and $\tau_E = 3$ s.

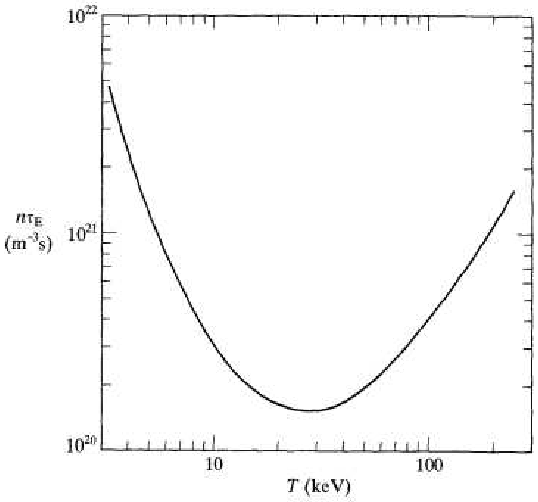

Figure 1.4: Trend of $n\tau_E$ fulfilling the ignition condition in Eq. (1.16) as a function of the plasma temperature T for the D-T reaction [10].

1.2.3 The overall energy gain

The fusion reactor's ability to have a positive energy balance is actually measured with the ratio between the total power obtained from fusion reactions during the discharge, P_f, and that used to heat the plasma inside the reactor during the same time, P_H. Namely:

$$Q = \frac{P_f}{P_H} = \frac{5P_\alpha}{P_H}\ , \tag{1.20}$$

where the last passage is justified considering that, in a single D-T reaction, the total released energy is 5 times the kinetic energy of the α-particle which is produced. The condition $Q = 1$ is called *break-even condition*, it refers to the situation when the reactor gives back the same energy that is required for the plasma sustainment. In the ignition regime, $P_H = 0$, so $Q \longrightarrow +\infty$.

The highest Q ever reached is 1.25, with the Japanese Tokamak JT-60U in 1999 [11]. However, it is not enough to make commercial use of the energy produced through fusion processes. One of the major goals of ITER is indeed to achieve the value $Q = 10$ and possibly to overcome it. The first commercial fusion reactor, DEMO, should reach even higher levels of Q.

1.3 Magnetic confinement of charged particles

1.3.1 Towards the modern helical transform configuration

As already underlined in Eq. (1.19), in order to trigger a sufficient number of D-T fusion reactions, particles should be confined for a reasonably long time, at a sufficiently high temperature, in a high-density condition. A possible way to solve this issue is to employ the magnetic field.

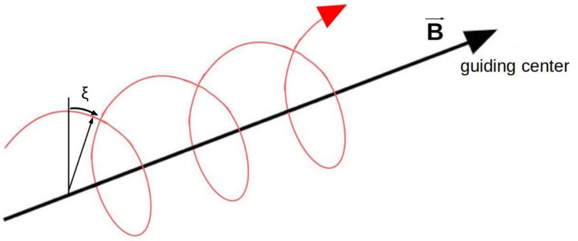

Figure 1.5: A charged particle immersed in a magnetic field draws a spiral around the magnetic field line. ξ is the so called gyro-phase.

Magnetic confinement is based on the principle that a charged particle immersed in a magnetic field, draws a spiral around the magnetic field line, see Fig. 1.5. The center of the circular orbits is known as *guiding-center* [12]. The radius, ρ, of the circular trajectory drawn by the particle with charge e on the plane that is perpendicular to the field line is historically known as *Larmor radius*[2], and it arises from the equilibrium between the Lorentz force and the centrifugal force:

$$ev_\perp B = \frac{mv_\perp^2}{\rho} \qquad \Rightarrow \qquad \rho = \frac{mv_\perp}{eB} \ , \tag{1.21}$$

where $v_\perp$ is the component of the particle velocity which is perpendicular to the magnetic field $\vec{B}$, $|q|$ is the modulus of its charge, and m indicates its mass. The frequency of such a circular motion around the magnetic field line is said *cyclotron frequency* and it is calculated as: $\omega_c = \frac{v_\perp}{r_L} = \frac{eB}{m}$.
A particle is said *confined* if its Larmor radius is smaller than the space available for its motion. Vice versa it is said *lost*.

The simplest magnetic configuration that can be possibly used to confine charged particles is represented by the solenoid. In this way, particles are constrained to do a circular motion perpendicularly to the magnetic field. However, in this device they are still lost in the parallel direction. A possible solution might be to increase the intensity of the magnetic field at the edges of the solenoid, as it is shown in Fig. 1.6. In fact, it can be easily shown that such a configuration works as a *magnetic mirror* for most of the particles. Indeed, even in this case, some particles are still lost, especially those that move quickly enough along the direction parallel to the magnetic field. Then, the most effective approach to avoid these longitudinal losses is to close the magnetic field lines on themselves, forming a sort of doughnut, geometrically called a torus. The simplest way to realise such a spatial configuration of the magnetic field is to use coils placed so as to form a toroidal solenoid[3].

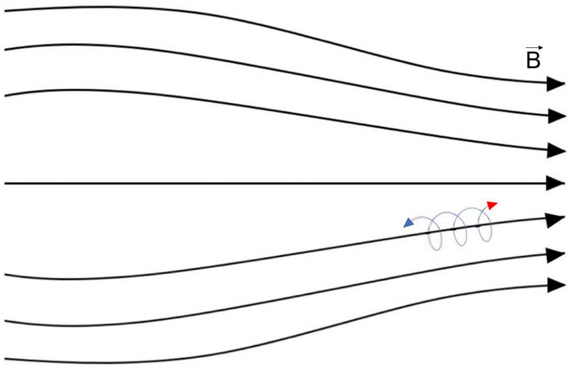

Figure 1.6: Sketch of the magnetic mirror configuration. The magnetic field is represented in black. The particle turns around the magnetic field line following the red orbit. Then, it bounces due to the increase of the magnetic field at the edge. The bounced particles come back following the same trajectory (coloured in blue) but in the opposite direction.

---

[2] Alternatively, it can be called also as *cyclotron radius* or *gyro-radius* A more formal introduction to this quantity is going to be reported in the next Chapter.

[3] As concerns the notation, it is going to be called *toroidal* ($\hat{\varphi}$) the direction which turns around the major axis of the torus, Whereas *poloidal* ($\hat{\theta}$) is going to identify the direction that turns around its minor axis. The minor radius coordinate is going to be indicated with $\hat{r}$.

Inside a torus, the magnetic field decays as $\frac{1}{R}$ where R represents the distance from its center. It can be demonstrated simply by using Ampére's law. It can be shown that, if the magnetic field has a gradient, then it is responsible for a guiding center drift. Its velocity thus would be given by:

$$\vec{v}_d = \frac{mv_\perp^2}{2qB} \cdot \frac{\vec{B} \times \nabla B}{B^2} + \frac{mv_\parallel^2}{qB} \cdot \frac{\vec{R}_c \times \vec{B}}{R_c^2 B} \ . \tag{1.22}$$

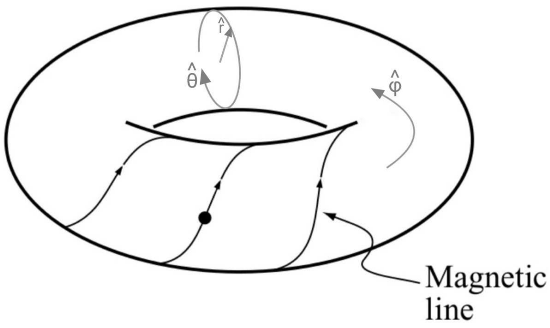

Figure 1.7: Sketch of the helical transform of the magnetic field. Toroidal and poloidal directions are respectively indicated with $\hat{\varphi}$ and $\hat{\theta}$. $\hat{r}$ indicates the radial direction. Adapted from Ref. [13].

In the formula above, $\vec{R}_c$ indicates the curvature radius of the magnetic field. As a convention, the direction towards the outer part of the torus is taken positively. The overall effect of this velocity in the geometrical case of a torus is a vertical drift of particles. Since $\vec{v}_d$ depends on the sign of the particle's charge, we have that electrons and ions are separated with this drift. Therefore, an electric field is generated. This field is responsible for another contribution of velocity:

$$\vec{v}_{E\times B} = \frac{\vec{E} \times \vec{B}}{B^2} \ . \tag{1.23}$$

In principle, such a separation of charges could be detrimental for the plasma survival. Therefore, this problem needs to be solved by introducing a new component of the magnetic field along the poloidal direction. The overlap of the toroidal (B_φ) and the poloidal (B_θ) components gives birth to a magnetic configuration where the magnetic field lines wind helically around the torus as shown in Fig. 1.7. In other words, the magnetic field undergoes to the so-called *helical transform.* The resulting guiding center orbit becomes helical itself. In fact, the trajectory designed by each particle of the plasma performs a certain number of turns around both the toroidal and the poloidal directions.

To conclude, a magnetically confined device is a toroidal vacuum chamber. Its typical dimensions are of the order of magnitude of a meter regarding major (R_0) and minor (a) radii. A useful parameter to describe the reactor geometry is the so-called *aspect-ratio*, which is defined as $A = R_0/a$.

1.4 Plasma equilibrium

1.4.1 Plasma dynamical theory

In the *Magneto-Hydro-Dynamics* (MHD) approach, the plasma is considered as a fluid made up of charged particles, called *magnetofluid.* As a consequence, in the MHD model, a full dynamical theory for plasma is provided by considering the conservation equations for neutral fluids which come out from the collisional Boltzmann's equation and then, by adding the Maxwell's equation (in the non-relativistic approach) for the electric ($\vec{E}$) and the magnetic ($\vec{B}$) fields:

$$\frac{\partial \rho_m}{\partial t} + \nabla\left(\rho_m \vec{v}\right) = 0 \ ; \tag{1.24}$$

$$\frac{\partial \vec{v}}{\partial t} + \left(\vec{v} \cdot \nabla\right) \vec{v} = -\frac{1}{\rho_m} \nabla p - \frac{\vec{F}}{m} + \nu \ \nabla^2 \vec{v} \ ; \tag{1.25}$$

$$\rho_m \left(\frac{\partial \varepsilon}{\partial t} + \vec{v} \cdot \nabla \varepsilon \right) - \nabla \cdot \left(K \ \nabla T\right) + p \ \nabla \cdot \vec{v} = 0 \ ; \tag{1.26}$$

$$\nabla \cdot \vec{E} = \frac{Q_{tot}}{\varepsilon_0} \qquad , \qquad \nabla \times \vec{E} = -\frac{\partial \vec{B}}{\partial t} \ ; \tag{1.27}$$

$$\nabla \cdot \vec{B} = 0 \qquad , \qquad \nabla \times \vec{B} = \mu_0 \vec{j} \ . \tag{1.28}$$

$\rho_m = mn$ is the mass density of the plasma, n is the numerical density of its particles, $\vec{F}$ represents the total external force acting on the system, ν is the viscosity. Furthermore, ε represents the internal energy of the system, while K is the thermal conductivity, and T is the temperature. Finally, as concerns Maxwell's equations, Q_{tot} is the total charge contained within the system, ϵ_0 is the vacuum dielectric constant, μ_0 is the vacuum diamagnetic constant, and $\vec{j}$ represents the electric current density.

By combining the equations reported above to get a full dynamical theory for plasma, one finally obtains the following set of equations, representing the local evolution of the most relevant quantities characterising the system, respectively the mass density ρ_m, the velocity $\vec{v}$, and the magnetic field $\vec{B}$:

$$\frac{\partial \rho_m}{\partial t} + \nabla\left(\rho_m \vec{v}\right) = 0 \ ; \tag{1.29}$$

$$\frac{\partial \vec{v}}{\partial t} + \left(\vec{v} \cdot \nabla\right)\vec{v} = -\frac{1}{\rho_m}\nabla\left(p + \frac{B^2}{2\mu_0}\right) + \frac{1}{\rho_m \ \mu_0}\nabla\left(\frac{B^2}{2}\right) + \nu \ \nabla^2 \vec{v} \ ; \tag{1.30}$$

$$\frac{\partial \vec{B}}{\partial t} = \nabla \times \left(\vec{v} \times \vec{B}\right) + \lambda \nabla^2 \vec{B} \ ; \tag{1.31}$$

where the quantity $\lambda = \frac{\eta}{\mu_0}$, with η the plasma resistivity, is called *magnetic diffusivity*. As a final remark, it is worth mentioning that the simplified version of the MHD equations where resistivity is assumed to vanish and $\eta = 0$ is called **ideal MHD**. This is a good, first-order approximation because a plasma is a very good electricity conductor.

1.4.2 The β parameter

In the MHD model framework, by considering a single charged particle in a plasma, the evolution in time and space of its linear momentum is well described with the Navier-Stokes equation, written for a charged particles system:

$$\frac{\partial \vec{v}}{\partial t} + \left(\vec{v} \cdot \nabla\right)\vec{v} = -\frac{1}{\rho_m}\nabla p + \frac{1}{\rho_m}\left(\vec{j} \times \vec{B}\right) + \nu \ \nabla^2 \vec{v} \ . \tag{1.32}$$

Assuming a condition of static equilibrium, the terms in $\vec{v}$ disappear and one finally obtains the so-called Grad-Shafranov equation:

$$\nabla p = \vec{j} \times \vec{B} \ . \tag{1.33}$$

The equation above makes explicit the balance between kinetic forces and magnetic forces in a magnetofluid at static equilibrium.

The plasma equilibrium is completely described through the following set of equations: the Grad-Shafranov equation (1.33), and the two Maxwell's equations for the magnetic field (1.28), which can be manipulated considering a cylindrical approximation, i.e. assuming to *straighten* the torus into a cylindrical shape[4]. In fact, by assuming cylindrical symmetry, i.e. $\frac{\partial}{\partial \theta} = \frac{\partial}{\partial z} = 0$, and that the plasma is at static equilibrium, i.e. $\vec{v} = 0$, the Eq. (1.30) becomes:

$$\frac{\partial}{\partial r}\left(p + \frac{B_\theta^2 + B_z^2}{2\mu_0}\right) + \frac{B_\theta^2}{\mu_0 r} = 0 \ . \tag{1.34}$$

The equation above represents the balance of the kinetic pressure, the magnetic pressure, and the magnetic tension for a cylindrical magnetofluid at static equilibrium. The first two contributions tend to push the magnetic field lines in the outside direction, instead the latter works to avoid their stretching.

---

[4] Passing from a toroidal to a cylindrical system of coordinates, the toroidal direction $\hat{\varphi}$ becomes the axial one $\hat{z}$.

Since, as we have already seen, magnetic confinement depends on the profile of the magnetic field line determining the helical transform, a suitable way to quantify its performance is to calculate the ratio between the average kinetic pressure and the magnetic pressure. This is the definition of the so-called *'beta' parameter*:

$$\beta = \frac{2\mu_0 \langle p \rangle}{B^2} \ , \tag{1.35}$$

where the average is meant to be calculated across the poloidal surface of the plasma.

1.5 Tokamak, Reversed-Field-Pinch and Stellarator

Depending on the amplitude of the toroidal and poloidal components of the magnetic field determining the helical transform for a modern fusion reactor, one can distinguish between several configurations for magnetic confinements. Presently, three are those most studied.

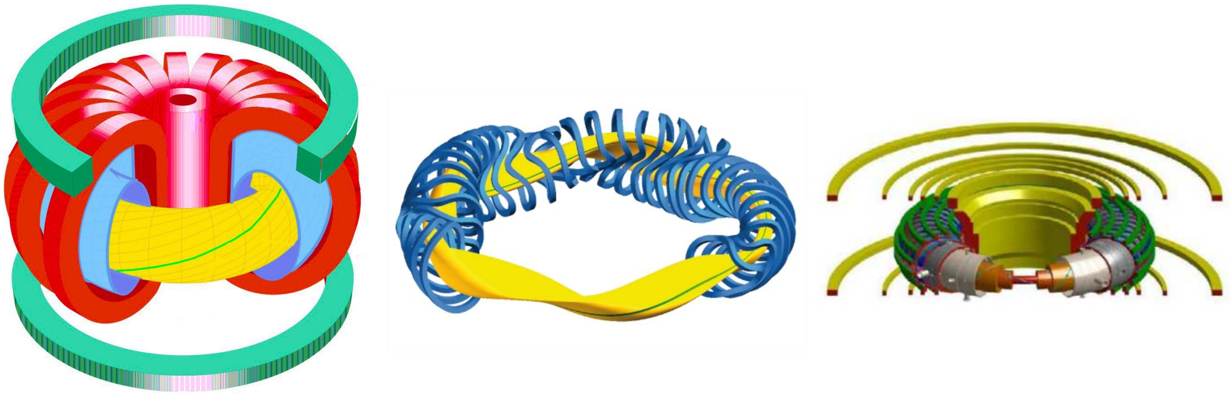

(a) Tokamak **(b)** Stellarator **(c)** Reversed-Field-Pinch

Figure 1.8: Comparison between the main confinement configurations available for a modern reactor.

The first one is the *Tokamak* (Fig. 1.8a). In this configuration, most of the magnetic field is in the toroidal direction ($B_\varphi \gg B_\theta$), and it is obtained thanks to a set of coils forming a sort of toroidal solenoid. Instead, the poloidal one is provided by induction through a plasma current which is triggered with a central solenoid and flows toroidally.

An alternative magnetic configuration to the Tokamak is called *Stellarator* (Fig. 1.8b) [15], which is characterised by the absence of plasma current. The peculiarity of this configuration is that the helical transform of the magnetic field is obtained directly through a properly designed set of magnetic field coils. Because of this feature, the Stellarator configuration can avoid disruptions, since no current is flowing into it. On the other hand, the manufacture of a set of reliable magnetic coils for a Stellarator reactor currently is a very challenging task because of several technological limits in manifacturing and assembling the coils.

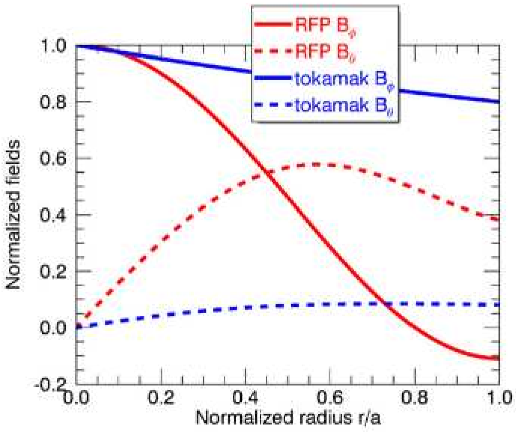

Figure 1.9: Radial profiles of the toroidal B_φ and the poloidal B_θ magnetic fields (normalized to the on-axis toroidal field value) for a Tokamak and Reversed Field Pinch. Taken from Ref. [14].

Finally, the second alternative to the Tokamak is represented by the *Reversed-Field-Pinch* (RFP, Fig. 1.8c). Tokamak and RFP share some similar properties, such as the co-presence of a toroidal and a poloidal magnetic field, and the pinch effect associated with the plasma current. However, the mechanisms which sustain the discharge in the two configurations are completely different. This is mainly due to the different ratio between toroidal and poloidal fields inside RFP, where $B_\varphi \approx B_\theta$ contrary to the Tokamak. A comparison between the two configurations is shown in Fig. 1.9. The way RFP sustains high magnetic fields in both directions is consequence of a large plasma current, which can heat the discharge through Ohmic-heating only.

1.6 MHD instabilities

1.6.1 The safety factor and the magnetic shear parameters

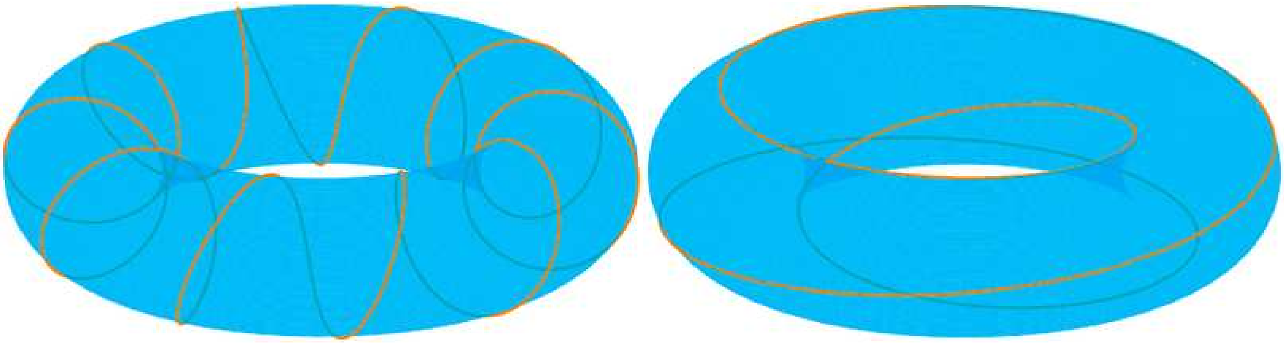
(a) $q = 1/10$ **(b)** $q = 2$

Figure 1.10: Two examples of magnetic field lines characterised by different safety factors [16].

Helical magnetic field lines are usually described in terms of the so-called *safety factor*, q. Referring to a single magnetic field line, it is defined as the ratio between the number of travelled toroidal turns run by a magnetic field line while it completes a full poloidal turn:

$$q = \frac{\Delta\varphi}{2\pi} \ , \tag{1.36}$$

where $\Delta\varphi$ is the portion of toroidal angle that is travelled by the magnetic field line during a complete poloidal turn. A few examples of magnetic field lines at different q are reported in Fig. 1.10. Magnetic field lines characterised by the same value of q form a *magnetic surface*.

In order to find an expression for the safety factor radial profile, $q \equiv q(r)$, one can consider the field line equation [17]:

$$\frac{R_0 \, \mathrm{d}\varphi}{r\mathrm{d}\theta} = \frac{B_\varphi}{B_\theta} \ , \tag{1.37}$$

where $r\mathrm{d}\theta$ is the distance run by the magnetic field line in the poloidal direction, and $\mathrm{d}\varphi$ is the infinitesimal portion of the toroidal angle. $q(r)$ is thus obtained by using Eq. (1.36) and integrating:

$$q(r) = \frac{1}{2\pi} \oint \mathrm{d}\varphi = \frac{1}{2\pi} \frac{r}{R_0} \frac{B_\varphi}{B_\theta} \oint \mathrm{d}\theta = \frac{r}{R_0} \frac{B_\varphi(r)}{B_\theta(r)} \ . \tag{1.38}$$

The value of the safety factor on the axis is related to the plasma current through the relation:

$$q_0 = q(0) = \frac{2B_\varphi(0)}{\mu_0 j_\varphi R_0} \ , \tag{1.39}$$

where j_φ is the plasma current density. The relation above is obtained under the assumption of a uniform plasma current profile.

1.6.2 Plasma instabilities

In general, several instabilities might occur in plasma. They are well described in the MHD framework. First of all, instabilities can be distinguished between *pressure-driven* and *current-driven* depending on if respectively pressure gradients or current gradients are responsible for the arising instability.

Alternatively, another way to classify plasma instabilities might be between *ideal* and *resistive modes* depending on the role the plasma resistivity, η, plays in determining the time evolution of the instability.
All instabilities can be analysed in the Fourier space. Namely, $\delta B_r(\vec{r})$, describing a local perturbation of the magnetic field in the radial direction, can be written in terms of a Fourier series as follows:

$$\delta B_r(\vec{r}) = \sum_{\vec{k}} b^r_{\vec{k}}(\vec{r})\ e^{i\left(\vec{k}\cdot\vec{r}+\omega t\right)} = \sum_{m,n} b^r_{m,n}(\vec{r})\ e^{i(m\theta - n\varphi + \omega t)}\ , \tag{1.40}$$

where $\vec{k} = (k_r, k_\theta, k_\varphi) = (k_r, m/r, n/R)$ is the wave vector written in toroidal coordinates, while $\vec{r}$ is the position vector in the real space. m and n are respectively known as *poloidal mode number* and *toroidal mode number*. As a consequence, the couple (m, n) identifies uniquely a single mode.
For a uniform plasma, small perturbations have a spatial structure similar to a wave. In this case, a single plane wave with a certain wave vector $\vec{k}$ and frequency ω arises. This wave is called *normal mode*. The frequency that describes each mode is a complex quantity $\omega = \omega_R + i\omega_I$, where the real part is related to the propagation velocity, while the imaginary part describes the growth ($\omega_I > 0$) or the attenuation ($\omega_I < 0$) of its amplitude.

The perturbation described in Eq. (1.40) is maximised for:

$$m\theta - n\varphi = 0\ . \tag{1.41}$$

Using the equation above we can calculate the distance traveled by the perturbed magnetic field line during a complete poloidal turn:

$$\Delta\varphi = \frac{m}{n}\cdot 2\pi \quad \Rightarrow \quad d_\varphi = R_0\cdot\Delta\varphi = \frac{m}{n}\cdot 2\pi R_0\ . \tag{1.42}$$

By comparing the Eq. (1.42) just written above with the field line equation in Eq. (1.37), and by taking into account the expression of the safety factor in Eq. (1.38), one gets the following *resonance condition*:

$$q = \frac{m}{n}\ . \tag{1.43}$$

Whenever the length of a magnetic field line is an integer multiple of the perturbation wavelength, then a resonant mode is excited. To conclude, *the most dangerous helical instabilities are localised in those positions of plasma where the corresponding safety factor has rational values.*

In an ideal plasma with no resistivity, $\eta = 0$, it can be demonstrated that the geometrical arrangement of the magnetic field lines, namely the plasma magnetic topology, is preserved (further details about this topic are going to be provided in Section 1.8.1). It implies that the magnetic field lines can not recombine in a new magnetic configuration. In the context of ideal MHD typical instabilities are the *ideal modes*, also called *kink modes* (see Fig.1.11). They appear in the form of a global kinking of the plasma column, they do not imply reconnection and are non-resonant, for example they are characterised by $m/n > q(0)$. Kink modes are typically stable in a RFP and they are not treated in this thesis.

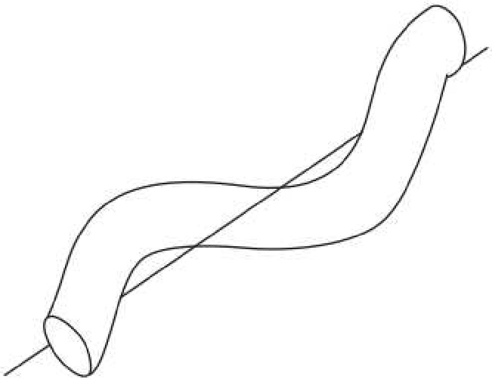

Figure 1.11: Sketch of a plasma perturbation corresponding to a kink mode. Taken from Ref. [18].

On the contrary, a resistive plasma with $\eta \neq 0$ displays large current instabilities in the form of *tearing modes*. In the case of the tearing modes, since the plasma is resistive, magnetic field lines reconnect with each other forming the so-called *magnetic islands*. Topologically, tearing modes are very different from ideal modes, as sketched in Fig. 1.12. The number of magnetic islands which lie on the toroidal and the poloidal plane is uniquely related respectively to the toroidal and the poloidal mode numbers n and m which describe the instability driving the phenomenon. Their radial position is determined by the profile of the safety factor. Each magnetic island is characterised by two points: the *O-point* is that around which the magnetic field lines rotate, while the *X-point* is that where magnetic reconnection events take place. The magnetic surface on which the X-point lies is called *separatrix*, because it separates the volume of the island from the surrounding plasma. The width of a single island, w, is defined as the distance between the extremities of its separatrix, and is proportional to $\left(\frac{\delta B}{B}\right)^{\frac{1}{2}}$ [19].

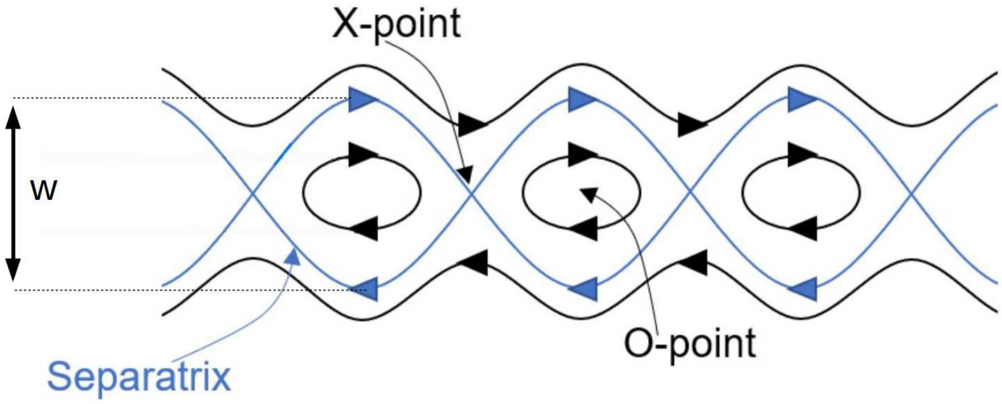

Figure 1.12: Sketch of the reconnection of magnetic field lines producing magnetic islands.

Another useful parameter is the *magnetic shear*, which is defined as:

$$s(r) = \frac{r}{q(r)} \frac{dq(r)}{dr} \ . \tag{1.44}$$

It represents the variation in the direction of the magnetic field, which affects the size of the islands [20].

1.6.3 Operational limit for a fusion reactor

By substituting the ideal gas law: $p \propto nT$ into the Eq. (1.19), then one has:

$$nT\tau_E \propto B^2 \beta \tau_E \ . \tag{1.45}$$

As a consequence, in principle, in order to fulfill the ignition condition, it is desirable to increase the value of β as much as possible. However, the maximum achievable values are limited by the so-called *Troyon limit* [21]:

$$\beta\,(\%) < g \frac{I_{P[\mathrm{MA}]}}{a_{[\mathrm{m}]} \cdot B_{\varphi[\mathrm{T}]}} \ , \tag{1.46}$$

where a, B_φ, I_P are respectively the minor radius, the toroidal magnetic field, and the plasma current, while the constant g is called *Troyon factor* (its value is typically in the range between 2.8 and 3.5). Experimentally, above this limit, pressure-driven instabilities development is found.

Another very important operational limit regards the numerical density. A phenomenological law based on experimental data was found by Greenwald [22]. It states that stability (with respect to the density limit) is obtained for the averaged values of the electronic density $\langle n_e \rangle$ such that:

$$\langle n_e \rangle \left(10^{20}\ \mathrm{m}^{-3}\right) < \frac{I_{P[\mathrm{MA}]}}{\pi a^2_{[\mathrm{m}^2]}} \equiv n_G \ , \tag{1.47}$$

where the right-hand side is known as *Greenwald density*, n_G.
For both Tokamaks and RFPs, the existence of a limit as concerns the electronic density is justified

with the development of thermal instability at the plasma edge. In Tokamaks the consequent shrinking of the plasma current might trigger a plasma disruption, i.e. an abrupt termination of the discharge. Instead, in the case of RFPs, it usually leads to a soft landing of the plasma discharge rather than to a fast termination [23].

1.7 Perturbations in Tokamak configuration

1.7.1 Edge Localised Modes

The typical radial profile of the magnetic fields in the Tokamak magnetic configuration (see Fig. 1.9) implies that $q_0 \geq 1$. This means that only a few tearing modes, especially those characterised by $n = 1$ and $m = 1, 2, 3$ can arise in the plasma during a discharge. Furthermore, the amplitude of the perturbations caused by these instabilities, calculated according to Eq. (1.40), is of the order of a few mT, very small with respect to the on-axis magnetic field B_0, which is of the order of a few T.
In principle, since spontaneous resonances are almost irrelevant for the MHD dynamics in Tokamak at $n \ll n_G$, such a configuration is capable to achieve a very high plasma confinement time τ_E, as it is desirable to reach the ignition condition, thanks to the overall stability it guarantees. For instance, for the first time in ASDEX [25], it has been observed that, in presence of external heating sources, it is possible to sensitively improve the confinement time. This discharge regime is called *High confinement mode* or *H-mode*. Its peculiarity consists of the formation of a steep gradient in the pressure radial profile (named *pedestal*) just inside the last closed flux surface, as shown in Fig. 1.13. It results in an edge transport barrier since the transport of heat and particles is strongly reduced compared to the rest of the plasma. The drawback is that, as we already mentioned, too steep pressure gradients destabilise pressure-driven modes at the edge. They are the *Edge Localised Modes* (ELMs).

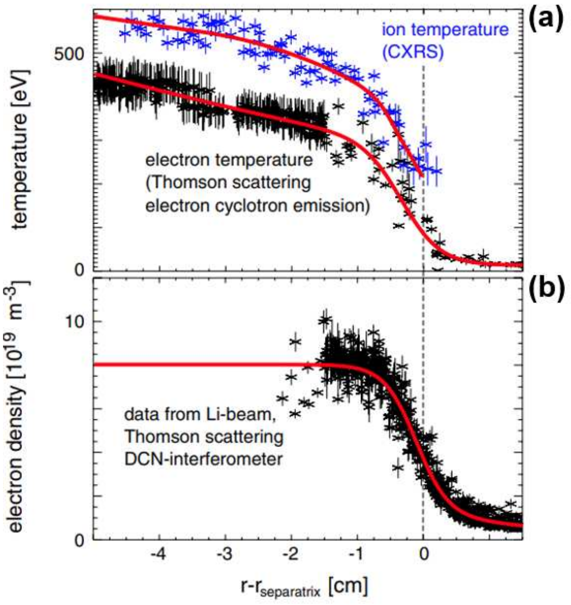

Figure 1.13: Experimental profile of **(a)** temperature and **(b)** electron density in the very edge of the plasma leading to the formation of the typical pedestal structure in the pressure radial profile in H-mode during an ASDEX Upgrade Tokamak discharge. Taken from Ref. [24].

The ELMs are violent MHD events, associated with an abrupt decrease of the pressure gradient forming the pedestal, resulting in a large loss of fast particles and energy toward the plasma-facing components (PFC). The energy loss for a single ELM event might be tremendously dangerous for a large device such as ITER since the amount of energy deposited on the first wall is so high that the plasma-facing materials might be melted or even destroyed during the event. This is the reason why methods that are able at least to mitigate such a release of energy during ELMs are one of the prime interests in the field of fusion research, as concerns Tokamak devices. One possible solution in this sense is represented by the application of *Resonant Magnetic Perturbations* (RMPs) through a set of coils surrounding the vacuum vessel. Indeed, it has already been successfully demonstrated in some experiments as TORE Supra [26] and TEXTOR [27], that such a set of coils, called *ergodic divertor*, can mitigate or even completely suppress ELMs and, as a consequence, to control the power deposition on PFC by externally applying a set of properly characterised resonating instabilities.
In a few words, sufficiently large tearing modes are not naturally present in the case of a Tokamak magnetically confined plasma. Instead, they are artificially induced so as to avoid dangerous pressure-driven instabilities which periodically arise in such a plasma.

1.7.2 Homoclinic tangles

The mechanism driving the suppression of ELMs through RMPs is based on the induced stochasticity of the magnetic field lines pattern, as well described by Evans in Refs. [28, 29].
Formally speaking, by looking at Fig. 1.12. The O-points and the X-points of such a scheme are respectively the elliptic points and the hyperbolic points of the system particle dynamics. Moreover, given a hyperbolic point x, one can notice two kinds of invariant manifolds, dubbed *stable* (or *unstable*). They are defined as the sets of points starting from which the dynamics of the system tend to indefinitely move close (away) with respect to the hyperbolic point. They are easily recognisable along the separatrix direction in Fig. 1.12.

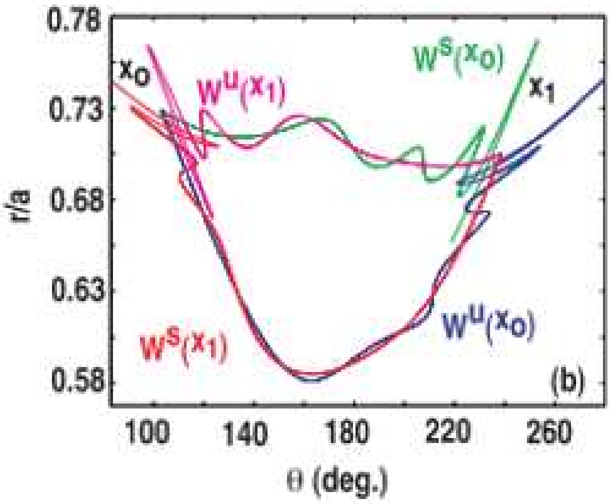

Figure 1.14: Sketch of the invariant manifolds making up the separatrix of a magnetic island. Picture taken from Ref. [29].

However, the stable (unstable) manifold of one hyperbolic point cannot intersect the stable (unstable) manifold of another hyperbolic point. But, if the two hyperbolic points are connected with a field line, *stable manifolds can intersect unstable manifolds transversely resulting in* homoclinic tangles[5].
Therefore, the real arrangement of magnetic islands resembles much more the one reported in Fig. 1.14, where it is shown that the separatrix is composed of a pair of invariant manifolds mixing, rather than the simplified scheme in Fig. 1.12.
The formation of homoclinic tangles is the main effect of the overlapping of magnetic islands, resulting in the chaotic tunneling of magnetic field lines from one island to the neighboring one. Thus, the importance of the introduction of RMPs at the edge of the plasma consists of the formation of a chaotic layer that mitigates the density and pressure gradients of the H-mode pedestal by slowing down and then driving particles toward the vessel first wall. This approach seems to reduce particle and heat transport to the wall and meanwhile to increase time confinement as regards both energy and particles.

---

[5] Heteroclinic tangles are however possible for unconnected hyperbolic points, for example between those that appear on the magnetic surface related to a mode like $m = 4$, $n = 2$. However, this is far beyond the contents of this thesis and we are not going to point out further details in the following about this specific kind of tangles.

1.8 MHD theory of RFP configuration

1.8.1 The magnetic helicity

Consider a region such that all magnetic field lines are closed within it, with no field lines crossing its boundary. Formally, it means that the normal component B_n is null at the boundary surface of the region. The *magnetic helicity* of the magnetic field in this region is defined as:

$$\mathcal{H} = \int_V \vec{A} \cdot \vec{B} \, \mathrm{d}V \ , \tag{1.48}$$

where the integration has to be done over the whole region V satisfying the so-called perfect boundary condition, i.e. $B_n = 0$.

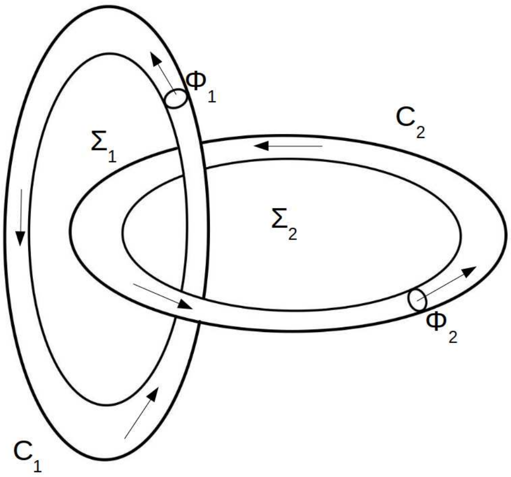

Figure 1.15: Simple scheme of two interconnected magnetic flux tubes.

In Ref. [30] an useful example to understand the connection between magnetic helicity and magnetic topology is discussed by Moffatt. It consists of the calculation of the magnetic helicity of a simple magnetic configuration like the one shown in Fig. 1.15, where there are two interconnected tubes, C_1 and C_2. Correspondingly there are two magnetic fields. No magnetic field exists outside so as to fulfill $B_n = 0$. Let the magnetic fluxes through the sections of these two tubes respectively be Φ_1 and Φ_2. In order to find the magnetic helicity of the entire system, consider a small volume element $\mathrm{d}V$ of tube C_1 whose contribution to the total magnetic helicity is $\vec{A} \cdot \vec{B} \, \mathrm{d}V$. Replacing $B \, \mathrm{d}V$ with $\Phi_1 \, \mathrm{d}\vec{x}$, the contribution coming from the whole tube C_1 is then calculated by integrating over the circuit:

$$\mathcal{H}_1 = \Phi_1 \oint_{C_1} \vec{A} \cdot \mathrm{d}\vec{x} = \Phi_1 \int_{\Sigma_1} \left(\nabla \times \vec{A} \right) \cdot \mathrm{d}\vec{S} = \Phi_1 \int_{\Sigma_1} \vec{B} \cdot \mathrm{d}\vec{S} \ , \tag{1.49}$$

where in the first passage the Stokes theorem has been used to transform the line integral $\oint_{C_1} \vec{A} \cdot \mathrm{d}\vec{x}$ into the surface integral $\int_{\Sigma_1} \left(\nabla \times \vec{A} \right) \cdot \mathrm{d}\vec{S}$, which corresponds exactly to the magnetic flux passing through the surface Σ_1 and turns out to be Φ_2 in the present case. From Eq. (1.49), one finally gets:

$$\mathcal{H}_1 = \Phi_1 \Phi_2 \ . \tag{1.50}$$

Since the contribution of the other tube C_2 would be analogously calculated, its contribution to the magnetic helicity of the whole system would be the same. Hence:

$$\mathcal{H} = \mathcal{H}_1 + \mathcal{H}_2 = 2\Phi_1 \Phi_2 \ . \tag{1.51}$$

The importance of this result is based on the fact that the expression of the magnetic helicity depends only on if the two fluxes Φ_1 and Φ_2 are interlinked. In fact, the value of the magnetic helicity does not change under the deformation of the two tubes C_1 and C_2 as long as their linkage stays the same. Instead, if one tube was cut and removed so that the linkage between C_1 and C_2 was broken, then the magnetic helicity of the whole new configuration would be zero. As a consequence, there is a direct correspondence between the magnetic helicity and the topology of the magnetic lines. *As long as the magnetic topology does not change, the magnetic helicity is an invariant of the magnetic configuration.*

As concerns the magnetic topology, two relevant results have been demonstrated by Woltjer in Ref. [31]:

Theorem. ***(First Woltjer's theorem)*** *The magnetic topology is preserved for a magnetofluid with zero resistivity.*

Proof. Since the magnetic helicity is directly related to the topology, one expects that the magnetic helicity also would be invariant for an ideal magnetofluid. Therefore, to prove the theorem one must verify that:

$$\frac{\mathrm{d}\mathcal{H}}{\mathrm{d}t} = 0 \ . \tag{1.52}$$

Using the definition of magnetic helicity in Eq. (1.48):

$$\frac{\mathrm{d}\mathcal{H}}{\mathrm{d}t} = \int_V \frac{\partial \vec{A}}{\partial t} \cdot \vec{B} \ \mathrm{d}V + \int_V \vec{A} \cdot \frac{\partial \vec{B}}{\partial t} \ \mathrm{d}V \ . \tag{1.53}$$

Let us recall the induction equation (1.31) for an ideal magnetofluid:

$$\nabla \times \left(\vec{v} \times \vec{B}\right) = \frac{\partial \vec{B}}{\partial t} = \frac{\partial}{\partial t}\left(\nabla \times \vec{A}\right) = \nabla \times \frac{\partial \vec{A}}{\partial t} \quad \Leftrightarrow \quad \frac{\partial \vec{A}}{\partial t} = \vec{v} \times \vec{B} \ . \tag{1.54}$$

By substituting inside the Eq. (1.53), it becomes:

$$\frac{\mathrm{d}\mathcal{H}}{\mathrm{d}t} = \cancel{\int_V \left(\vec{v} \times \vec{B}\right) \cdot \vec{B}} \ \mathrm{d}V + \int_V \vec{A} \cdot \left[\nabla \times \left(\vec{v} \times \vec{B}\right)\right] \ \mathrm{d}V \ . \tag{1.55}$$

The first term is canceled because two vectors that are perpendicular each other are scalar multiplied. Instead, the second term can be written in this way:

$$\frac{\mathrm{d}\mathcal{H}}{\mathrm{d}t} = \cancel{\int_V \left(\vec{v} \times \vec{B}\right) \cdot \vec{B}} \ \mathrm{d}V - \int_V \nabla \cdot \left[\vec{A} \times \left(\vec{v} \times \vec{B}\right)\right] \ \mathrm{d}V \ . \tag{1.56}$$

The first term can be neglected for the same reason as before. Whereas, the second term can be managed using the Gauss divergence theorem:

$$\frac{\mathrm{d}\mathcal{H}}{\mathrm{d}t} = -\int_S \vec{A} \times \left(\vec{v} \times \vec{B}\right) \ \mathrm{d}S \ . \tag{1.57}$$

By taking into account that $\vec{v}$ and $\vec{B}$ are perpendicular to each other, one finally has:

$$\frac{\mathrm{d}\mathcal{H}}{\mathrm{d}t} = \int_S \left(\vec{A} \cdot \vec{v}\right) \cdot \vec{B} \ \mathrm{d}S = 0 \ , \tag{1.58}$$

which is null since perfect boundary conditions ($B_n = 0$) have been assumed at the beginning.

$\square$

The second Woltjer's result involves the *magnetic energy* (of a charged particles system), which is defined as follows:

$$W = \int_V \frac{B^2}{2\mu_0} \ \mathrm{d}V \ . \tag{1.59}$$

Theorem. ***(Second Woltjer's theorem)*** *An ideal magnetofluid reaches the minimum of its magnetic energy in the configuration which satisfies the following relation:*

$$\nabla \times \vec{B} = \mu \vec{B} \ . \tag{1.60}$$

Proof. Since, for an ideal magnetofluid, the magnetic helicity is an invariant (as the first Woltjer's theorem states), one way to calculate the minimum of the magnetic energy is to employ the method of Lagrange's multipliers, namely to impose:

$$\delta W - \frac{\mu}{2\mu_0}\delta\mathcal{H} = 0 \ , \tag{1.61}$$

where μ is formally a Lagrange's multiplier. The 'δ' symbol represents the differential operator. By substituting in the equation above the expression for the magnetic energy (1.59), and for the magnetic helicity (1.48), after having manipulated the r.h.s. of the equation, one gets:

$$\begin{aligned} 0 &= \delta\left[\int_V \frac{B^2}{2\mu_0}\,\mathrm{d}V - \frac{\mu}{2\mu_0}\int_V \vec{A}\cdot\vec{B}\,\mathrm{d}V\right] && (1.62)\\ &= \frac{1}{\mu_0}\int_V \vec{B}\cdot\delta\vec{B}\,\mathrm{d}V - \frac{\mu}{2\mu_0}\int_V \delta\vec{A}\cdot\vec{B}\,\mathrm{d}V - \frac{\mu}{2\mu_0}\int_V \vec{A}\cdot\delta\vec{B}\,\mathrm{d}V && (1.63)\\ &= \frac{1}{\mu_0}\int_V \vec{B}\cdot\delta\vec{B}\,\mathrm{d}V - \frac{\mu}{\mu_0}\int_V \delta\vec{A}\cdot\vec{B}\,\mathrm{d}V + \frac{\mu}{2\mu_0}\int_V \nabla\cdot\left(\vec{A}\times\delta\vec{A}\right)\,\mathrm{d}V && (1.64)\\ &= \frac{1}{\mu_0}\left[\int_V \vec{B}\cdot\left(\delta\vec{B}-\mu\delta\vec{A}\right)\,\mathrm{d}V\right] + \cancel{\frac{\mu}{2\mu_0}\int_V \nabla\cdot\left(\vec{A}\times\delta\vec{A}\right)\,\mathrm{d}V}\ , && (1.65) \end{aligned}$$

where it has been used the relation: $\delta\vec{B} = \nabla\times\delta\vec{A}$. Namely:

$$\int_V \nabla\cdot\left(\vec{A}\times\delta\vec{A}\right)\,\mathrm{d}V = \int_S \vec{A}\times\delta\vec{A}\,\mathrm{d}S = 0\ , \tag{1.66}$$

and the last term has been neglected because $B_n = 0$. Hence, one has:

$$\delta\vec{B} - \mu\delta\vec{A} = 0 \quad \Rightarrow \quad \vec{B} = \mu\vec{A}\ . \tag{1.67}$$

Finally, by applying the curl operator to both sides:

$$\nabla\times\vec{B} = \mu\nabla\times\vec{A} \quad \Rightarrow \quad \nabla\times\vec{B} = \mu\vec{B}\ . \tag{1.68}$$

□

The process driving plasma to the minimum of the magnetic energy is called *relaxation*, and the plasma energy state at its minimum is said *relaxed state.*

The results coming from Woltjer's theorems can be considered sufficiently valid also for a plasma with a finite but small resistivity. By remembering what has just been said at the end of Section 1.6.2, the resistive MHD instabilities drive the plasma relaxation since they let the magnetic field lines break and reconnect each other, leading the plasma to the relatively more stable available magnetic configuration in closer proximity to the fully relaxed state. As Moffatt's argument underlines, the magnetic helicity and the magnetic topology are strongly bound. To conclude, by extending the results coming from the two Woltjer's theorems to slightly resistive plasmas, an important relationship between plasma relaxation events and magnetic reconnection phenomena delivered by tearing modes instabilities, is found. Reversed-field pinch experiments, like RFX and RFX-mod later, have demonstrated the relevance of this link. Further details are going to be provided in the next Section about reconnection events.

By combining the Eq. (1.60) with the Ampére's law, $\nabla\times\vec{B} = \mu_0\vec{j}$, it follows:

$$\mu\vec{B} = \mu_0\vec{j}\ . \tag{1.69}$$

Therefore, for an ideal magnetofluid, the magnetic field and the current density are parallel. As a consequence, the pressure gradient given according to the Grad-Shafranov equation (1.33) is null, namely:

$$\nabla p = \vec{j}\times\vec{B} = 0\ . \tag{1.70}$$

This is the reason why the magnetic field profile satisfying the Eq. (1.60) is called *force-free field.* From the Eq. (1.69), one can calculate a formula for the coefficient μ:

$$\mu = \mu_0\,\frac{\vec{j}\cdot\vec{B}}{B^2}\ . \tag{1.71}$$

1.8.2 The Bessel Function Model

The Bessel Function Model (BFM) provides a simplified description of the RFP magnetic configuration. In this sense two useful parameters are the *reversal parameter* F and the *pinch parameter* Θ. Being a the minor radius, they are defined as:

$$F = \frac{B_\varphi(a)}{\langle B_\varphi \rangle} \qquad , \qquad \Theta = \frac{B_\theta(a)}{\langle B_\varphi \rangle} \ . \tag{1.72}$$

$\langle B_\varphi \rangle$ is the poloidal average of the toroidal field B_φ. It is related to the flux of the toroidal magnetic field, $\Phi(B_\varphi)$, through the following relation:

$$\langle B_\varphi \rangle = \frac{1}{\pi a^2} \int_0^a dr\; 2\pi r B_\varphi(r) = \frac{1}{\pi a^2}\, \Phi(B_\varphi) \ . \tag{1.73}$$

The safety factor at the plasma boundary is thus given by:

$$q_a = q(a) = \frac{a\ B_\varphi(a)}{R_0\ B_\theta(a)} = \frac{a}{R_0}\frac{F}{\Theta} \ . \tag{1.74}$$

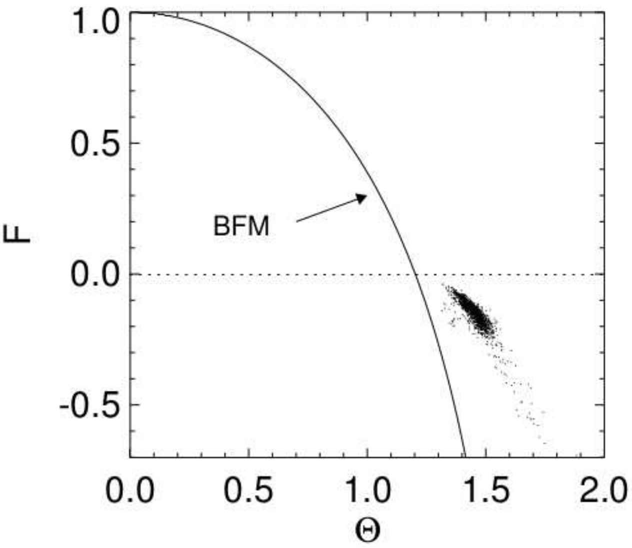

Figure 1.16: Comparison between the $F - \Theta$ curve which has been derived from the BFM and the experimental points measured in RFX. Adapted from Ref.[32].

F and Θ are not independent. The relation between the two parameters is graphically reported in Fig. 1.16. To make explicit the relation between them, it is possible to solve the force-free field equation (1.60). For the sake of simplicity, consider cylindrical coordinates and assume that μ is uniform across the whole cylinder section.

By writing the Eq. 1.60 along the axial and poloidal directions of the cylindrical coordinates system, one gets:

$$\frac{\partial B_z}{\partial r} = \mu B_\theta \qquad , \qquad \frac{1}{r}\frac{\partial}{\partial r}(rB_\theta) = \mu B_z \ . \tag{1.75}$$

By combining the equations above, and by subsequently making a change of variable, $r' = \mu r$, one obtains:

$$r' \frac{\partial}{\partial r'}\left(r' \frac{\partial B_z}{\partial r'} \right) + r'^2 B_z = 0 \ . \tag{1.76}$$

The one written above is the differential Bessel equation for $B_z(r')$, which is solved by:

$$B_z(r') = B_0\ J_0(r') \quad \Rightarrow \quad B_z(r) = B_0\ J_0(\mu r) \ , \tag{1.77}$$

where $J_0(r')$ is the zero-order Bessel function [33], while B_0 represents the on-axis magnetic field amplitude.
By substituting back B_z through the Eqs. in 1.75, a solution is found also for B_θ:

$$B_\theta(r) = B_0\ J_1(\mu r) \ , \tag{1.78}$$

where $J_1(\rho)$ is the first-order Bessel's function.

Finally, the profiles of the axial and poloidal current densities, j_z and j_θ, are obtained by combining the force-free field equation with the Ampére's law:

$$\mu_0 j_z = \mu B_z \quad \Rightarrow \quad j_z = \frac{\mu}{\mu_0} B_0 \; J_0(\mu r) \; ; \tag{1.79}$$

$$\mu_0 j_\theta = \mu B_\theta \quad \Rightarrow \quad j_\theta = \frac{\mu}{\mu_0} B_0 \; J_1(\mu r) \; . \tag{1.80}$$

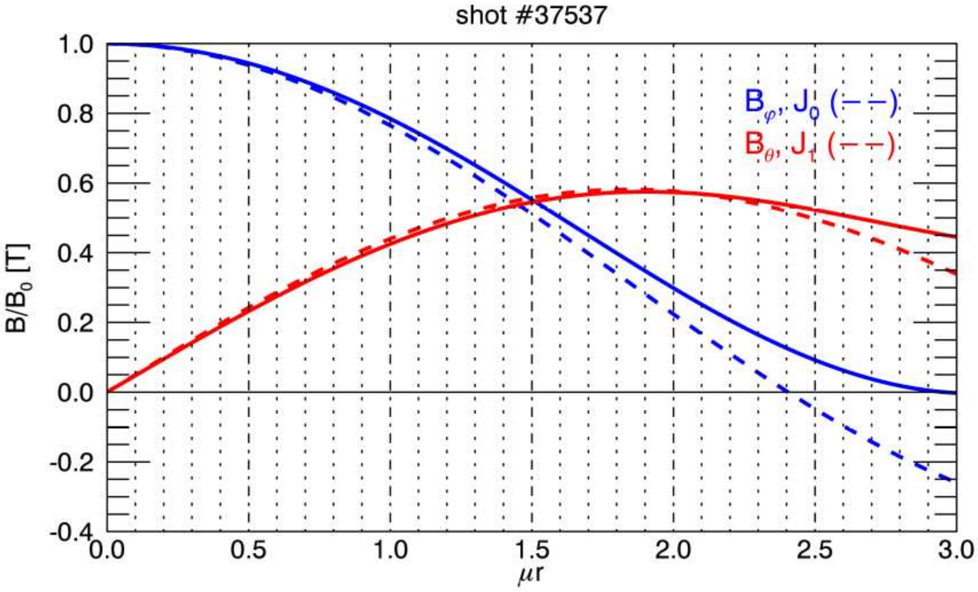

Figure 1.17: According to BFM, the profiles of the normalised magnetic field and the current density components are the same of the first two orders of Bessel's functions: J_0 and J_1. Here, they are compared to a real magnetic configuration realised during the shot #37537 in RFX-mod.

In Fig. 1.17, a comparison between the two Bessel's function profiles and the profiles of the magnetic fields in a typical RFX-mod discharge (# 37537) is shown. The first observation one can do is that the BFM provides a good analytical explanation for the reversal of the toroidal magnetic field at the edge in the case of the RFP magnetic configuration. Moreover, it can be easily seen that the argument reported above can be adapted also in the case of a toroidal geometry with a sufficiently high aspect ratio, the one of the RFX-mod is $A \approx 4$ indeed.

On the whole, the results coming from the BFM are useful to determine an analytic expression for both F and Θ which depends on the geometrical and physical characteristics of the RFP configuration. First of all, by substituting the expression for $B_z(r)$ (1.77) into the calculation of the mean axial magnetic field (1.73), one can easily obtain the following relation:

$$\langle B_z \rangle = \frac{2}{\mu a} B_0 \; J_1(\mu a) \; . \tag{1.81}$$

By inserting such an expression for $\langle B_z \rangle$ into the definition of Θ parameter in Eq. (1.72), one has:

$$2\Theta = \mu a \; . \tag{1.82}$$

Analogously, for the F parameter, it follows:

$$F = \Theta \, \frac{J_0(\mu a)}{J_1(\mu a)} \; . \tag{1.83}$$

From this equation, the profile of the $F - \Theta$ curve in Fig. 1.16 is deduced. Not only, but one can also conclude that the reversal of the first-order Bessel's function J_0 indicates where the toroidal magnetic field changes sign in the RFP configuration. By looking at the graph in Fig. 1.17, it is found that this is the case for $\mu a > 2.405$. Therefore, one can experimentally work in the magnetic RFP configuration as long as the condition $\Theta > 1.2$ is satisfied. This is confirmed also by the $F - \Theta$ curve in Fig. 1.16. Finally, by using the following asymptotic expansion for $J_1(z)$:

$$\lim_{z \longrightarrow 0} J_1(z) = \frac{z}{2} \ , \tag{1.84}$$

one can calculate an expression for the safety factor on the axis. Namely:

$$q_0 = q(0) = \frac{a}{R}\frac{1}{\Theta} = \frac{\varepsilon}{\Theta} \ , \tag{1.85}$$

where ε identifies the so-called *inverse aspect-ratio*, i.e. $\varepsilon = A^{-1}$.

1.8.3 The μ & p model

Experimentally, to confine a plasma, a pressure gradient is needed. Since one of the main hypotheses of the BFM is that the magnetic field that confines the plasma is free-force, in Figs. 1.16-1.17 experimental data differ from the theoretically predicted curves, which do not consider the role of the pressure gradient in the confinement, especially in the edge region.

In order to take into account the effects of a pressure gradient, a more refined model [34] introduces some corrections to the initial assumption of the BFM. First of all, μ is not taken as uniform anymore but it is considered as a function of the radius: $\mu \equiv \mu(r)$. In particular, the following set of functions:

$$\mu(r) = \mu(0)\left(1 - \frac{r}{a}\right)^{\alpha} \ , \tag{1.86}$$

give a good approximation for the radial profile of $\mu(r)$ in RFP.

By implementing the set of Eqs. in 1.75 with the hypothesis of a not-null pressure gradient, one gets the following equations:

$$-\frac{\partial B_z}{\partial r} = \mu_0 j_\theta = \mu B_\theta + \mu_0 \frac{\partial p}{\partial r} \cdot \frac{B_z}{B^2} \ ; \tag{1.87}$$

$$\frac{1}{r}\frac{\partial}{\partial r}(rB_\theta) = \mu_0 j_z = \mu B_z - \mu_0 \frac{\partial p}{\partial r} \cdot \frac{B_\theta}{B^2} \ . \tag{1.88}$$

The system of differential equations we have just reported can be solved by taking as inputs the profiles of μ and pressure p. This is the reason why this model is called μ & p. The model can be solved numerically by normalising Eqs. (1.87) and (1.88) as:

$$\frac{\partial \widetilde{B_z}}{\partial \widetilde{r}} = -2\Theta_0 \widetilde{\mu} \widetilde{B}_\theta - \frac{\beta_0}{2}\frac{\partial}{\partial \widetilde{r}}\left(\widetilde{n}\widetilde{T}\right) \cdot \frac{\widetilde{B}_z}{\widetilde{B}^2} \ ; \tag{1.89}$$

$$\frac{\partial \widetilde{B}_\theta}{\partial \widetilde{r}} = -\frac{\widetilde{B}_\theta}{\widetilde{r}} + 2\Theta_0 \widetilde{\mu} \widetilde{B}_z - \frac{\beta_0}{2}\frac{\partial}{\partial \widetilde{r}}\left(\widetilde{n}\widetilde{T}\right) \cdot \frac{\widetilde{B}_\theta}{\widetilde{B}^2} \ . \tag{1.90}$$

The symbol $\widetilde{\cdot}$ indicates normalised quantities, namely:

$$\widetilde{r} = \frac{r}{a} \quad , \quad B_z(r) = B_0 \cdot \widetilde{B}_z(r) \quad , \quad B_\theta(r) = B_0 \cdot \widetilde{B}_\theta(r) \tag{1.91}$$

$$p(r) = p(0) \cdot \widetilde{p}(r) = 2n(0)T(0) \cdot \widetilde{n}(r)\widetilde{T}(r) \quad , \quad \mu(r) = \mu(0) \cdot \widetilde{\mu}(r) = \frac{2\Theta_0}{a} \cdot \widetilde{\mu}(r) \ . \tag{1.92}$$

Θ_0 is called *on-axis pinch parameter*, and similarly β_0 is the β-parameter on the axis. Considering the case of a free-force field, i.e. $p = 0$, and $\widetilde{\mu} = 1$, one comes back to the BFM with uniform $\Theta \equiv \Theta_0$.

The μ & p model is going to be used in Chapters 3 and 5 to calculate the equilibrium of the RFX-mod discharge studied in this thesis.

1.9 Perturbations in RFP configuration

1.9.1 Self-organization of the magnetic field

Consider the hypothesis of an incompressible magnetofluid. In such a case a fully dynamical theory consists uniquely of the motion equation (1.30) and the induction equation (1.31) which have to be solved by calculating the velocity field $\vec{v}$ and the magnetic field $\vec{B}$. Such a problem is said *kinematic dynamo problem*.

In Ref. [35], a toy model which gives a simple example of the self-organization of a cylindrical plasma (resembling the one in the RFP configuration), which implies the reversal of the magnetic field near the edge, is pointed out.
Consider a situation like the one reported in Figs. 1.18-1.19a. A current I flows along the axis with a wire, such that it is also responsible for a poloidal magnetic field B_θ. Meanwhile, a magnetic field B_φ is imposed in the axial direction thank to a poloidal current I_{shell} flowing in a conducting shell.
Assume that the wire is unstable and it kinks, as shown in Fig. 1.19b. Due to the kink, the magnetic field becomes stronger in the inner part and weaker in the outer part. This makes the wire kink further until, if the starting magnetic field is low enough, the magnetic field in the outer region B'_φ becomes negative. Therefore, if the reversal is sufficiently high, the wire reaches again a new equilibrium.
To conclude, *under certain circumstances*, the reversal of the magnetic field in the outer region of the plasma can be seen as a way the plasma has to *self-organise* [36] and relax.

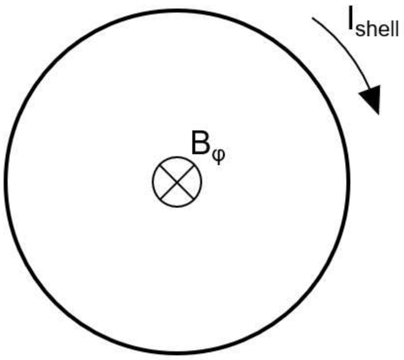

Figure 1.18: Poloidal section of the cylindrical magnetic configuration considered in the argument.

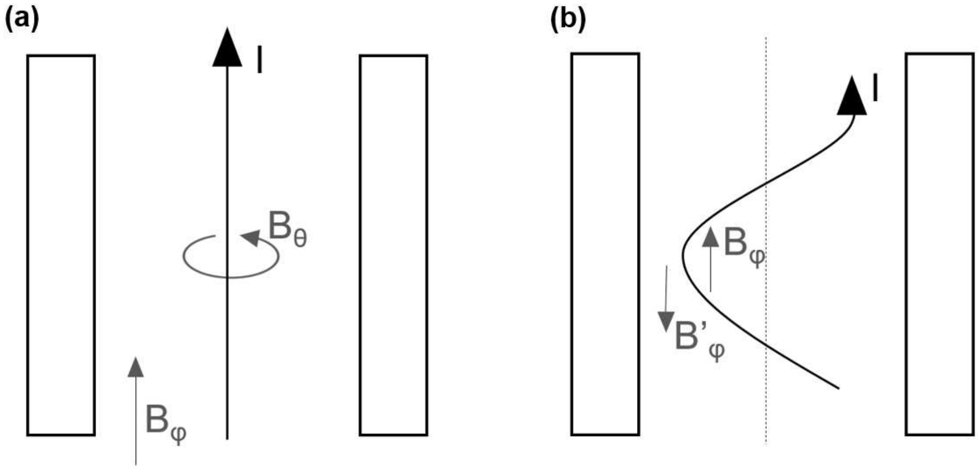

Figure 1.19: Evolution of the wire dynamics explained with the toy model: **(a)** unperturbed starting configuration, **(b)** perturbed configuration and final reversal of the toroidal magnetic field, B'_φ in the outer region.

1.9.2 The QSH and the MH states

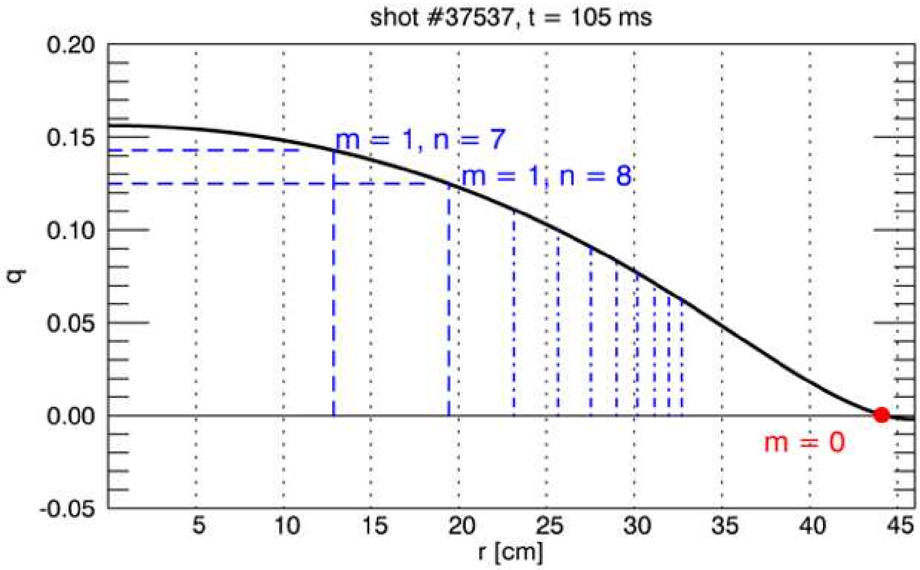

Figure 1.20: Safety factor profile during the #37537 shot, at $t = 105$ ms in RFX-mod.

As already mentioned at the end of Section 1.5, the peculiarity of the RFP magnetic configuration is that the magnetic field components are of the same order of magnitude, and in particular B_φ reverses its sign at the plasma edge. From a technological point of view, the RFP has the advantage that no super-conducting coils are needed to generate the magnetic field. At the same time, the fact that $B_\varphi \approx B_\theta$ also implies that the safety factor q is relatively low across the whole plasma. For example, by looking at Fig. 1.20, where the radial profile of the safety factor during a typical RFX-mod discharge is reported, one immediately notices that q is always lower than 1, monotonically decreasing and negative at the edge, due to the B_φ reversal. Due to this q profile, multiple resonant surfaces are present inside the plasma, in particular those characterised by poloidal numbers $m = 1$ and $m = 0$. Since the maximum of q is achieved at the center of the plasma and its value is about $q_0 \approx 0.16$, the most internal resonant mode in RFX-mod is the one described by $m = 1$ and $n = 7$, such that $q_{1,7} \approx 0.14$.

All modes with $m = 1$ and $n > 7$ resonate inside the plasma during the discharge and are located in those radial positions where the safety factor has rational values, $q = \frac{m}{n}$. Instead, all $m = 0$ modes are positioned in correspondence to the so-called *reversal surface*, where $q = 0$. Their amplitudes, calculated according to Eq. (1.40), are of the order of a few mT in RFX-mod, which means that large magnetic islands are generated since the perturbation is of the order of a few percent the magnetic field at the axis. This information can be easily deduced by observing the graphs reported in Fig. 1.21. Depending on the shape of the $m = 1$ tearing modes spectrum, the plasma regime can be classified in two possible states. The *Quasi Single Helicity* (QSH) *state*, characterised by the dominance of the most internal mode $m = 1$, $n = 7$ over the other modes populating the plasma (which are consequently considered as *secondary*), i.e. the amplitude of the dominant mode is almost ten times the one of the secondary modes. The second state is called *Multiple Helicity* (MH), where it is not possible to recognise a dominant mode.

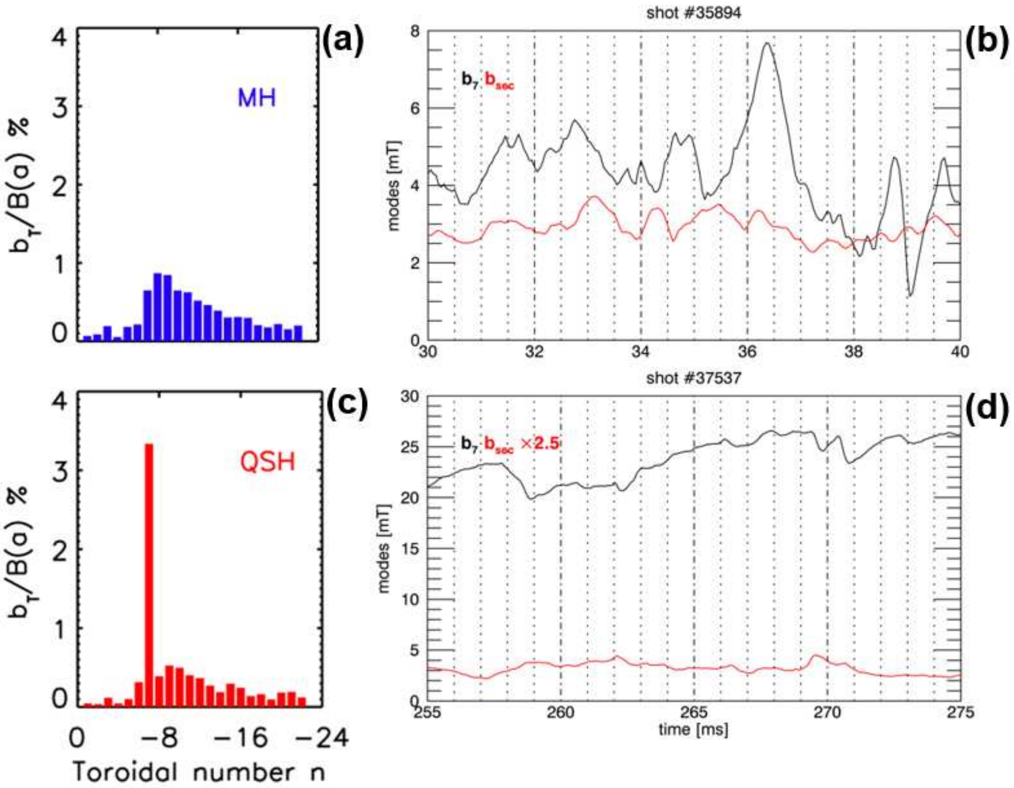

Figure 1.21: On the left, two examples of the typical spectra characterising respectively **(a)** the MH regime (in blue) and **(c)** the QSH regime (in red) in RFX-mod are shown. Whereas, on the right, the evolution of the amplitudes of the modes are correspondingly plotted for both **(b)** MH and **(d)** QSH states considering two different discharges in RFX-mod (respectively #35894 and #37537). The black line represents the mode amplitude of the dominant $m = 1$, $n = 7$ mode, the red line indicates the root mean square (r.m.s.) of the measured secondary modes ($m = 1$, $7 < n < 24$) amplitudes. Pictures **(a)** and **(c)** are taken from Ref. [37].

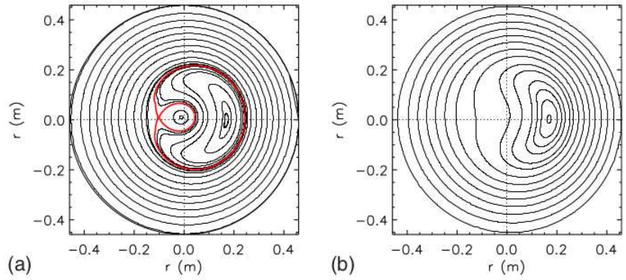

Figure 1.22: Reconstruction of the transition from **(a)** the QSH-DAx state to **(b)** the QSH-SHAx state. The separatrix of the magnetic island is coloured in red [37].

The QSH state is associated with the formation of a single magnetic island corresponding to the magnetic helicity of the dominant mode ($m = 1$, $n = 7$)[6], which influence the topology of the magnetic field lines throughout the whole plasma. The general way a QSH state occurs is where two magnetic axes are present in the plasma, located on the magnetic island O-point and on the equilibrium axis. In the RFP configuration, they can be easily recognised by looking at a poloidal section of the plasma. This configuration is called *Double Axes* (QSH-DAx) state (Fig. 1.22a). By increasing the plasma current above a certain threshold (which can be set experimentally at about $I_p = 1.4$ MA, [14]), a transition from the QSH-DAx state to a configuration, where only one degenerate magnetic axis remains, as it is shown in Fig. 1.22b, is observed. The new regime is called *Single Helical Axis* (QSH-SHAx) state.

The QSH-SHAx state is accompanied by the formation of a large plateau in the profile of the electron temperature, T_e, sustained by a large gradient in the outer region of the plasma, which is called *electron Internal Transport Barrier* (eITB). The presence of an eITB corresponds to a condition of

---

[6] To be more precise, another set of seven magnetic islands, corresponding to the mode $m = 0$, $n = 7$, appears due to an interaction process between modes which is called *toroidal coupling*. Since, at the moment, we focus only on the $m = 1$ modes spectrum, we are not going to investigate more this kind of modes, which actually are going to be mentioned later in the Section 4.2 of this thesis.

reduced particle transport and a consequent improvement of the confinement [38, 39].

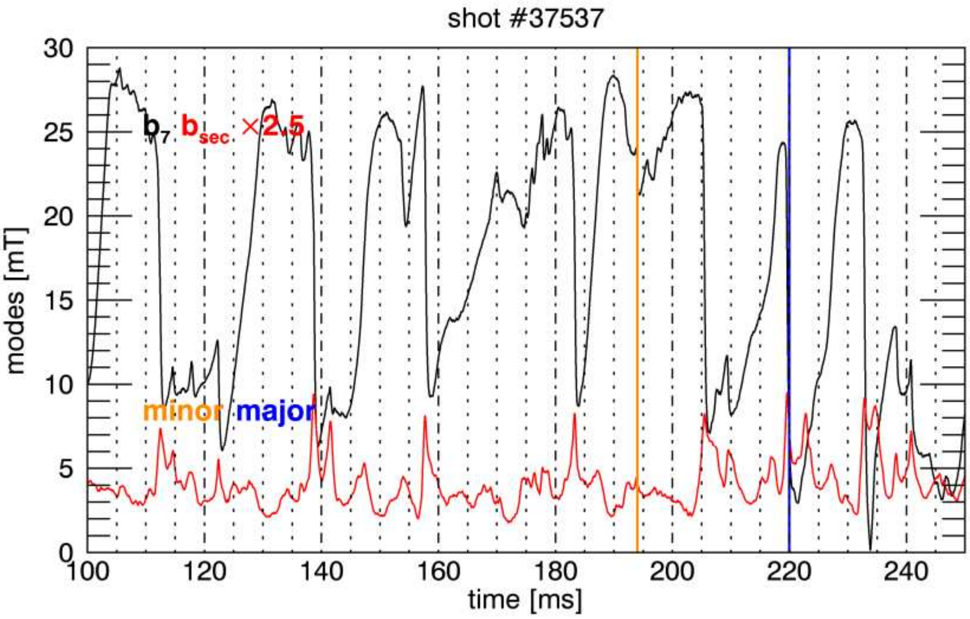

Figure 1.23: Evolution of the $m = 1$ modes amplitude during the shot # 37537 in RFX-mod. The black line represents the evolution of the $m = 1$, $n = 7$ mode amplitude, b_7. Whereas the red line represents the evolution of the r.m.s. secondary modes amplitudes, b_{sec}, multiplied by a factor 2.5. The orange and the blue vertical lines correspond respectively to the time instants of a minor and a major crash.

On the other hand, MH states are frequently observed in discharges at low plasma current ($I_p \leq 1$) or at large Greenwald fractions [40]. In any case, back-transitions from QSH to MH and vice versa are always present during a single discharge. This kind of events is strongly linked to the phenomena of plasma reconnection since they lead to the increase of secondary modes amplitudes. Therefore, they find a full explanation in the framework of the MHD treatment of plasma instabilities shortly introduced in Section 1.6.1.
The Figs. 1.23-1.24 summarise the evolution of the main parameters of an RFP discharge during the shot #37537 in RFX-mod. #37537 is a typical example of high current discharge in RFX-mod ($\langle I_p \rangle \approx 1.4$ MA), as it is confirmed by the fact that the QSH state is the favorite plasma state in most of the discharge. However, some time instants when the dominance of the $m = 1$, $n = 7$ mode over the other ones is partially or totally lost are observed. This kind of events takes the name of *crashes*. Their duration is of the order of a few milliseconds. Depending on the fact that, at the end of the crash, the $m = 1$, $n = 7$ is still dominant or not, it is used to distinguish between *partial* or *minor* and *major* crashes [41]. In particular, *during a major crash the plasma completely loses its helical state*, while during a minor crash the QSH survives the increase of secondary modes. Examples of major and minor crashes are both highlighted in Figs. 1.23-1.24. The orange line located at $t \approx 191$ ms represents a minor crash since, after the crash, b_7 is still much higher than b_{sec}. Instead, at $t \approx 220$ ms a major crash event is indicated in blue.

To understand the phenomenology of such a crash in RFP configuration, it is sufficient to look at Fig. 1.24. As already anticipated in the previous section, the increase of modes' amplitudes leads to the formation of chaotic regions associated with the magnetic islands overlap. In other words, a crash is a *Discrete Reconnection Event* (DRE) whose main effect is a loss of particles from the central to the outer part of plasma. The first consequence of such a loss is an overall reduction of the plasma current, determining the flattening of the q profile. According to Eq. (1.39) the safety factor at the center, q_0, is inversely proportional to the plasma current, so it must increase during the crash (Fig. 1.24a). In response, the safety factor at the edge q_a decreases (Fig. 1.24b) to avoid the flattening of the q

profile. The relations between q_0 and q_a and the RFP parameters F and Θ are given by Eqs. (1.74) and (1.85), according to the BFM. It follows that, during a crash Θ increases (Fig. 1.24c), while F undergoes an abrupt fall (Fig. 1.24d). Even if the phenomenology is the same, the distinction between major and minor crashes is obviously in the different amount of energy that is released with particles during the crash. By looking at the same figure one can also notice that the profile of q_a and F is almost the same since they are proportional. This is the reason why in the following of this thesis the crash analysis is going to be focused on the reversal parameter rather than q_a.

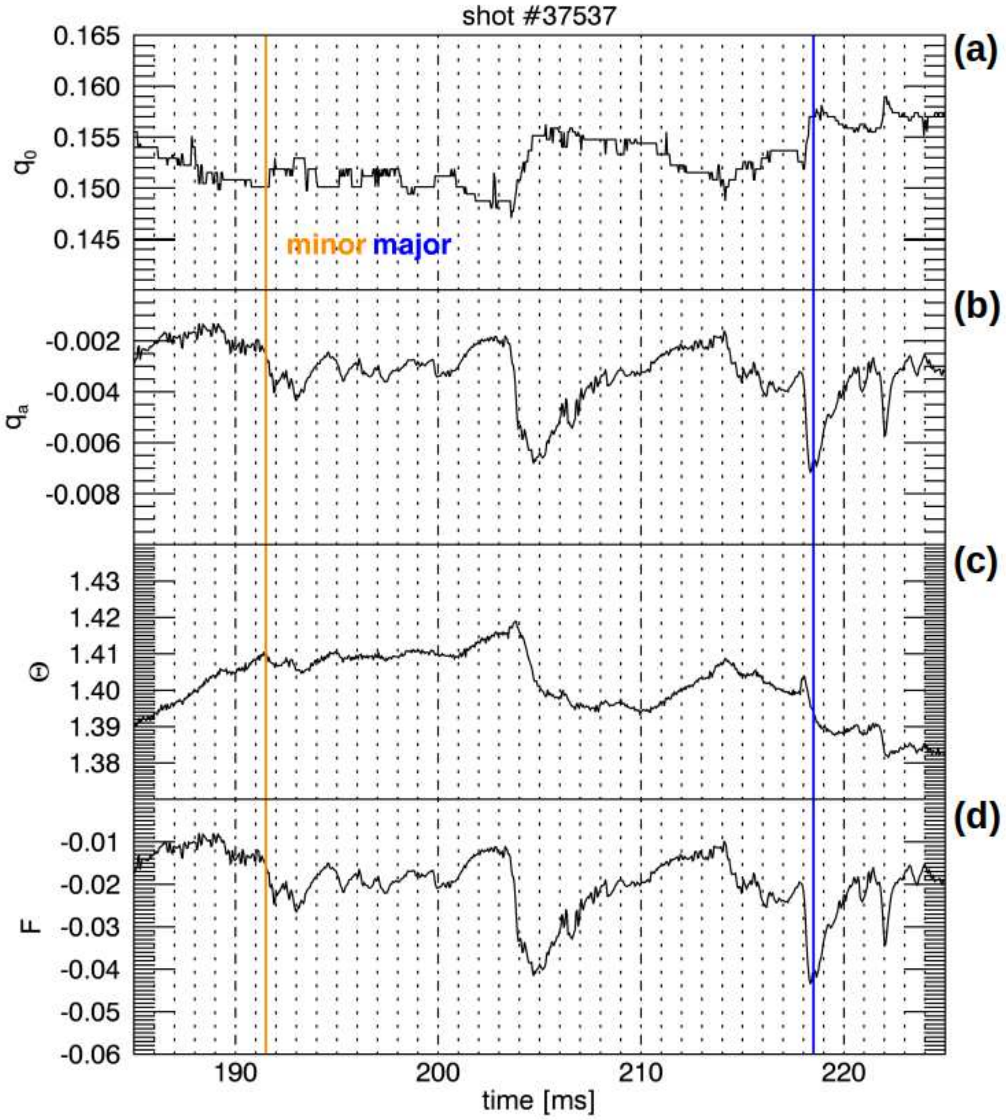

Figure 1.24: Representation of the evolution of the main plasma parameters during the shot #37537 in RFX-mod: **(a)** safety factor at the center, q_0, **(b)** safety factor at the edge, q_a, **(c)** the pinch parameter, Θ, and **(d)** the reversal parameter, F. The orange vertical line at $t \approx 191$ ms indicates a minor crash, while the blue line at $t \approx 218$ ms indicates a major crash.

To conclude, both the BFM and the μ & p model, state that the RFP magnetic configuration is the preferred equilibrium state for a resistive plasma that evolves according to the second Woltjer's theorem.
In other words, the tearing modes spontaneously occurring in the case of the RFP configuration drive the plasma relaxation towards the most stable state described by the force-free field (1.60), namely by reversing B_φ at the edge as sketched by the 'toy-wire-model'. In practice, this explains why reconnection (associated with tearing modes formation) and relaxation (associated with stability) are so strongly interconnected.

In this thesis we will focus on the analysis of particle loss and edge magnetic topology during a minor crash. We will show that, despite the presence of a QSH state, secondary modes are still capable of influencing particle transport and determine a large PWI.

Chapter 2

Setup and Methods

In this Chapter, the experimental setup and the numerical methods used in the thesis are presented. First, an overview of the RFX experiment, which is operated by Consorzio RFX in the CNR area in Padova, Italy, is provided. A particular attention is devoted to the imaging system of RFX, which allows to detect the Plasma-Wall Interaction (hereafter PWI) patterns which are the central topic of the thesis. Then, the numerical methods are introduced, namely the guiding center code ORBIT *which has been used to simulate the PWI patterns measured with the fast cameras.*

2.1 The RFX-mod experiment

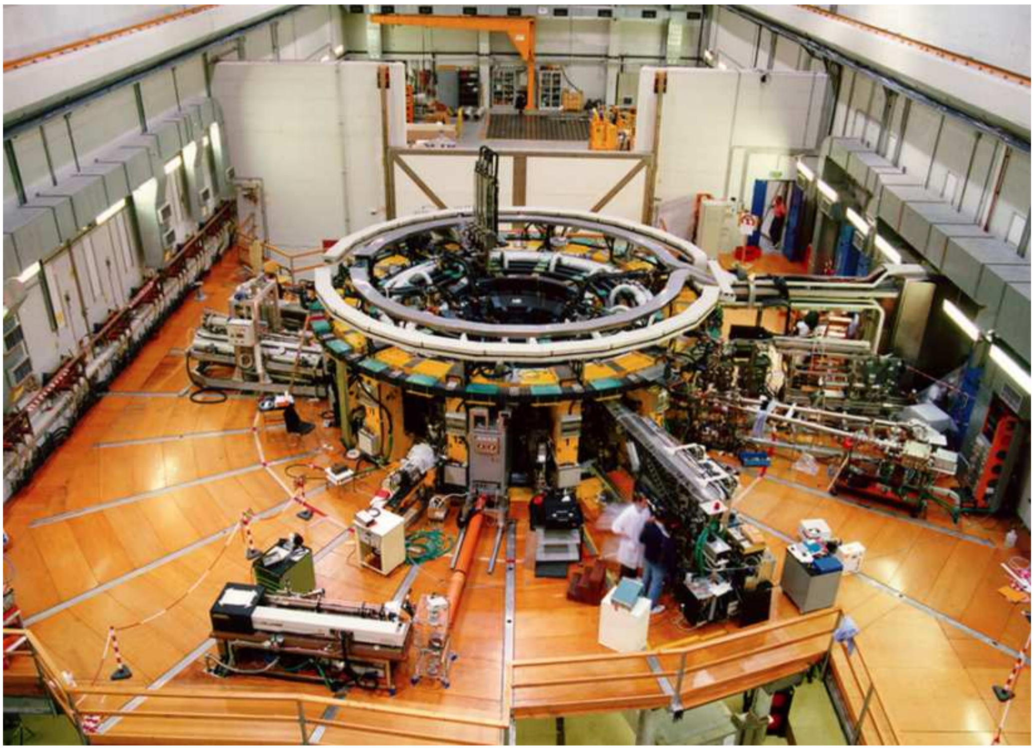

Figure 2.1: Picture of the RFX-mod device looking towards the assembly hall (image courtesy: Maria Teresa Orlando).

The Reversed Field eXperiment (RFX-mod) is a medium-sized device that mainly works in the RFP magnetic configuration, and is operated in the CNR research area in Padova, Italy. The main parameters of the machine are shown in Tab. 2.1.

Historically, the device had three phases of operation:
The **RFX** experiment itself, which started the operations in 1992 [43]. Initially, it was an RFP with a 65 mm (penetration time of the vertical field $\tau_V \approx 400$ ms) thick shell made of Aluminum [44]. Such a shell was exploited to passively stabilize ideal modes.

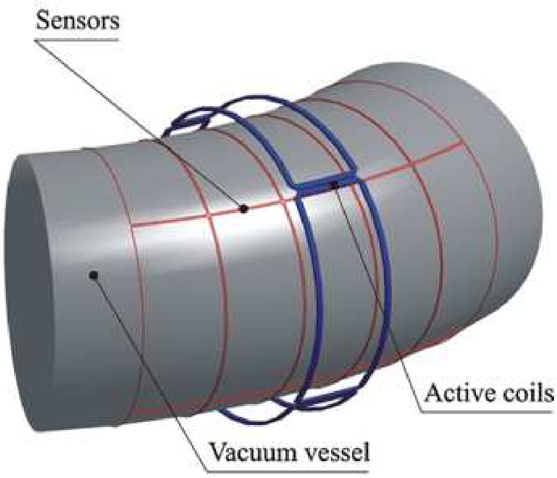

Figure 2.2: Arrangement of a set of coils forming the active feedback system of RFX-mod [42].

In 1999 an accident at the Toroidal Field (TF) power supply interrupted the experimental activities. The RFX experiment was modified, and the thick shell was replaced with a thin, copper shell of 3mm (penetration time of the vertical field $\tau_V = 50$ ms). Therefore, mode stabilization was no more performed by passive means, but by a sophisticated system of 192 (4 poloidally arranged × 48 toroidally arranged, as in Fig. 2.2) feedback-controlled saddle coils [45]. The new machine was called RFX modified (**RFX-mod**) [46] and operated, both in RFP and Tokamak configurations, from April 2004 until October 2015.

In 2015 it was decided to modify the engineering scheme of the saddle coils, and to revise thoroughly the entire front-end system, by removing the vacuum vessel which was the primary source of tearing mode braking. The new machine, which is much more similar now to the twin RFP called MST which is run at the University of Wisconsin, Madison [47], is called RFX modified for the 2$^{\text{nd}}$ time, or **RFX-mod2** [48]: it will likely resume operation in the second half of 2024.

Geometry and plasma features		**Magnetic and Electric fields**	
Major radius	$R_0 = 2$ m	**Plasma current**	50 kA $< I_P \leq 2$ MA
Minor radius	$a = 0.459$ m	**Loop-voltage**	$(10 < V_{loop} < 60)$ V
Vacuum pressure	$(2 < P < 6) \cdot 10^{-11}$ Pa	**Toroidal field**	$B_\varphi^{max} \leq 0.7$ T
Electron density	$(1 < n_e < 10) \cdot 10^{19}$ m^{-3}	**Discharge duration**	50 ms $< \Delta t_{\text{sh.}} < 1$ s
Max. temperature	$T_e^{max} \approx 1.2$ keV		

Table 2.1: Summary of the main properties of the RFX-mod device [46].

RFX-mod is equipped with a rather complete set of devices to measure plasma parameters, called *diagnostics*. For the purposes of this thesis, it is important to mention the two arrays of 72 pick-up coils located at the shell radius, at two different poloidal angles, $\theta = -20.5°$ and $\theta = 159.5°$ [49]. These arrays allow for the reconstruction of the magnetic field perturbations $\delta\vec{B}$ with toroidal mode number $0 \leq n \leq 23$ which are given as input to the code ORBIT (see Section 2.2.2). A picture of RFX-mod is shown in Figure 2.1.

2.1.1 The Optical Camera System

The RFX-mod device was equipped with a set of CCD cameras which covers the first wall of the device both in the toroidal and the poloidal directions. The so-called *Optical Camera System* (OCS) was devoted to the visualisation of the PWI events occurring during the discharges. An example of some images that have been taken by employing this system in the shot # 29324 is reported in Fig. 2.3a. Each camera had an integration time of $\tau_{int} = 2$ ms with a field of view (FOV) of about $\approx 40°$.
Since the first wall of the vacuum chamber is made of tiles that are covered by graphite, at the end of PWI events a large quantity of carbon is freed in the vacuum chamber through a phenomenon known as *sputtering*. Because of the fact that plasma is much colder in the external regions than in the center,

its temperature near the edge is well below the ionisation energy of carbon. A lot of neutral carbon atoms thus enter hotter regions of the plasma and they are ionised. So a good way to experimentally observe PWI is to look at the neutral carbon C-I emission line, at 970 nm, which is also the more intense.

In the new RFX-mod2 it is planned to install 7 new *Basler ace acA720-520um* [50] cameras, which are going to be located as reported in Fig. 2.3b, so as to cover a percentage of the 70% of the total first wall surface, i.e. a total angulation of 260°. Each camera has a pixel dimensions of 6.9 μm × 6.9 μm, a nominal focal distance 12 cm, and a maximum acquisition frequency of 525 frame/s.

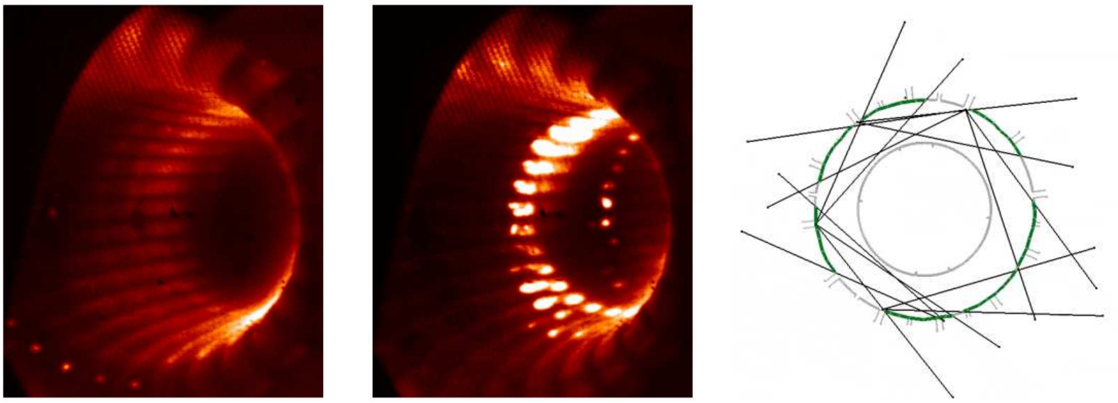

(a) Some photos taken by the OCS during the shot #29324 in RFX-mod.

(b) Camera coverage in RFX-mod2 reconstructed with the CAD software CATIA. View of the toroidal shape from above.

Figure 2.3: The Optical Camera System of RFX-mod and RFX-mod2.

2.2 ORBIT

In this thesis, the properties of magnetic islands, and their overlap generating chaos are examined using a guiding center formalism, valid for frequencies well below the particle cyclotron frequency, ω_c, and cyclotron orbits, ρ, small compared to equilibrium scales. The code suitable for this purpose is ORBIT [2].

2.2.1 Guiding center equations of motion

The code ORBIT was developed during the '80s in `Fortran77` language at the Princeton Plasma Physics Laboratories (PPPL, Princeton, NJ, USA) by Roscoe White and Morrell Chance starting from the guiding center Lagrangian, which was formulated a few years before by Littlejohn [51]. In the code, particles are approximated by their *guiding center*, that is, the center of their circular motion around the magnetic field line. Within this approximation, the particle motion is expressed by the Lagrangian:

$$\mathcal{L} = (\psi + \rho_{\|} I)\dot{\theta} + (\rho_{\|} g - \psi_p)\dot{\zeta} + \mu\dot{\xi} - H \ , \tag{2.1}$$

where the dot $\dot{x}_i$ means a derivative of the coordinate x_i with respect to time t, so $\dot{x}_i = \mathrm{d}x_i/\mathrm{d}t$. $\rho_{\|} = v_{\|}/B$ is the velocity parallel to the magnetic field, or parallel gyroradius, which is normalized with $m_i = 1$ and $e = 1$. μ is the magnetic moment, and ξ is the gyro-phase (see Figure 1.5), while ψ and ψ_p are the toroidal and poloidal magnetic fluxes, respectively. Regarding the fields, g and I are the co-variant components respectively of the toroidal and poloidal fields in the Boozer [52] coordinate system (ψ_p, θ, ζ)[1], where the equilibrium field is given by:

$$\vec{B} = g(\psi_p)\nabla\zeta + I(\psi_p)\nabla\theta + \delta(\psi_p)\nabla\psi_p \ . \tag{2.2}$$

---

[1] The Boozer system is a type of fluz coordinates which can be obtained analytically starting from the more traditional toroidal system (r, θ, φ) sketched in Fig. 1.7.

It can be immediately shown that Eq. (2.1) is equivalent to:

$$\mathcal{L} = P_\theta \, \dot\theta + P_\zeta \, \dot\zeta - H \ , \tag{2.3}$$

where the Hamiltonian is given by:

$$H = \frac{1}{2}\rho_\parallel^2 B^2 + \mu B + \Phi \ , \tag{2.4}$$

with B the magnitude of the magnetic field and Φ the electrostatic potential.
The two conjugate momenta are P_θ and P_ζ, given by:

$$P_\theta = \psi + \rho_\parallel I \tag{2.5}$$

$$P_\zeta = \rho_\parallel g - \psi_p \tag{2.6}$$

While P_θ can vary along a particle orbit, P_ζ is conserved since the system is symmetric along ζ ($\partial B/\partial\zeta = 0$). This can be easily shown by considering the second canonical equation and by taking the derivative of Eq. (2.4) with the assumption of no electrostatic potential, $\Phi = 0$:

$$\dot P_\zeta = -\frac{\partial H}{\partial \zeta} = -(\mu + \rho_\parallel^2 B)\frac{\partial B}{\partial \zeta} = 0 \ . \tag{2.7}$$

This is the well-known theorem by Noether and can be demonstrated explicitly [53]. The consequence is that *for unperturbed, toroidally symmetric systems*, such as a Tokamak or an RFP, *P_ζ is an invariant of the motion.*

The equations for the momenta (Eqs. 2.5-2.6) show that the couple of variables P_θ, P_ζ depend uniquely on the couple of variables $\rho_\parallel, \psi_p$ (since all of the other terms depend on the "radius" ψ_p only, $g = g(\psi_p)$, $I = I(\psi_p)$ and $\partial\psi/\partial\psi_p = q$ with $q = q(\psi_p)$). This means that, when constructing the equations of motion, one can use alternatively the couple (P_θ, P_ζ) or $(\rho_\parallel, \psi_p)$ as two equivalent forms. The choice by White & Chance [2] is to use the couple $(\rho_\parallel, \psi_p)$, in order to avoid an implicit integration scheme in terms of the canonical momenta. In fact, $(\rho_\parallel, \psi_p)$ have an immediate physical explanation, being the parallel energy and the Boozer radial coordinate. To do this, they solve directly the Lagrange equations of motion:

$$\frac{\mathrm{d}}{\mathrm{d}t}\frac{\partial \mathcal{L}}{\partial \dot x_i} = \frac{\partial \mathcal{L}}{\partial x_i} \ , \tag{2.8}$$

with $x_i = \xi, \theta, \zeta$. The first equation, with $x_i = \xi$, shows that the motion along such a direction can be ignored. In fact:

$$\frac{\mathrm{d}}{\mathrm{d}t}\frac{\partial \mathcal{L}}{\partial \dot\xi} = \frac{\mathrm{d}\mu}{\mathrm{d}t} = 0 = \frac{\partial \mathcal{L}}{\partial \xi} \ . \tag{2.9}$$

Eq. (2.9) is zero at all orders, since μ is a constant of motion: this is the reason for using the guiding center formalism. Instead, the non-trivial equations regard θ, ζ (and parallel energy and radius). The derivation of these equations is beyond the purposes of this thesis[2]. For its purpose, it is sufficient to show that the outcome is the following matrix multiplication:

$$\begin{vmatrix} 0 & -A & -C & 0 \\ A & 0 & 0 & I \\ C & 0 & 0 & g \\ 0 & -I & -g & 0 \end{vmatrix} \cdot \begin{pmatrix} \dot\psi_p \\ \dot\theta \\ \dot\zeta \\ \dot\rho_\parallel \end{pmatrix} = \begin{pmatrix} -\partial_{\psi_p} H \\ -\partial_\theta H \\ -\partial_\zeta H \\ -\partial_{\rho_\parallel} H \end{pmatrix} \tag{2.10}$$

The coefficients A, C are functions of the equilibrium fields g and I, and of the safety factor q, as follows:

$$\begin{aligned} A &= q + \rho_\parallel I' \\ C &= \rho_\parallel g' - 1 \end{aligned} \tag{2.11}$$

---

[2] For the interested reader, they are shown in detail in White's book [54].

where the prime symbol $'$ means a derivative with respect to ψ_p, for example $I' = \mathrm{d}I/\mathrm{d}\psi_p$.

The equations of motion (2.10) are in the form $\mathbb{A}\dot{\vec{X}} = Y$, where the matrix $\mathbb{A}$ is skew-symmetric (or anti-symmetric) such that $a_{i,j} = -\delta_{i,j}a_{j,i}$. By definition, the diagonal contains only zeroes. It can be demonstrated that a 4×4 skew-symmetric matrix is equivalent to a symplectic matrix $\mathbb{S}$. Solving a Hamiltonian system is equivalent to inverting a skew-symmetric (or a symplectic) matrix. This is a quite general result of classical mechanics [55].

Hence, the final step to get ORBIT equations is to invert the matrix $\mathbb{A}^{-1}$. To do this, it is necessary to calculate only $n(n-1)/2$ co-factors, and not the original n^2, since the inverse of a skew-symmetric matrix is skew-symmetric.
The determinant of $\mathbb{A}$ is the square of a polynomial in A, g, C, I, which is named the *Pfaffian*, and it is called D (which stands for 'denominator') by White & Chance [2]:

$$D = Ag - IC \ . \tag{2.12}$$

The Pfaffian can be expanded in terms of the field functions as follows:

$$\begin{aligned} D =& g(q + \rho_\parallel I') - I(\rho_\parallel g' - 1) \\ =& gq + I + \rho_\parallel (gI' - Ig') \end{aligned} \tag{2.13}$$

which coincides with the expression of White's book [56]. Finally, it can be easily demonstrated that the inverse matrix is:

$$\mathbb{A}^{-1} = \frac{1}{Ag - IC} \begin{vmatrix} 0 & g & -I & 0 \\ -g & 0 & 0 & C \\ I & 0 & 0 & -A \\ 0 & -C & A & 0 \end{vmatrix} \tag{2.14}$$

Therefore, the final guiding center equations of ORBIT are expressed in compact form as:

$$\begin{pmatrix} \dot{\psi}_p \\ \dot{\theta} \\ \dot{\zeta} \\ \dot{\rho}_\parallel \end{pmatrix} = \frac{1}{Ag - IC} \begin{vmatrix} 0 & g & -I & 0 \\ -g & 0 & 0 & C \\ I & 0 & 0 & -A \\ 0 & -C & A & 0 \end{vmatrix} \cdot \begin{pmatrix} -\partial_{\psi_p} H \\ -\partial_\theta H \\ -\partial_\zeta H \\ -\partial_{\rho_\parallel} H \end{pmatrix} \tag{2.15}$$

To conclude, it is worth noticing that the Pfaffian D shown in Eq. (2.13) should contain derivatives of the non-orthogonal function $\delta(\psi_p)$ which is retained in Boozer coordinates (2.2). It can be shown that the function δ plays no role in the guiding center equations since it determines only a nonsecular change in the motion, which is periodic in the speed of the particle and does not affect the form of the trajectory. Therefore, in ORBIT $\delta = 0$ and is completely neglected [57].

2.2.2 Perturbations in Orbit

The equations of motion sketched in the previous Section do contain the equilibrium field (2.2), only. In this form, they are suited for calculations of neoclassical transport in arbitrary equilibria (RFP, Tokamak, or Stellarator): ORBIT has been used, for example, to study ripple losses of energetic particles in a Tokamak equilibrium [58, 59] or to characterize the poor alpha confinement in a Stellarator equilibrium [60]. But the most interesting results obtained with ORBIT are those where a magnetic perturbation, such as a *tearing mode* or an *Alfvén mode*, is added to the equilibrium.
All tearing and Alfvén modes are perturbations of $\vec{B}$ primarily orthogonal to the original $\vec{B}$. They can be described as having the vector potential with gauge $\delta\vec{A} = \alpha\vec{B}$, i.e.:

$$\delta\vec{B} = \nabla \times \alpha\vec{B} \ , \tag{2.16}$$

where α is an arbitrary scalar function that contains information about all the three radial, poloidal, and toroidal directions [61]. The representation of Eq. (2.16) breaks down with kink modes [62], but we are not interested in this case for the present thesis.

At this stage, it is important to underline that **field perturbations must be given as input to Orbit**. Consequently, the code calculates exact particle motion in an arbitrary field (comprehensive of both equilibrium and perturbations) which is *not* evolved self-consistently. Typical inputs which have been used for studies in the RFX device are:

- the profile of δB_r which is given as output of the 3D, cylindrical viscoresistive MHD code SpeCyl [63];
- the perturbations (a.k.a. eigenfunctions) calculated with Newcomb's equations in toroidal geometry with the code `NCT` [64].

In order to transform the profile of δB_r provided with SpeCyl or `NCT` in the scalar function α, one needs to decompose α in Fourier series, in analogy to what has been already done in Eq. (1.40) for δB:

$$\alpha = \sum_{m,n} \alpha_{m,n}(\psi_p)\ \sin(m\theta - n\zeta + \phi_{m,n})\ . \tag{2.17}$$

Then, by matching equations (2.17) and (1.40), one gets the expression for a single α-harmonic (in cylindrical geometry) as:

$$\alpha_{m,n}(r) = \frac{r\ b^r_{m,n}(r)}{mg + nI}\ , \tag{2.18}$$

as reported for example in the Equation (17) of Ref. [65]. The generalised expression in Boozer coordinates is slightly more complicated [61].

The α profile is very similar to the original δB_r perturbation (which is the main perturbation component for a tearing mode), as it can be seen in Fig. 2.4 for a mode $m = 0$, $n = 4$ in an RFP. Physically, α is the perturbation of the poloidal flux associated with the magnetic island generated by the tearing mode itself.

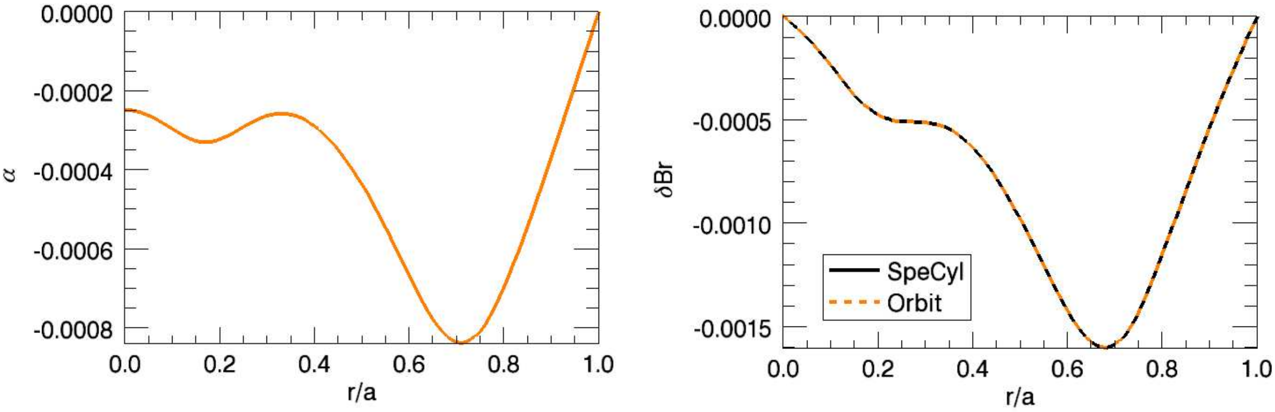

(a) Normalised α radial profile

(b) Normalised δB_r radial profile

Figure 2.4: Comparison between **(a)** α-profile and **(b)** SpeCyl and ORBIT perturbation component for an $m = 0$ $n = 4$ mode. In **(b)** the ORBIT radial component matches the radial perturbation of the SpeCyl run by construction. As expected, the α-profile is very similar to the radial perturbation. The α has dimension m^{-1}, here it is normalized to the major radius R_0. Magnetic perturbations are normalized to the field on the axis. Pictures are taken from Ref. [65].

Extensive verification work has been done in the past to verify the validity of the representation provided by Eq. (2.16) for tearing modes [65]. By benchmarking ORBIT and the volume-preserving field line tracing code NEMATO [66] on the same SpeCyl input, it was shown that the representation with α is perfectly valid for a tearing mode, giving a small error only in the longitudinal component δB_θ which is not relevant for the quantitative description of both conserved and chaotic magnetic fields in the RFP [65].

The advantage of a single scalar function α is that it is straightforward to add it to the guiding center equations of motion (2.15). In fact, formally α is an additive constant to the vector potential, and it can be shown (see on this respect Ref. [67]) that the perturbed equations of motion are obtained from the unperturbed ones (2.15) with the position:

$$\rho_{\parallel} \to \rho_{\parallel} + \alpha \ . \tag{2.19}$$

The canonical momenta are also modified accordingly, and in particular, the toroidal component is modified as follows:

$$P_{\zeta} = (\rho_{\parallel} + \alpha(\psi_p, \theta, \zeta))g - \psi_p \ , \tag{2.20}$$

which adds up a new term in the equation of evolution (2.7) as follows:

$$\dot{P}_{\zeta} = -(\mu + \rho_{\parallel}^2 B)\frac{\partial B}{\partial \zeta} + \rho_{\parallel} B^2 \ \frac{\partial \alpha}{\partial \zeta} \ . \tag{2.21}$$

It is evident from Eq. (2.21) that the new term $\partial\alpha/\partial\zeta$ breaks the toroidal symmetry and, in particular, now $\dot{P}_{\zeta} \neq 0$, which allows magnetic islands [68] to grow and chaos to creep in the system [69].

2.2.3 Calculation of the Connection Length to the wall

In this Section the calculation with ORBIT of the Connection Length to the wall in the case of RFX-mod discharge #29324, at time $t = 218$ ms (that is the case study discussed in Chapters 3, 4, and 5) is briefly described. The equilibrium field is calculated via the μ & p model of Section 1.8.3 in toroidal coordinates, and then it is transformed in Boozer form according to Eq. (2.2).

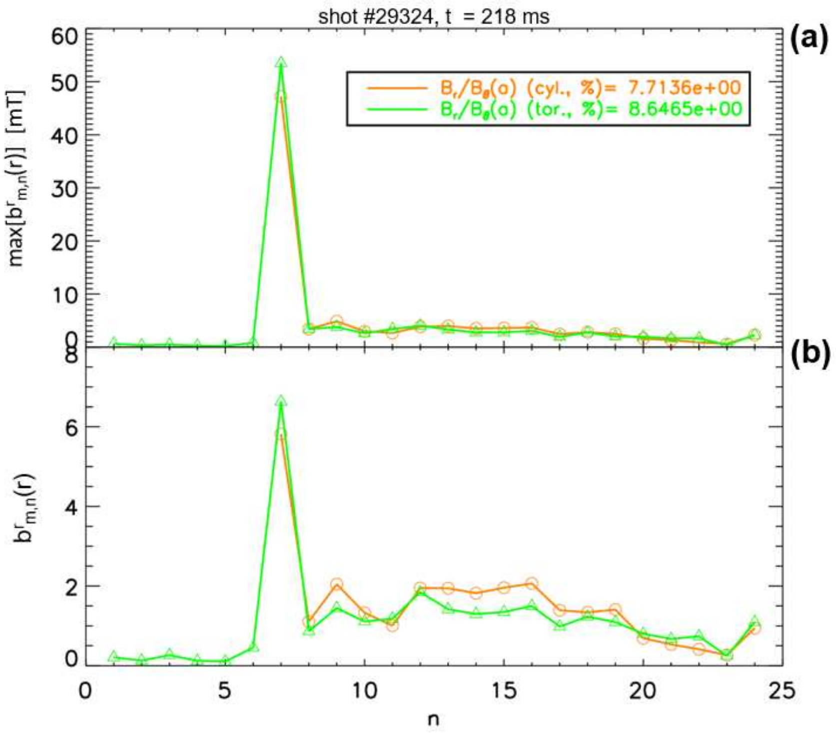

Figure 2.5: Spectrum of $b^r_{m,n}$ for shot #29324 and time $t = 218$ ms, as calculated with `NCT`: **(a)** maximum of the eigenfunction $b^r_{m,n}(r)$, **(b)** edge value $b^r_{m,n}(a)$ for the $m = 1$ modes.

The perturbations are calculated starting from the pick-up coils measurements [49] with the `NCT` [64] code for modes with poloidal mode number $m = 0, 1$ and toroidal mode numbers $0 \leq n \leq 23$. The spectrum of $b^r_{m,n}$ calculated with `NCT` is shown in Fig. 2.5. It is evident the presence of a QSH state where the dominant mode is characterised by $m = 1$, $n = 7$.

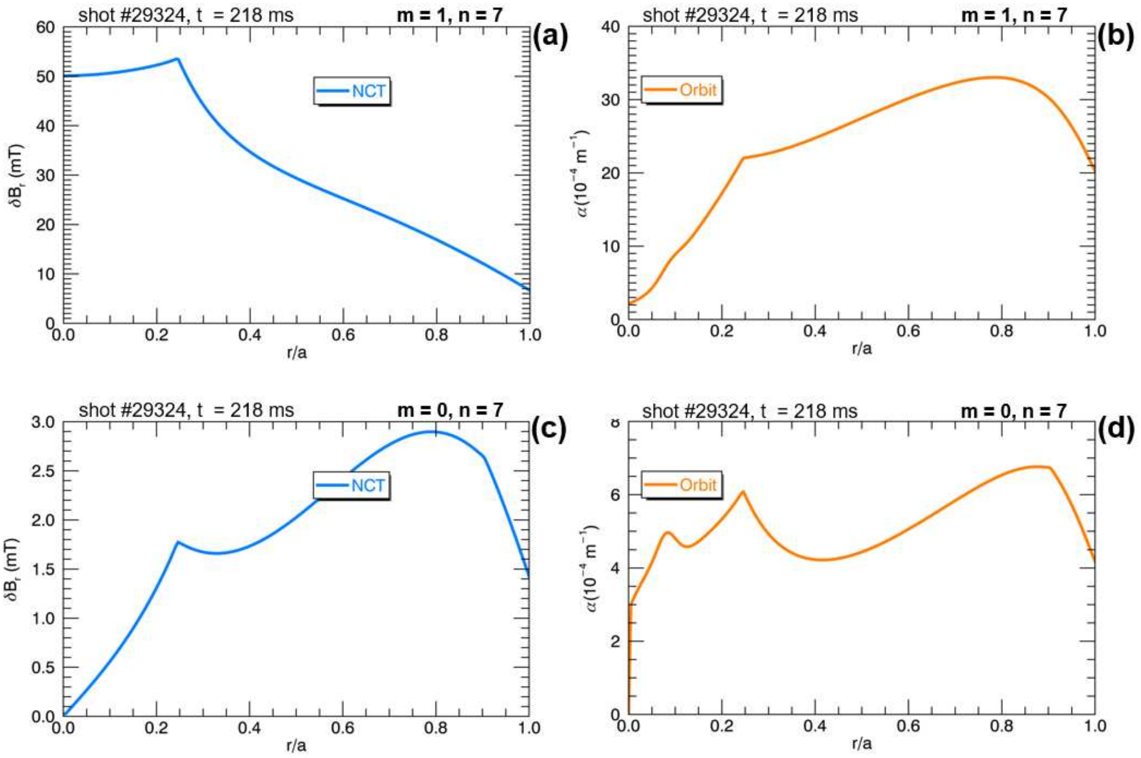

Figure 2.6: Comparison between **(a)** and **(c)**, perturbations (eigenfunctions) calculated with the code `NCT`, and **(b)** and (d), the same perturbations transformed in Orbit as α profiles.**(a)** and **(b)** regard the $m = 1$, $n = 7$ QSH dominant mode, while **(c)** and **(d)** its $m = 0$, $n = 7$ toroidally coupled mode.

The radial profile of the eigenfunctions $b^r_{m,n}(r)$ is then transformed in the scalar function $\alpha_{m,n}(r)$ using Eq. (2.18). An example of profiles of α and δB_r for the QSH mode and $m = 0, 1$ is shown instead in Figure 2.6. It is worth noting that in the RFX-mod the dominant mode of the QSH is characterised by a quite large amplitude, $\delta B_r \approx 50$ mT, corresponding to a scalar $\alpha \sim 10^{-3}$. This value is *one order of magnitude larger* than the typical value of a tearing mode, $\alpha \sim 10^{-4}$ in a tokamak [70]. The toroidally coupled $m = 0$, $n = 7$ mode is order $\epsilon = a/R_0$ smaller, being in the range $\alpha \approx 6 \times 10^{-4}$.

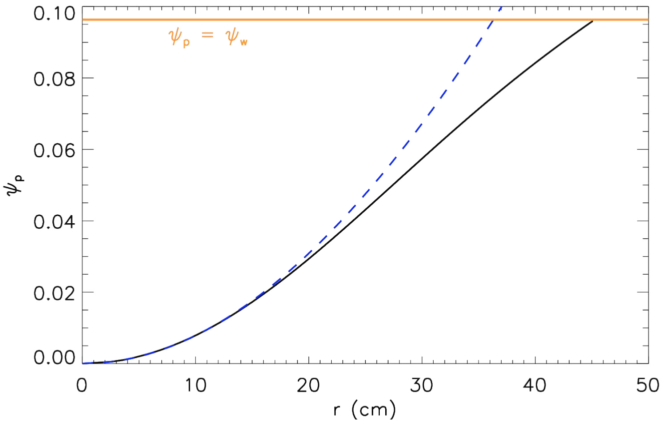

Figure 2.7: Relationship between the Boozer radial coordinate (magnetic poloidal flux) ψ_p and the radial coordinate r, for the shot #29324 and time $t = 218$ ms equilibrium. The dashed line represents the tokamak limiting value $\psi_p = r^2/2q$. The edge value $\psi_w = 0.096$ and corresponds to the geometrical minor radius $r = a$.

An alternative way to represent α in Orbit is to use the Boozer radial coordinate ψ_p (poloidal flux label) instead of the circolar minor radius r. In Orbit the transformation of the Boozer coordinate system into the cylindrical one is straightforward, and it is provided through a file, called `spdata`, which contains the splined equilibrium. Here it suffices to show that the two radial coordinates are linked to the cylindrical poloidal magnetic field $B_\theta^{\mathrm{cyl}} = I/r$ through the relation:

$$\nabla\psi_p = B_\theta^{\mathrm{cyl}}(r)\,\nabla r \ , \tag{2.22}$$

which, by integration, yields:

$$\psi_p(r) = \int_0^r B_\theta^{\mathrm{cyl}}(r)\ \mathrm{d}r \ . \tag{2.23}$$

Since near the origin $B_\theta^{\rm cyl} \approx r/q$, it follows that $\psi_p \approx r^2/2q$, as it is evident in Figure 2.7 for the equilibrium of shot #29324, $t = 218$ ms. The value of ψ_p at the wall is $\psi_w = 0.096$, which is the total poloidal flux, normalized to $B_0^2 R_0$. This value obviously corresponds to the geometric minor radius a, $r(\psi_w) = a$.

Taking into account the sketch reported in Fig. 2.8, the *Connection Length* $L_{c,w}$ is the parallel path along a field line from a given point $(\psi_{p,0}, \theta_0, \zeta_0)$ to the wall $\psi_{p,0} = \psi_{p,w}$, and can be thus formally defined as:

$$L_{c,w}(\psi_{p,0}, \theta_0, \zeta_0) = \int_{\zeta_0}^{\zeta_w} \frac{B\,\mathrm{d}\zeta}{\vec{B} \cdot \nabla\zeta} \,. \qquad (2.24)$$

This definition has already been reported in the Introduction, Eq. (1). The original term 'connection' referred to the length of the magnetic field line which actually *connected* two coils placed at different toroidal angles in the Ergodic Divertor of the TORE Supra Tokamak [26]: the term survived for describing the properties of the stochastic layer in the RMPs literature.

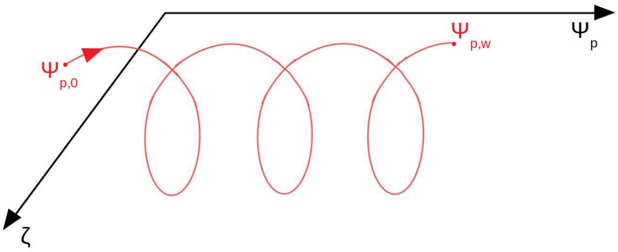

Figure 2.8: Schematic representation of a particle orbit which starts at $(\psi_{p,0}, \theta_0, \zeta_0)$ and ends up to the wall at $(\psi_{p,w}, \theta_w, \zeta_w)$.

In ORBIT, particles with very low energy ($E = 10^{-2}$ eV) are actually considered to represent a field line since, when $\rho_\parallel \approx 0$, a particle follows closely a field line [65]. Moreover, since the edge field of an RFP is chaotic due to the arising of multiple modes whose magnetic islands overlap each other, for a given initial position $(\psi_{p,0}, \theta_0, \zeta_0)$, the Connection Length to the wall is estimated by averaging over a bundle of 1000 particles (field lines), all started at the same initial position. This is repeated in a matrix of initial positions $(\psi_{p,i}, \theta_j, \zeta_k)$ with $i = 8$, $j = 32$ and $k = 64$. Finally a matrix with $8 \times 32 \times 64$ elements is obtained: $\mathbb{L}_{i,j,k} = L_{c,w}(\psi_{p,i}, \theta_j, \zeta_k)$, where each value in the matrix represents the length travelled from the initial point $(\psi_{p,i}, \theta_j, \zeta_k)$ to the wall. Therefore, the matrix $\mathbb{L}_{i,j,k}$ is the output of a grand total 16384 ORBIT simulations.

The $L_{c,w}$ parameter in the RFX-mod edge can vary in between a few centimeters to tens of kilometers [71]. This range is consistent with analogous results found in the edge stochastic layer of Tokamaks and in the island divertor of Stellarators [72].

Chapter 3

Analysis of the Locked Mode in the shot #29324

This Chapter is devoted to the analysis of the magnetic perturbations leading to the Plasma-Wall Interaction reported in Fig. 3.1 [73]. The image has been collected through the fast CCD cameras system of RFX-mod, during the shot #29324, at time $t_{PWI} = 218$ *ms. The image shows two red footprints of a localised emission in the C-I line. The positions of the two stripes of the interaction were measured on the equatorial plane (namely* $\theta = 0$*), respectively at toroidal angles* $\varphi_1 \approx 352^\circ$ *and* $\varphi_2 \approx 7^\circ$ *underlying a mutual toroidal distance of* $\Delta\varphi_S = 15^\circ$*. A preliminary calculation, based on the comparison between the PWI shape and the toroidal profile of the ideal displacement induced by the secondary modes, results in a quantitative estimation of how many modes were involved in the crash event.*

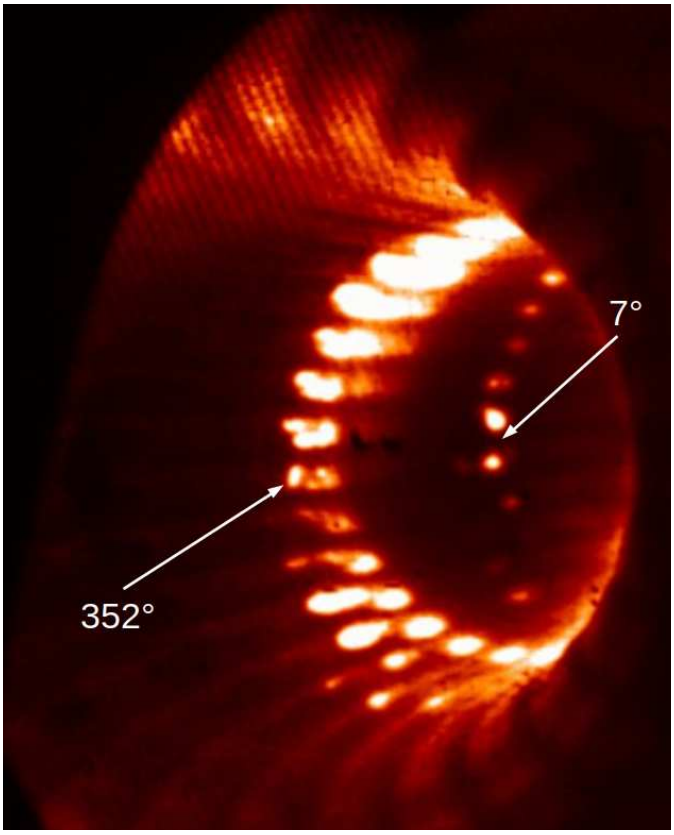

Figure 3.1: Image of the PWI of interest in this work. The image has been taken through a CCD camera during discharge 29324 at time $t_{PWI} = 218$ ms. The two stripes are located on the toroidal plane at $\varphi_1 = 352°$ and $\varphi_2 = 7°$. Taken from Ref. [73].

3.1 Characteristics of the discharge #29324

3.1.1 Magnetic and electrical features of the discharge

The shot #29324 is a typical example of an RFP discharge at high plasma current regime, $\langle I_p \rangle \approx 1.6$ MA. As a matter of fact, both QSH and MH phases are present, in the sense that several transitions from one state to the other can be observed. Its main features are reported in Fig. 3.2. The flat-top condition, i.e. the condition where the plasma current is sufficiently high and stable is highlighted in red in Figs. 3.2a-3.2b. Conventionally, the flat-top condition is set at:

$$\left| \frac{1}{I} \frac{\mathrm{d}I}{\mathrm{d}t} \right| < 10\% \ \mathrm{s}^{-1} \ . \tag{3.1}$$

In the graphs reported in Fig. 3.2, the time instant ($t_{PWI} = 218$ ms) of the PWI of interest is highlighted with a vertical orange line.

By multiplying the mean plasma current $\langle I_p \rangle$ with the mean loop-voltage $\langle V_{loop} \rangle$, one concludes that, on average, the injected power during the discharge was of about $\langle P_{\mathrm{input}} \rangle \approx 50$ MW. Furthermore, regarding the electronic density (3.2c), it can be easily noticed that, during the whole discharge, n_e stays well below the experimental Greenwald $n = n_G$ limit, calculated as in Eq. (1.47). The mean ratio between the two quantities is $\langle n_e/n_G \rangle = 0.119$. These properties are enough to justify the relatively long-lasting (about 200 ms) of the flat-top phase.

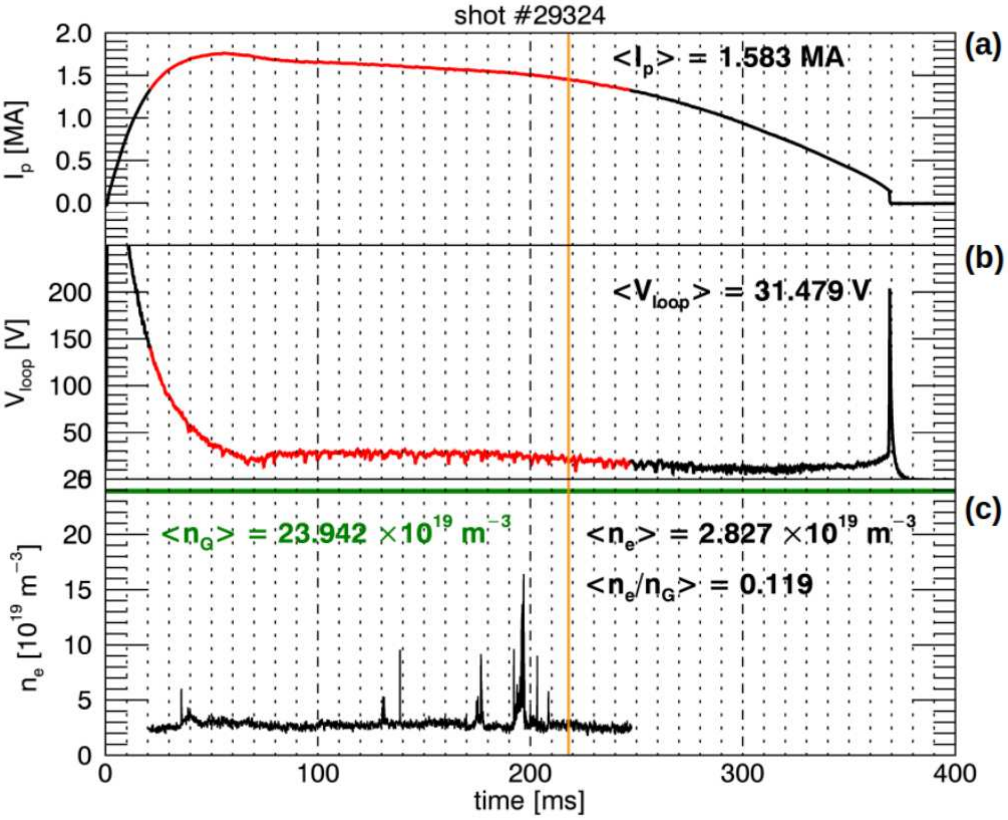

Figure 3.2: Evolution of the discharge #29324's main features: **(a)** the plasma current I_p, and **(b)** the loop-voltage V_{loop}, i.e. the voltage difference applied to make plasma current flowing in the toroidal direction. In **(a)** and **(b)** the flat-top phase is highlighted in red. In **(c)** the evolution of the numerical electronic density during the flat-top phase is shown. In this graph, Greenwald's limit is reported through a green line. Whereas, the orange vertical line highlights the time instant, $t_{PWI} = 218$ ms, corresponding to the PWI of interest. The discharge duration is about 400 ms. Its evolution can be divided in three main parts: the lighting (until $t \approx 20$ ms) when plasma is accelerated by applied V_{loop}. In the subsequent flat-top phase ($(20 < t < 250)$ ms) both I_p and V_{loop} stabilise. For $t > 250$ ms discharge slowly terminates.

Moreover, from the observation of the graphs in Fig. 3.3, further information about the magnetic configuration at the moment of the interaction can be easily deduced. For instance, in 3.3a the radial profile of the toroidal (B_φ) and the poloidal (B_θ) magnetic field components is shown. As we expected for a typical RFP discharge, B_φ's sign was negative at the edge. By looking at the radial profile of the safety factor ($q(r)$) in 3.3b, one can notice that several instabilities were radially resonating in the plasma depending on the rational values assumed by q.

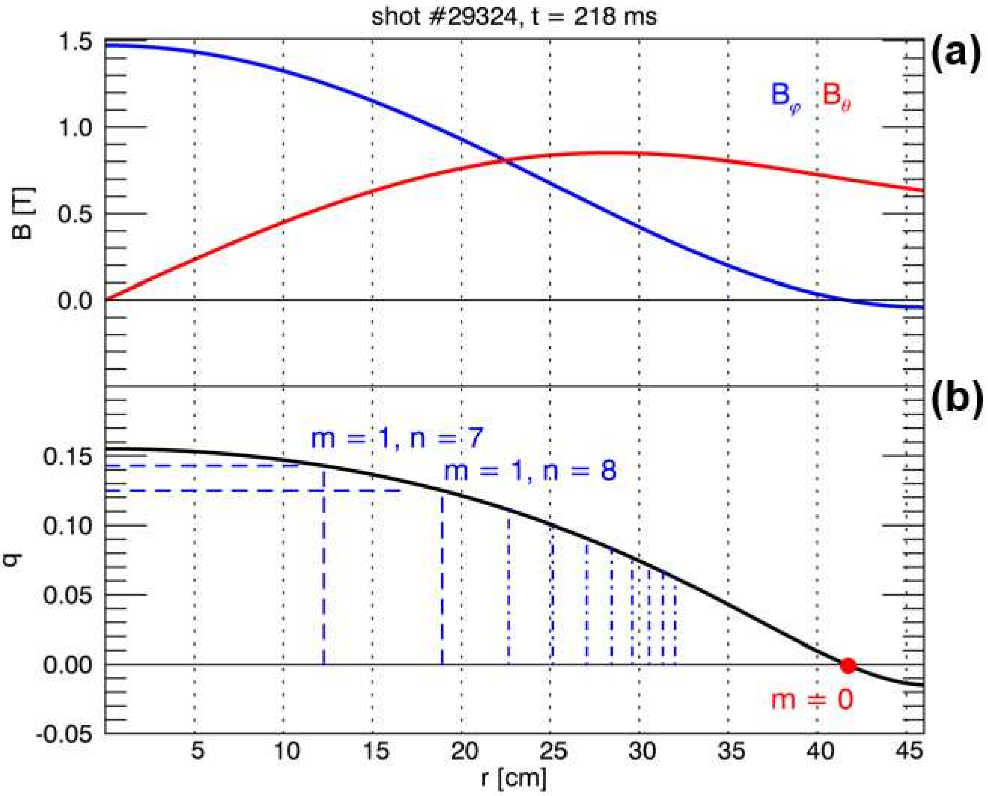

Figure 3.3: Magnetic characterisation of the shot #29324 at $t = t_{PWI}$: **(a)** the magnetic field components radial profile, **(b)** the safety factor radial profile. q rational values, corresponding to the radial positions of the magnetic surfaces associated with tearing modes, are highlighted.

3.1.2 Crash characterisation

Since, as it has been just said, during shot # 29324, many resonances populated radially the plasma, some crashes have occurred. In Fig. 3.4, similarly to what has been already done in Section 1.9.2, the evolution of the main parameters characterising the phenomenology of the plasma relaxation during a short time interval around the interesting event at $t = t_{PWI}$ is reported. The PWI's time instant is highlighted with a vertical orange line. A vertical blue line indicates the time instant $t = 221$ ms. The two lines indicate two different kinds of crashes. Concerning the blue line, most of the relevant quantities like q_0, Θ, and F are characterised by a strong variation correspondingly to the time instant of the crash. A strong decrease of the dominant mode amplitude follows soon in a few milliseconds[1]. This description is compatible with the notion of a major crash. In fact, the plasma helicity is almost completely lost during the event as the graph of the modes amplitudes evolution in Fig. 3.4d clearly confirms. On the contrary, in the same graph one can see that, at $t = t_{PWI}$, even if the dominant mode slightly decreases, the QSH state survives, i.e. the mode $m = 1$, $n = 7$ remained dominant after the plasma relaxation. In fact the $m = 1$ spectrum at $t = 218$ ms is shown in Fig. 2.5, and it is a typical QSH spectrum. As a consequence, the DRE observed in Fig. 3.1 is the consequence of a minor crash. In the remainder of the thesis we will concentrate on the minor crash at $t_{PWI} = 218$ ms.

---

[1] Take into account that the pick-up coils are placed outside the vacuum vessel so that the signal in Fig. 3.4d is attenuated and delayed.

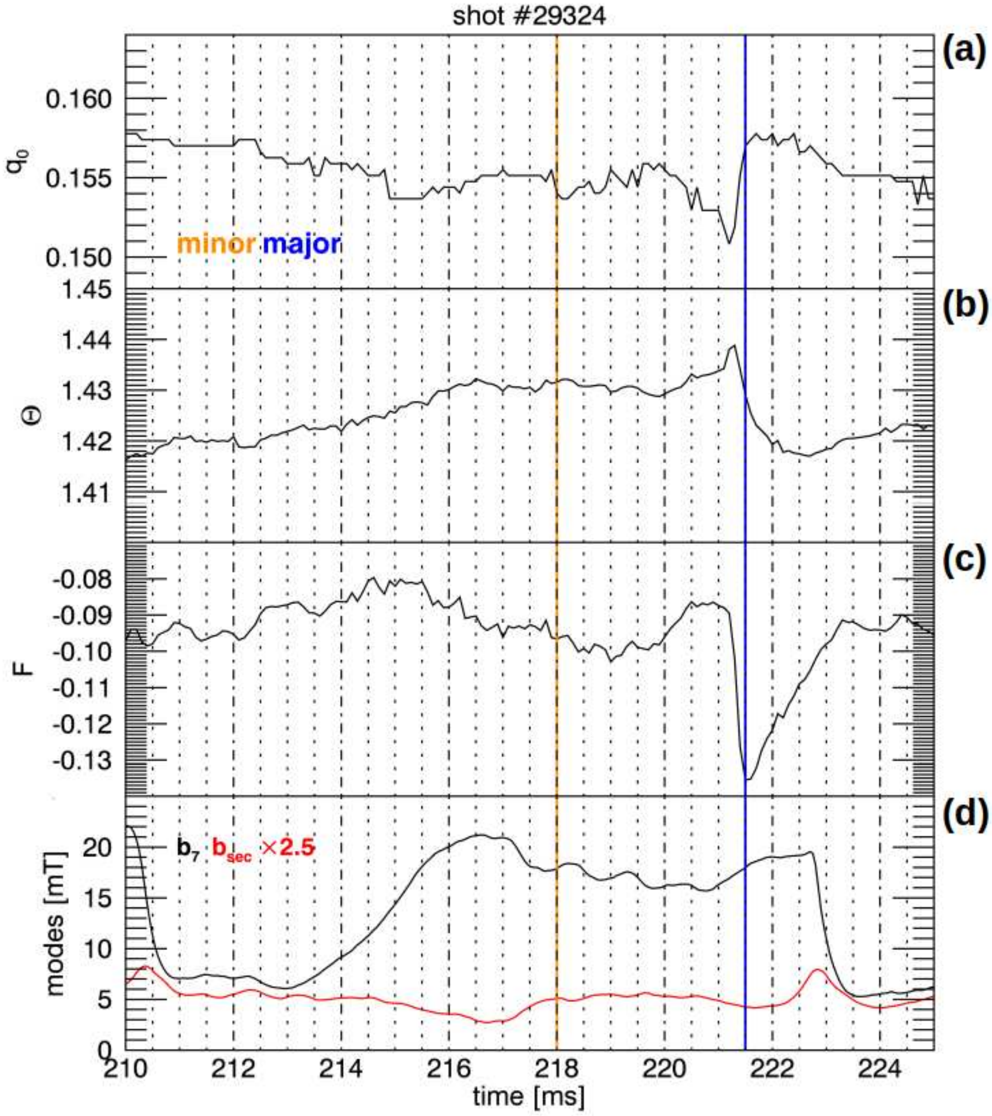

Figure 3.4: Evolution of main parameters during a short time interval around $t = t_{PWI}$: **(a)** safety factor at the center q_0, **(b)** pinch parameter Θ, **(c)** reversal parameter F, **(d)** amplitude of $m = 1$ modes. Time instant $t = t_{PWI}$ is highlighted with a vertical orange line. Whereas, a vertical blue line underlines the time instant $t = 221$ ms.

3.2 The Locked Mode

During a plasma discharge, a mechanism of non-linear coupling between tearing modes resembling constructive interference occurs [74]. The main consequence of such a mode coupling is the formation of a toroidally localised deformation called *Locked Mode* [75] (LM). The locking phenomena regards mainly the $m = 1$ modes, even if a $m = 0$ locking is also observed [64]. In the remainder of the thesis, we will refer always to $m = 1$ locking. In this section, some useful parameters to describe this phenomenon are introduced.

3.2.1 The inverse-sigma and the Locking-Strength parameters

The helical phase of a generic resonating mode (m, n) can be written as in Eq. (2.18):

$$\Phi_{m,n}(\theta, \varphi, t) = m\theta - n\varphi + \phi_{m,n}(t) \ ,$$

where $\phi_{m,n}$ indicates the FFT phase of the mode (m, n).
For sake of simplicity, consider here to focus on the equatorial plane ($\theta = 0$) so as to work with only

one degree of freedom. Then, the resulting helical phase of the (m, n) mode is given by:

$$\Phi_{m,n}\left(\varphi, t\right) = n\varphi + \phi_{m,n}(t) \ .$$

According to Ref. [76], the degree of alignment of the modes is studied by calculating the *inverse-sigma parameter*, σ^{-1}, where σ is defined as:

$$\sigma_M(\theta, \varphi, t) = \frac{1}{1 + 2 + \cdots + (n_{max} - n_{min})} \sum_{j=n_{min}}^{n_{max}-1} \sum_{k=j+1}^{n_{max}} \left| \sin\left(\frac{\Phi_{m,j}(\theta, \varphi, t) - \Phi_{m,k}(\theta, \varphi, t)}{2} \right) \right| \ , \tag{3.2}$$

where n_{max} and n_{min} respectively represent the range of toroidal mode numbers which interact together. A simplified version of the quantity above is obtained by focusing the attention only on the $m = 1$ modes, which are those driving the DREs in RFX-mod:

$$\sigma_M(\varphi, t) = \frac{1}{1 + 2 + \cdots + (n_{max} - n_{min})} \sum_{j=n_{min}}^{n_{max}-1} \sum_{k=j+1}^{n_{max}} \left| \sin\left(\frac{\Phi_{1,j}(\varphi, t) - \Phi_{1,k}(\varphi, t)}{2} \right) \right| \ . \tag{3.3}$$

Such an expression for σ was inspired by a precedent definition given by Kusano, Tamano, and Sato in Ref. [75]:

$$\sigma_{KTS}(\varphi, t) = \sqrt{\frac{\sum_{j=n_{min}}^{n_{max}} \left[\Phi_{1,j}(\varphi, t) - \langle \Phi(\varphi, t) \rangle_1 \right]^2}{N_{sum}}} \ .$$

Where $\langle \Phi(\varphi, t) \rangle_1$ indicates the $m = 1$ modes helical phases average, while N_{sum} is the number of modes taken into account: $N_{sum} = n_{max} - n_{min} + 1$. The latter expression for σ clarifies which is its meaning. In fact, since the formula above corresponds formally to the calculus of the r.m.s. of the phases sample $\{\Phi\}_{1,j}$, σ represents a measure of the overall dispersion of the modes phases set.
The inverse-sigma σ^{-1} is particularly effective in quantitatively describing the quality of the modes locking, namely the condition where the modes are aligned sharing the same helical phase. In fact, where and when the plasma is in the LM, i.e. when the coupled modes are aligned, both $\sigma_M(\varphi, t)$ and $\sigma_{KTS}(\varphi, t)$ go to zero. Correspondingly, σ^{-1} diverges.

An alternative way to quantify the *strength* of the Locked Mode is to calculate the so-called *Locking-Strength* parameter [74, 77], which is defined as the normalized sum over the main interacting modes of their mutual phase difference cosine:

$$\mathrm{LS}(\varphi, t) = \frac{1}{1 + 2 + \cdots + (n_{max} - n_{min})} \sum_{j=n_{min}}^{n_{max}-1} \sum_{k=j+1}^{n_{max}} \cos\left[\Phi_{1,j}(\varphi, t) - \Phi_{1,k}(\varphi, t)\right] \ . \tag{3.4}$$

The main difference between the Locking-Strength, LS, and the inverse-sigma, σ^{-1}, parameters is that, whereas the latter diverges in the LM, the first tends to 1. In fact, by imposing $\Phi_{1,j}(\varphi, t) = \text{cost.}\ \forall j$, we have for a complete locking condition[2]:

$$\begin{aligned} \mathrm{LS}(\varphi, t) &= \frac{1}{1 + 2 + \cdots + (n_{max} - n_{min})} \sum_{j=n_{min}}^{n_{max}-1} \sum_{k=j+1}^{n_{max}} 1 \\ &= \frac{1}{1 + 2 + \cdots + (n_{max} - n_{min})} \cdot \left[1 + 2 + \cdots + (n_{max} - n_{min})\right] = 1 \ . \end{aligned}$$

LS $= 0$ corresponds instead to the absence of a Locked Mode and random phases.
However, since both reach their maximum in the Locked Mode, *LS and σ are equivalent.* The LS has the advantage of being bounded in the interval $[0, 1]$. Therefore, it was preferred over σ over σ in the present thesis and in the RFX-mod database [74].

---

[2] The calculation is justified with the fact that, if $j = n_{max} - 1$ then k can assume just one value: $k = n_{max}$. If $j = n_{max} - 2$, then k can assume 2 values, and so on so forth until $j = n_{min}$, then k can assume all values between $n_{min} + 1$ and n_{max}, that are $n_{max} - n_{min}$.

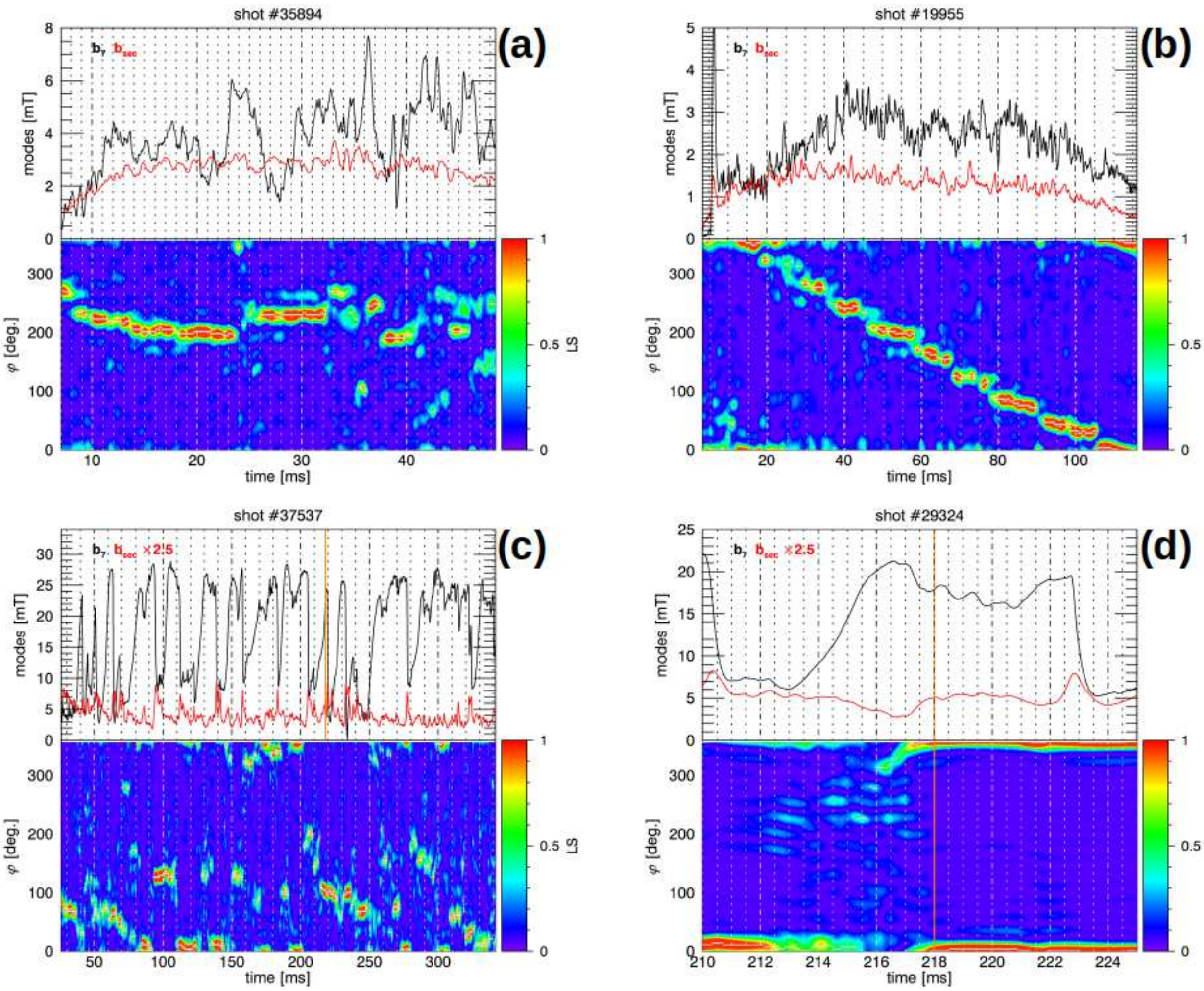

Figure 3.5: Examples of locked mode configurations compared to the modes amplitude evolution: **(a)** wall-locking (#35894), **(b)** phase-locking (#19955), **(c)** no wall-locking (#37537), **(d)** Locked-Mode shape in the shot #29324 of interest in this work. The orange line indicates the time instant $t = t_{PWI}$. In the figure LS has been calculated with $n_{min} = 7$ and $n_{max} = 23$.

In principle, by associating the maximum of the parameter $\mathrm{LS}(\varphi, t)$ to the toroidal position of the LM, $\varphi_{\text{lock}}(t)$, one can observe the time evolution of the LM during the discharge. In this sense, two main configurations are found. In the first case, the LM is *wall-locked* (Fig. 3.5a), since its toroidal coordinate does not change in time. This is the typical pattern of the LM evolution as it occurred in the old RFX device [78], where the feedback coil system was not available. In the second case, a rotation of the LM was induced by a proper setting of the feedback system (Fig. 3.5b), this state is called simply as *phase-locking* [79]. Wall-locking is the worst case, being responsible for the enhanced localised PWI, which might induce overheating of the PFC, anomalous impurity influx (sputtering), and radiation the so-called *Carbon bloom* [80]). On the contrary, the best case for what concerns the integrity of the first wall is when the QSH is well sustained during the discharge and wall-locking is not observed (Fig. 3.5c). This observation is confirmed by Fig. 3.6, where the evolution of the mode amplitude **(a)** is compared to the one of the LS **(b)** and it is noticed that the growth of the secondary modes is consequently followed by their alignment, since LS increases. In fact, in the figure just reported it can be easily seen that LS never reaches its maximum value (LS = 1) during the entire flat-top time interval of the discharge.
As concerns the DRE of interest at $t = t_{PWI}$, the contour plot in Fig. 3.5d clearly shows that the LM is wall-locked at a toroidal coordinate around $\varphi_{\text{lock}} = 0$. It is worthy to say that this conclusion is compatible with what has been previously reported by Scarin et al. in Ref. [73].

3.3 Comparison with the ideal displacement

3.3.1 Analytic version of LS through Dirichlet kernels

Assume that the helical angles of the modes are constant, $\phi^{m,n} = \text{cost.}$, which is equivalent to moving in the frame of reference where the LM is at rest at $\varphi_{\text{lock}} = 0$ [82]. Then, $\text{LS}(\varphi)$ in Eq. (3.4) becomes:

$$\text{LS}(\varphi) = \frac{2}{N \cdot (N+1)} \sum_{j=n_{min}}^{n_{max}-1} \sum_{k=j+1}^{n_{max}} \cos\left[(j-k)\varphi\right] ,$$

where $N = n_{max} - n_{min} = N_{sum} - 1$.
By calling $\ell = k - j$, the formula above can be re-written as:

$$\text{LS}(\varphi) = \frac{1}{N+1} \sum_{\ell=0}^{N} \cos\left(\ell\varphi\right) , \tag{3.5}$$

where such a normalization has been introduced in order to fulfill the prescription $\text{LS} = 1$ at its maximum.

The sum of cosine functions that appears in Eq. (3.5) is a known mathematical object: the *Dirichlet kernel*. It is formally defined as follows:

$$D_N(x) = \sum_{k=-N}^{N} e^{ikx} = 1 + 2\sum_{k=1}^{N} \cos\left(kx\right) = \frac{\sin\left[\left(N+\frac{1}{2}\right)x\right]}{\sin\left(\frac{x}{2}\right)} . \tag{3.6}$$

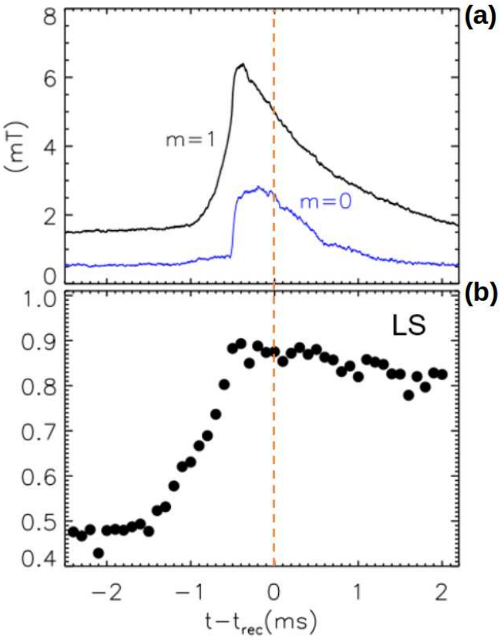

Figure 3.6: The picture is taken from Ref. [81] and is obtained by averaging over many RFX-mod shots. The time instant of the reconnection event, t_{rec}, is highlighted with an orange dashed vertical line.

By comparing Eq. (3.5) with the definition of the Dirichlet kernel in Eq. (3.6), one can get an analytic expression for $\text{LS}(\varphi)$:

$$\begin{aligned}
\text{LS}(\varphi) &= \frac{1}{N+1} \sum_{\ell=0}^{N} \cos\left(\ell\varphi\right) \\
&= \frac{1}{N+1} \left[1 + \sum_{\ell=1}^{N} \cos\left(\ell\varphi\right)\right] \\
&= \frac{1}{N+1} \left[1 + \frac{1}{2}\left(D_N(\varphi) - 1\right)\right] \\
&= \frac{1}{2(N+1)} \left[1 + D_N(\varphi)\right] .
\end{aligned}$$

And finally:

$$\text{LS}(\varphi) = \frac{1}{2(N+1)} \left[1 + \frac{\sin\left[\left(N+\frac{1}{2}\right)\varphi\right]}{\sin\left(\frac{\varphi}{2}\right)}\right] . \tag{3.7}$$

It can be verified that $\text{LS}(\varphi)$ given in this way respects the property to be equal to 1 at its maximum. Such an expression for $\text{LS}(\varphi)$ depends on the parameter N. By looking at Fig. 3.7, one notices that, by increasing N, the peak at $\varphi = 0$ in the $\text{LS}(\varphi)$ profile shrinks.

3.3.2 Definition of the ideal displacement

For sake of simplicity, consider working in the approximation where the resistivity of the plasma is ignored. The local *ideal displacement* $\Delta_{m,n}$ (hereafter it is going to be called also *shift*) associated to the (m,n) mode depends on the perturbed radial field $b^r_{m,n}(r)$ through the relation [83]:

$$\Delta_{m,n} = \frac{i\; r b^r_{m,n}\; e^{i(m\theta - n\varphi + \phi_{m,n})}}{(m - n\cdot q(r)) B^0_\theta(r)} \; , \qquad (3.8)$$

where m, n, and $q(r)$ are respectively the poloidal mode number, the toroidal mode number, and the safety factor profile. Instead, B^0_θ is the poloidal magnetic field at the equilibrium. The formula above is obtained by taking into account a cylindrical approximation. It diverges at the resonance, but this is not a problem since $\Delta_{m,n}$ is evaluated at the plasma edge in this section. The perturbation $b^r_{m,n}$ are calculated by the `NCT` code as explained in Chapter 2. The total shift of the magnetic field lines generated by secondary modes is then calculated as $\Delta_{sec} = \sum_{n=8}^{23} \Delta_{1,n}$.

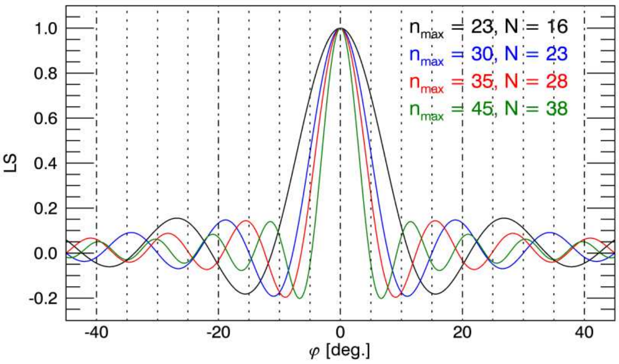

Figure 3.7: Examples of several LS(φ) profiles obtained by varying N.

The idea is that the position of the two stripes characterising the PWI in Fig. 3.1 should almost correspond to the maximum deformation induced by all the perturbations together, i.e. the maxima of $\Delta_{sec}(\varphi)$.

Fig. 3.8 compares the LS profile in the LM reference system, as described by Eq. (3.7), with the toroidal profile of the ideal shift, $\Delta_{sec}(\varphi)$, calculated by taking $\theta = 0$. It is shown that the positions of the two peaks of $\Delta_{sec}(\varphi)$ ($\varphi_1^\Delta = 351°$ and $\varphi_2^\Delta = 16°$), in particular the second one, differ with respect to the ones measured in Ref. [73], φ_1 and φ_2, see Fig. 3.1. A possible reason for this difference is that the ideal displacement is calculated using experimental data associated with the $m = 1$ modes with $n \leq 23$. Therefore, by considering more modes in the calculation of Δ_{sec}, a better agreement should likely be found.

3.3.3 Deduction of n_{max} causing PWI in #29324 at $t = t_{PWI}$

From the comparison reported in Fig. 3.8 a link between the positions of the first two minima of LS and the maxima of the deformation indicating the position of the two PWI stripes is deduced. Since in Eq. (3.7) an analytic version of LS has been already provided, in principle one can deduce the position of the first two minima of LS(φ) as a function of N analytically. Then, since N depends on the toroidal numbers of the modes interacting in the DRE at $t = t_{PWI}$, by imposing that the two minima are found in the positions experimentally measured ($\varphi_1 \approx 352°$ and $\varphi_2 \approx 7°$, $\Delta\varphi_S = 15°$), a first estimate of how many modes were involved in the PWI of interest can be found.

LS(φ) is an even function:

$$\mathrm{LS}(-\varphi) = \frac{1}{2(N+1)}\left[1 + \frac{\sin\left[\left(N+\frac{1}{2}\right)(-\varphi)\right]}{\sin\left(-\frac{\varphi}{2}\right)}\right] = \frac{1}{2(N+1)}\left[1 + \frac{\sin\left[\left(N+\frac{1}{2}\right)\varphi\right]}{\sin\left(\frac{\varphi}{2}\right)}\right] = \mathrm{LS}(\varphi)\;,$$

so the distance $\Delta\varphi$ between the two first minima of LS(φ) can be written as: $\Delta\varphi = 2\hat{\varphi}$ where $\hat{\varphi}$ is the position of the first minimum such that $\hat{\varphi} > 0$. It follows that the analytic profile of LS(φ) which describes the discharge #29324 at the time $t = t_{PWI}$, must have the first minimum at $\varphi_S = \Delta\varphi_S/2 = 7.5°$.

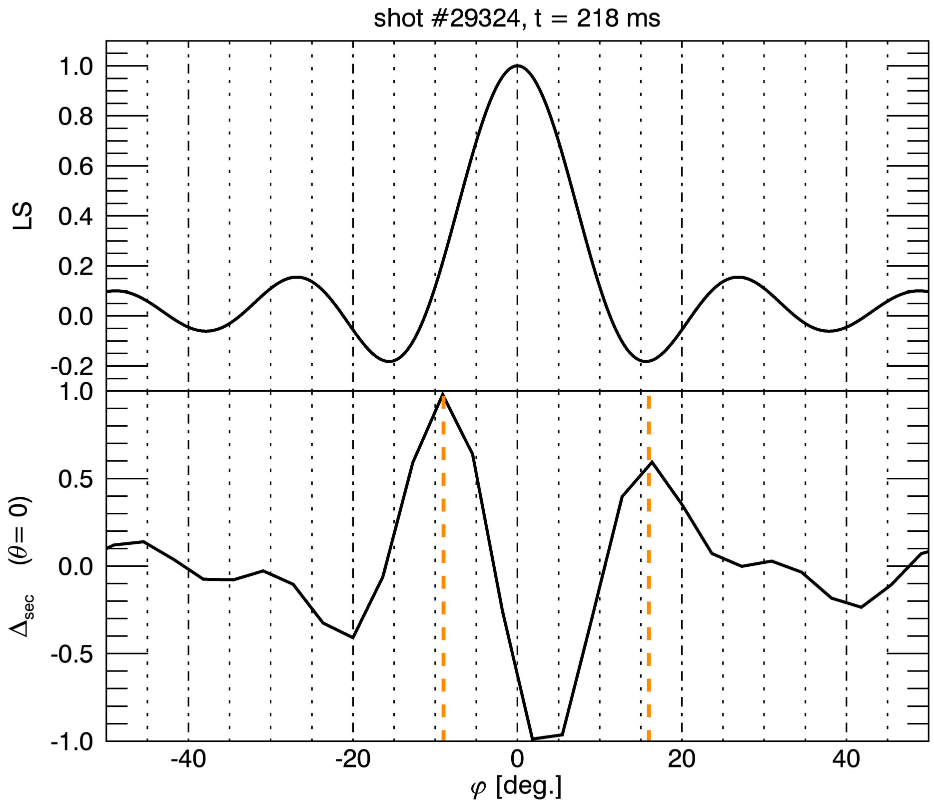

Figure 3.8: Comparison between **(a)** $m = 1$ LS(φ) and **(b)** $\Delta_{sec}(\varphi)$ for the discharge #29324 at $t = t_{PWI}$ calculated at $\theta = 0$. The orange dashed vertical lines highlight the two maxima of the ideal displacement Δ_{sec}.

The derivative of LS(φ) in Eq. (3.7) is given by:

$$\frac{\mathrm{dLS}(\varphi)}{\mathrm{d}\varphi} = \frac{1}{2(N+1)}\left[\frac{\cos\left[\left(N+\frac{1}{2}\right)\varphi\right]\cdot\left(N+\frac{1}{2}\right)}{\sin\left(\frac{\varphi}{2}\right)} - \frac{\sin\left[\left(N+\frac{1}{2}\right)\varphi\right]}{2\sin^2\left(\frac{\varphi}{2}\right)}\cdot\cos\left(\frac{\varphi}{2}\right)\right] . \tag{3.9}$$

By evaluating the equation above at the minimum $\varphi = \hat{\varphi}$, it becomes:

$$\cos\left[\left(N+\frac{1}{2}\right)\hat{\varphi}\right]\cdot\sin\left(\frac{\hat{\varphi}}{2}\right)\cdot\left(N+\frac{1}{2}\right) - \frac{1}{2}\sin\left[\left(N+\frac{1}{2}\right)\hat{\varphi}\right]\cdot\cos\left(\frac{\hat{\varphi}}{2}\right) = 0 . \tag{3.10}$$

By imposing the experimental result: $\hat{\varphi} = \varphi_S$, one gets the following equation in the variable N:

$$\cos\left[\left(N+\frac{1}{2}\right)\varphi_S\right]\cdot\sin\left(\frac{\varphi_S}{2}\right) - \sin\left[\left(N+\frac{1}{2}\right)\varphi_S\right]\cdot\cos\left(\frac{\varphi_S}{2}\right) = -2N\cos\left[\left(N+\frac{1}{2}\right)\varphi_S\right]\cdot\sin\left(\frac{\varphi_S}{2}\right) . \tag{3.11}$$

By considering the following trigonometric identities:

$$\sin(\alpha-\beta) = \sin(\alpha)\cos(\beta) - \cos(\alpha)\sin(\beta)$$
$$\cos(\alpha-\beta) = \cos(\alpha)\cos(\beta) - \sin(\alpha)\sin(\beta)$$

the Eq. (3.11) becomes:

$$\sin(N\varphi_S) = 2N\left[\cos(N\varphi_S)\cdot\cos\left(\frac{\varphi_S}{2}\right) - \sin(N\varphi_S)\cdot\sin\left(\frac{\varphi_S}{2}\right)\right]\cdot\sin\left(\frac{\varphi_S}{2}\right) \tag{3.12}$$

$$\tan(N\varphi_S)\left[\frac{1}{2N\sin^2\left(\frac{\varphi_S}{2}\right)}+1\right] = \frac{1}{\tan\left(\frac{\varphi_S}{2}\right)} \qquad (\star) . \tag{3.13}$$

By approximating $\frac{1}{2N\sin^2\left(\frac{\varphi_S}{2}\right)} + 1 \approx 1$, one has:

$$\tan(N\varphi_S) = 2N\cos\left(\frac{\varphi_S}{2}\right)\cdot\sin\left(\frac{\varphi_S}{2}\right) = N\sin\varphi_S . \tag{3.14}$$

φ_S is supposed to be small such that $\varphi_S \approx \sin\varphi_S$. Finally, the equation above can be written as:

$$\tan\left(N\varphi_S\right) = N\varphi_S \qquad \Rightarrow \qquad \tan x = x \ , \tag{3.15}$$

where the passage consists of a change of variable (namely $x = N\varphi_S$). This equation can be finally solved graphically, obtaining:

$$x \approx 4.5 \qquad \Rightarrow \qquad N \approx 34 \qquad \Rightarrow \qquad n_{max} \approx 41 \ . \tag{3.16}$$

The first confirmation of the goodness of such an analytical derivation comes from Fig. 3.9 which reports the comparison between $\Delta\varphi$ numerically calculated as the distance between the two first minima in the LS(φ) profile by using n_{max} as a free parameter and the experimentally measured $\Delta\varphi_S$.

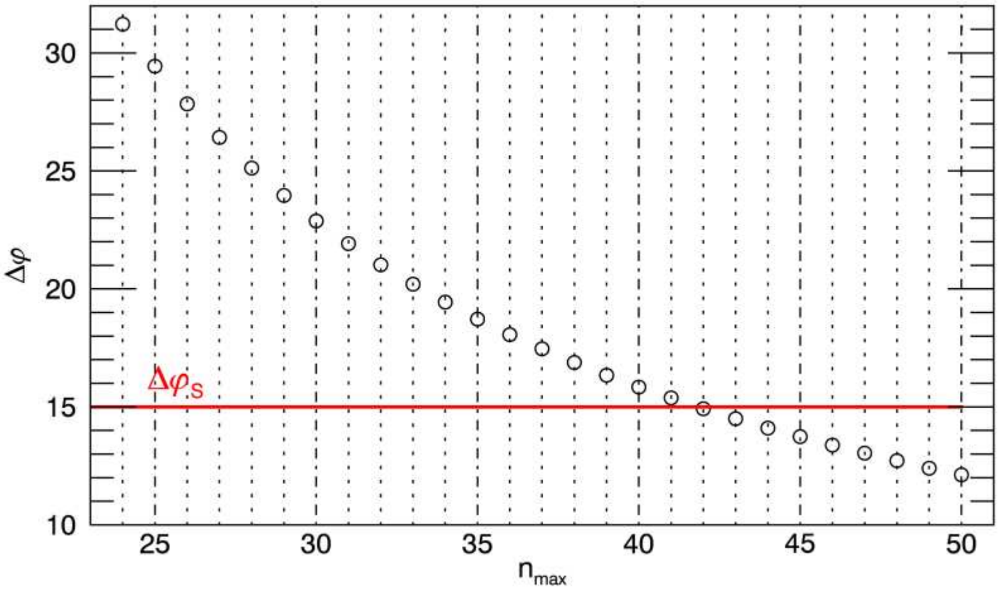

Figure 3.9: Comparison between **(a)** $\Delta\varphi$ computationally calculated by varying n_{max} into the expression of LS given by Eq. (3.7) and **(b)** the distance between emission footprints $\Delta\varphi_S$ measured in Ref. [73].

The physical interpretation of the result just obtained is that, during the shot # 29324, at $t = t_{PWI}$, the plasma should have been populated by all tearing modes with $m = 1$ and $7 < n < 41$ (well beyond the $n_{max} = 23$ the feedback system of RFX-mod can detect), which non-linearly have interacted with each other, locking their phases and stopping at $\varphi_{\text{lock}} = 0$. The two footprints of the PWI resemble the shape of the plasma spatially resulting from the coupling between modes. The importance of this result is that it can be used as a preliminary prescription for the implementation of the future RFX-mod2 experiment with an improved feedback system of coils so as to be able to control the modes characterised by higher toroidal mode numbers, approximately until $n = 41$ [48].

Chapter 4

Description of the magnetic topology during PWI through Poincaré plot

This Chapter is devoted to a more refined way to study PWI events like the one of interest in this thesis. It deals with the description of the plasma magnetic topology at the crash. The kind of map which is considered is the so-called Poincaré plot*. In this way, the real radial displacement of the magnetic field lines due to the tearing modes arising in the plasma at $t = t_{PWI}$ is directly visualised and compared with the results of the previous Chapter. In the end, the role played by the $m = 0$ magnetic islands during the event is clarified.*

4.1 Poincaré plot definition

Considering a dynamical system, a simple way to represent the trajectory followed by a given particle is to record the intersection of its orbit with a surface, which must be perpendicular to the dynamical flux. The collection of the intersections is called *Poincaré plot.*

The formal definition can be found in Ref. [84]: the *Poincaré section* is a surface $F(x, y, z) = 0$ on which there is no real point that satisfies:

$$\frac{\partial F}{\partial x}\dot{x} + \frac{\partial F}{\partial y}\dot{y} + \frac{\partial F}{\partial z}\dot{z} = 0 \ , \tag{4.1}$$

and so F is not tangent to any trajectory.
In other words, the Eq. (4.1) is equivalent to:

$$\vec{v} \cdot \nabla F(x, y, z) \neq 0 \quad \forall (x, y, x) \ , \tag{4.2}$$

i.e. the velocity of each particle is never tangent to the surface for any point of F. By looking at the sketch in Fig. 4.1 and by taking into account the Eqs. (4.1)-(4.2), one easily concludes that the vector which is represented in blue ($\vec{v}_1$) is a trajectory that can be considered as compatible with the definition of F as a Poincaré section. The opposite happens for the vector $\vec{v}_2$ represented in red. In this thesis, trajectories are represented by magnetic field lines, composing a *magnetic* Poincaré plot.

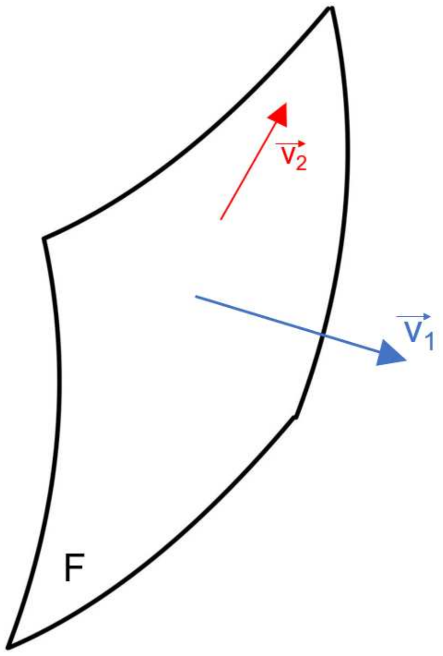

Figure 4.1: Sketch to describe the meaning of the definition of the Poincaré section. $\vec{v}_1$, represented in blue, is a good flux vector being F a Poincaré section, whereas the vector $\vec{v}_2$ represented in red is not compatible with the definition of F as a Poincaré section.

In the RFP case the Poincaré sections can be chosen in two ways. The first one is the poloidal Poincaré section, obtained by cutting the torus with a poloidal plane, as shown in Fig. 4.2a. The resulting plot lies in the $\theta - r$ plane, but the reversal surface can not be included in the plot since it is a tangent trajectory. Alternatively, is possible to cut the torus with a toroidal plane, obtaining a toroidal Poincaré plot in the $\varphi - r$ plane as shown in Fig. 4.2b. In the toroidal Poincaré plot it is not possible to include the axis at $r = 0$.

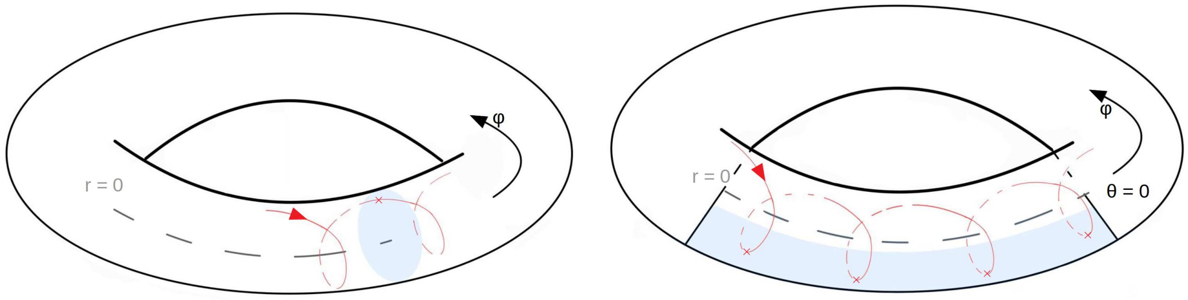

(a) Example of a poloidal Poincaré plot.

(b) Example of a toroidal Poincaré plot on the equatorial plane $\theta = 0$.

Figure 4.2: Construction of the two available kinds of Poincaré plots (coloured in blue) for a toroidal geometry like the one of the RFX-mod. The red arrow indicates a generic magnetic field line. The intersection between such a field line and the Poincaré section is indicated with a × symbol.

4.2 Poincaré plot in RFX-mod during #29324 at $t = t_{PWI}$

In Fig. 4.3 a toroidal Poincaré plot at $\theta = 0$ collects the magnetic topology of the plasma, simulated with the ORBIT code, during the discharge # 29324 at the crash time instant $t_{PWI} = 218$ ms. The points coloured in magenta were deposited inside the $m = 1$, $n = 7$ islands. The points in cyan were deposited on the reversal surface.

The description of such a Poincaré plot can be divided into three regions:
The **internal region** ($r \in [0, \approx 25]$) is populated by the magnetic islands associated with the $m = 1$, $n = 7$ mode. Notice that they are located around the same radial position, $r \approx 15$ cm, which is compatible with the radial position of the corresponding magnetic surface at $q_{1,7}$ already sketched in Fig. 3.3. The toroidal dimension of such islands is of the order of one meter, as can be seen by comparing with the distance indicated with the bar reported in the graph. Whereas, in the radial direction, these islands are of the order of ≈ 10 cm.

The **mid-radius region** ($r \in [\approx 25, \approx 35]$) is where secondary modes resonate. The chaos characterising this region is the main consequence of the magnetic islands overlap [85] due to their locking. The mechanism leading to the chaos formation is totally analogous to the one of Tokamaks as already reported in the Section 1.7.2.
On purpose, a largely used in Tokamaks, useful parameter to quantitatively describe the chaos condition is the *Chirikov parameter*, c . Assume a standard map, i.e. consider a simplified scheme of two adjacent magnetic islands which share same resonance and same helicity $m = 1$, $n = 1$. Given r_i and r_j as the radial positions of the O-points, their reciprocal distance is given by:

$$d_O = |r_j - r_i| \ . \tag{4.3}$$

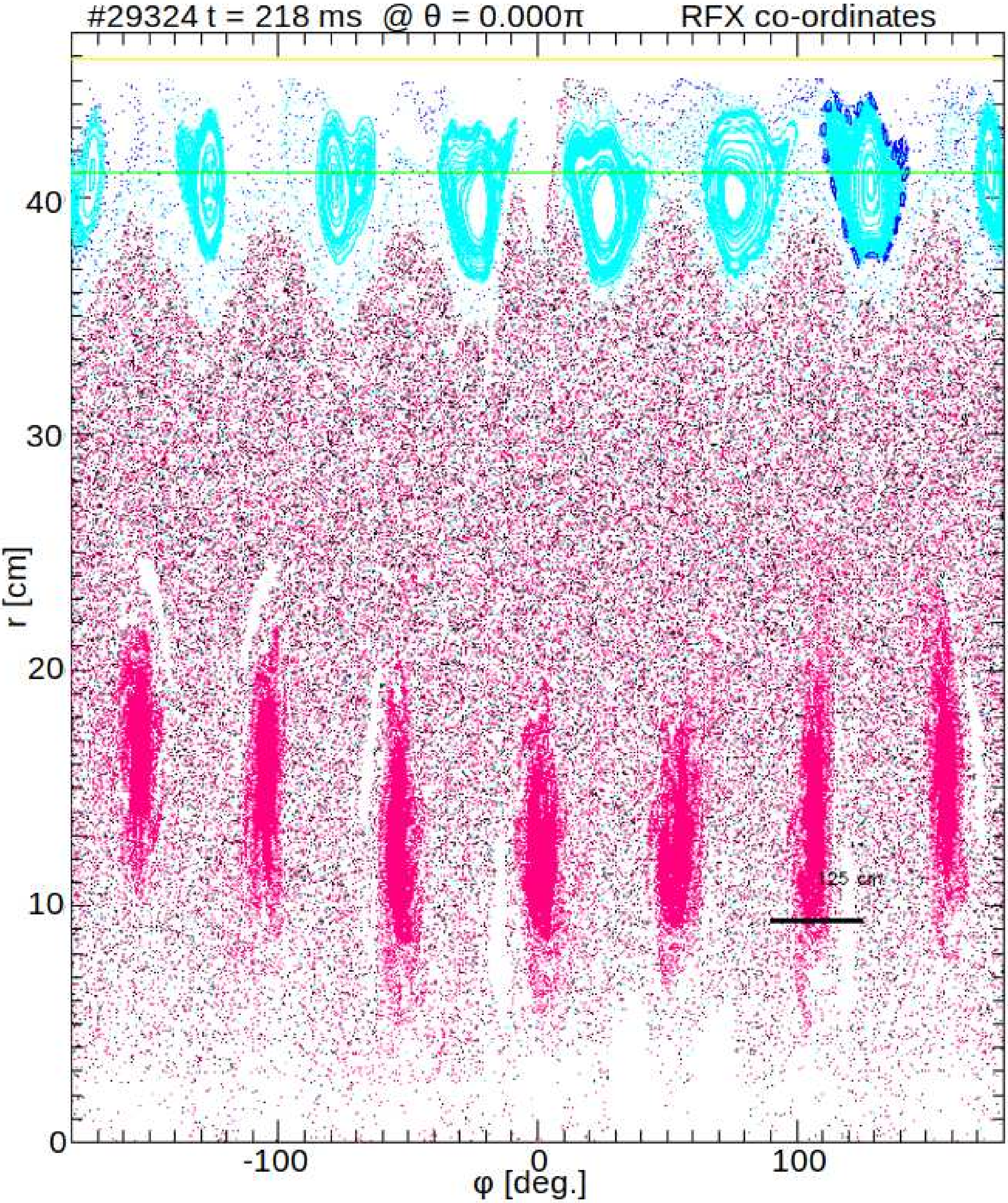

Figure 4.3: Toroidal Poincaré plot representing the magnetic topology during the shot #29324 at the crash time instant $t = t_{PWI}$. Each point corresponds to a magnetic field line crossing the equatorial plane $\theta = 0$. Magenta points refer to the $m = 1$ modes, whereas the cyan ones refer to $m = 0$ modes. The black bar indicates a distance of 125 cm. The points which are represented in blue highlight a set of smaller magnetic islands around an $m = 0$ one. They are the confirmation that the arrangement of the magnetic islands is actually much more complicated of the level of the description reported in this Chapter of the thesis since also the possible several interactions between modes have to be taken into account while describing the overall magnetic topology. The horizontal green line represents the position of the reversal surface, around which $m = 0$ magnetic islands are located. The horizontal yellow line indicates the position of the device wall.

Furthermore, consider w_i and w_j as the widths of the magnetic islands i and j respectively, according to what already illustrated in Fig. 1.12.

Therefore, the condition for the magnetic islands overlap, resulting in chaos, occurs when:

$$d_O < \frac{w_i + w_j}{2} \ . \tag{4.4}$$

Then, the *Chirikov parameter* is defined as follows:

$$c = \frac{w_i + w_j}{2 \cdot d_O} = \frac{w_i + w_j}{2 \cdot |r_i - r_j|} \ , \tag{4.5}$$

and chaos condition corresponds to $c > 1$. Actually, since it can be shown that we are near the stochastic threshold $c \approx 1$ [69], the Chirikov parameter provides only a qualitative understanding of the local presence of chaos regions in plasma in RFX-mod.

The overall physical interpretation of the description of the internal and the central part of the Poincaré plot in Fig. 4.3 is that, despite the secondary modes locking resulting in chaos, radially enclosed into the central region of the plasma, the magnetic helicity characterising the plasma is still well-defined and coincides with the one imposed by the $m = 1$, $n = 7$ mode indeed. This result is compatible with the one already provided in the previous Chapter, as summarised by Figs. 2.5-3.5d.

The Poincaré plot provides a much more detailed description of the PWI than the one reported in the previous Chapter. In the outermost **edge region** ($r > 35$ cm) corresponding to the reversal surface, positioned at $r \approx 42$ cm (as already indicated in Fig. 3.3), a set of seven $m = 0$ magnetic islands is present during the discharge. Their dimensions are reduced by a factor $\varepsilon = A^{-1}$ with respect to the $m = 1$ islands. The existence of such islands can be explained as the main consequence of the *toroidal coupling* [64] between the dominant mode ($m = 1$, $n = 7$) with a mode ($m = 1$, $n = 0$) corresponding to a radial shift of the magnetic surfaces, called *Shafranov shift*, which is due to the toroidal geometry of the device. It can be demonstrated that the resulting modes from such coupling are the $m = 2$, $n = 7$ mode, which does not appear in the Poincaré plot because it is not resonating since $m/n = 2/7 \approx 0.28 > q_0$, and the mode characterised by $m = 0$, $n = 7$, which is the one that appears in Fig. 4.3. Moreover, since the $m = 1$, $n = 7$ mode dominates over the other $m = 1$ modes (the plasma is in the QSH state, see Fig. 2.5), it is expected that also the $m = 0$ mode resulting from its coupling with the Shafranov shift dominates over the others $m = 0$ modes. This explains why the magnetic islands appearing in the reversal surface share the same helicity of the dominant mode.

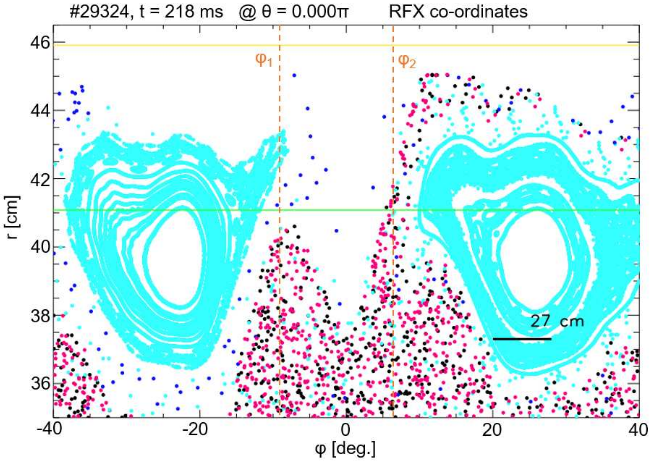

Figure 4.4: Zoom of the Poincaré plot already reported in Fig. 4.3 in proximity to the region where the PWI of interest is observed. Two stripes of points, correspondingly to a set of magnetic field lines, which overcome the barrier of the $m = 0$ islands, is effectively observed. The orange dashed vertical lines highlight the first two maxima of the ideal displacement Δ_{sec}.

In Fig. 4.4 is reported a zoom of the previous Poincaré plot in the outer region. It shows two bundles of points protruding from the chaotic sea to the plasma boundary. The convolution of these points resembles the two maxima of the ideal displacement already shown in Fig. 3.8b, confirming that the use of Δ_{sec} is justified as a first approximation of the pattern of PWI. Not only, as in the case of the ideal displacement profile, the positions of the two stripes also differ from the ones experimentally measured in Ref. [73]. The reason is the same since also the ORBIT simulation, from which the

Poincaré plot in Fig. 4.3 is obtained, employs only the modes with $n \leq 23$. Reasonably, by following the result obtained at the end of the previous Chapter (3.16), and by properly updating the number of sensors in RFX-mod2 [86], not only a much more detailed description of the magnetic topology during the crash should be obviously obtained, but also a more precise comprehension of the chaotic mechanism leading to the PWI observed should be achieved.

The main further conclusion we can draw by looking at the magnetic topology of the plasma during the crash, and by comparing it with the methods applied in Chapter 3, is that the role of the $m = 0$ modes can not be neglected. In particular, regarding the first stripe located at $\varphi_1 = 352°$, by looking at the image in Fig. 3.1, it is visible that the width of the deformation touching the wall is a little bit larger than the one at $\varphi_2 = 7°$. As a consequence, whereas the stripe at φ_2 can be associated with the $m = 1$ LM, the stripe at $\varphi_1 = 352°$ can be probably ascribed to the nearest $m = 0$ island.
Such an argument suggests the need for some new methods in order to achieve a better understanding of the mechanism leading to the occurrence of a PWI event with such a shape. One of these methods, based on the calculation with Orbit of the Connection Length $L_{c,w}$, is the topic of the next Chapter.

Chapter 5

The Connection Length

In this Chapter we present a further level of comprehension of the PWI event at $t_{PWI} = 218$ ms *by using the Connection Length to the wall. The parameter* $L_{c,w}$ *is calculated with* ORBIT *both in the* φ-r *plane and in the* φ-θ *plane. A comparison with the Poincaré plot introduced in the previous Chapter is discussed. The image of PWI is then associated with the 2D profile of the* $L_{c,w}(\varphi, \theta)$ *map. Results coming from previous analyses in Chapters 3 and 4 are confirmed and completed.*

5.1 $L_{c,w}(\varphi, r)$ map and the magnetic topology

The main result of the previous Chapter was that from the analysis of the magnetic topology, the two footprints of the PWI at $t_{PWI} = 218$ms might have different causes. In particular, the second one, at $\varphi_2 = 7°$ is the consequence of the $m = 1$ secondary mode locking. On the contrary, the first one, located at $\varphi_1 = 352°$, might be associated with a 'tail' of the nearest $m = 0$ island. This is suggested by the observation that in Fig. 3.1 the first stripe at φ_1 is broader than the second one at φ_2. In order to validate this argument, further investigation is needed.

The Connection Length to the wall, $L_{c,w}(\psi_{p,0}, \theta_0, \zeta_0)$, of a certain point A of coordinates $(\psi_{p,0}, \theta_0, \zeta_0)$ represents the distance that is travelled by a plasma particle from A to the wall. The meaning of such a quantity has been already discussed in Boozer coordinates in Section 2.2.3. Let us recall the formal definition provided in Eq. (2.24):

$$L_{c,w}(\psi_{p,0}, \theta_0, \zeta_0) = \int_{\zeta_0}^{\zeta_w} \frac{B\,\mathrm{d}\zeta}{\vec{B} \cdot \nabla\zeta} \,. \tag{5.1}$$

It is worth underlining that such a distance is calculated *along the magnetic field line* since the meaning of the scalar product present in the equation above is a projection of the particle orbit (which is a spiral around the magnetic field line itself) on the direction parallel to the one of the magnetic field $\vec{B}$. Through the definition in Eq. (5.1), each point of the space is uniquely associated with a certain value of the $L_{c,w}$ parameter in such a way each point of the spatial region occupied by plasma can be mapped in terms of Connection Length to the wall. Thus it quantitatively describes the plasma magnetic topology.

A comparison between the $L_{c,w}$ map and the Poincaré plot in the φ-r plane (the poloidal coordinate is fixed at $\theta = 0$) near the region where the PWI at $t_{PWI} = 218$ ms occurred is illustrated in Fig. 5.1. In the RFP, shorter connection lengths correspond to particles jumping from the plasma core to the wall in a very short time [69]. The toroidal position of the LM is a preferential channel of increased particle losses and short connection lengths, as already shown with ORBIT in the past [73, 87]. By looking at the regions where the $L_{c,w}$ is lower, one can therefore easily associate them with the regions at larger PWI. Such regions are coloured in red in the figure. The Poincaré plot is then over-plotted to provide a full sight of the plasma magnetic topology.

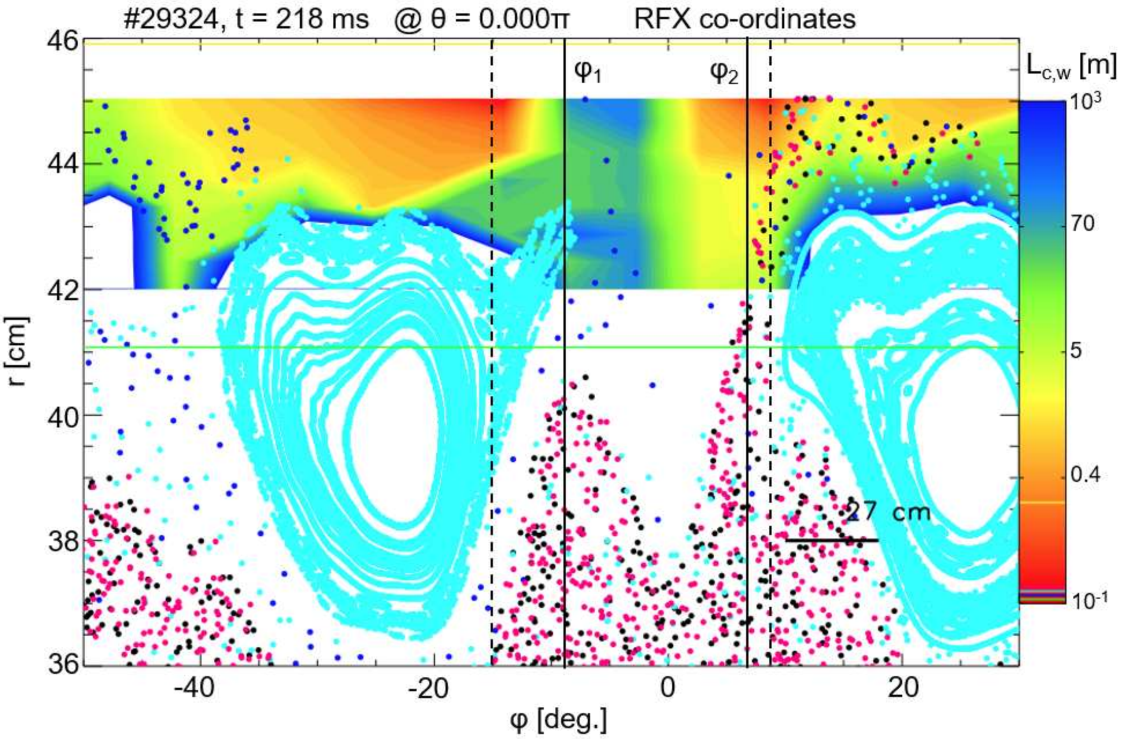

Figure 5.1: Comparison between the $L_{c,w}(\varphi,\theta)$ map and the Poincaré plot in the φ-r plane near the region where the PWI at $t_{PWI} = 218$ ms occurred. Regions coloured in red are characterised by low $L_{c,w}$ (of the order of magnitude of 10^{-1} m). Whereas, the regions where $L_{c,w}$ is high (of the order of magnitude of 1 km) are coloured in blue. The toroidal angles of the two PWI stripes observed with the OCS of RFX-mod, φ_1 and φ_2 are highlighted with two solid lines. Dashed lines indicate the toroidal angles where $L_{c,w}$ is at minimum.

By looking at Fig. 5.1, three main zones can be horizontally distinguished:
To the **right** ($\varphi \in [0, \approx 10]$), there is the region corresponding to the second PWI stripe, the one at $\varphi_2 = 7°$, as the low level of $L_{c,w}$ (of the order of magnitude of 10^{-1} m) confirms. To the **left** ($\varphi \in [\approx -45°, \approx -5°]$), there is the region associated with the second stripe of the PWI at $\varphi_1 = 352°$. In this case, not only the pattern of the $L_{c,w}$ map confirms that the interaction between plasma and the PFC is spatially wider than the one of the second stripe, but also makes explicit that particles which are responsible for this interaction come from the $m = 0$ magnetic island. Another observation regards the fact that, also in this case, the positions around which the red regions are centered (i.e. where $L_{c,w}$ is at minimum) are not compatible with the toroidal positions measured for PWI, φ_1 and φ_2. In fact, since the Connection Length is calculated by using ORBIT from experimental data, only the modes up to $n = 23$ are considered for calculations. This is a further confirmation that in order to have a total comprehension of the PWI of interest, more modes would have been given as input to ORBIT.
Finally, the **central** one ($\varphi \in [\approx -5, 0]$) is a region characterised by high $L_{c,w}$ (of the order of magnitude of 1 km), so it is populated by particles that reached the wall only after a very long time.

5.2 Description of the $L_{c,w}(\varphi, \theta)$ map

In order to find an explanation of such a $L_{c,w}$ map, one can look at the connection lengths on the nearest φ-θ plane to the edge (r is set at 0.45 m, so only almost 1 cm far from the device's first wall). Such a map is shown in Fig. 5.2.

The Fig. 5.2 represents an arrangement of regions with high and low $L_{c,w}$ analogous to the one already described in the previous Section. By looking at the poloidal coordinate $\theta = 0$, the positions of the

two stripes of interaction can be approximately located at: $\varphi_1^{Lcw} = -15°$, and $\varphi_2^{Lcw} = 8°$. They are highlighted with vertical white lines. Their mutual distance is not compatible with the ones experimentally measured in Ref. [73], $\Delta\varphi_S = 15°$, as previously shown by the Fig. 5.1.
However, in the case of the figure above, more details can be appreciated, for example, the fact that the two red regions (corresponding to the regions of interaction between the plasma and the first wall) do not follow the same slope. And this is a consequence of the fact that the two stripes of the interaction had two different topological causes, i.e. they came from modes characterised by a different helicity.

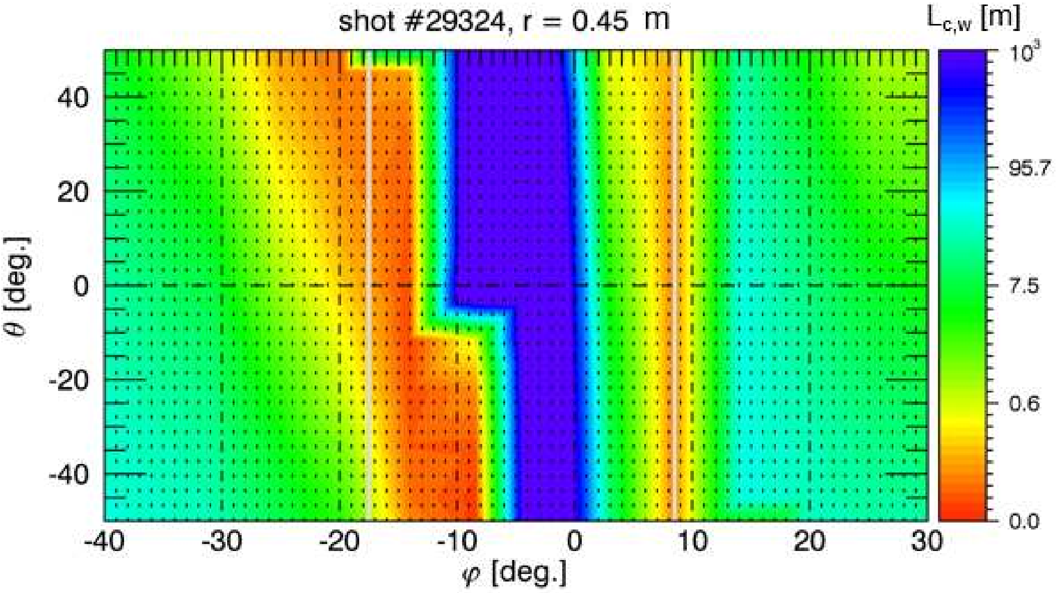

Figure 5.2: $L_{c,w}$ map at fixed $r = 45.1$ cm. The red regions indicate where the Connection Length is low (of the order of magnitude of 10^{-1} m). In blue those regions where $L_{c,w}$ is maximised (of the order of magnitude of 1 km) are represented. The vertical white line indicates the position of the PWI at $\theta = 0$.

Furthermore, regarding the central region, characterised by high $L_{c,w}$, it can be interpreted as the main effect of a process that is analogous to the one leading to homoclinic tangles in Tokamaks. They were described in Section 1.7.2. In this sense, the blue region (high $L_{c,w}$) and the red region at $\varphi_2 = 7°$ (low $L_{c,w}$) could correspond respectively to the unstable and stable manifolds of the homoclinic tangle which drove the chaos leading to the localised loss of particle to the first wall. Therefore, we speculate that the first of the two secondary $m = 1$ modes major ideal displacements we have shown in 3.8b at $\varphi < 0$, namely the one we have initially assumed to be the cause of the second stripe of the PWI of interest, was actually located in such a central region.

5.3 $L_{c,w}(\varphi, \theta)$ map and PWI footprints

The main advantage of the use of the connection length is the possibility to compare directly with the pattern of the PWI measured by the fast cameras. This type of analysis is customary in the Tokamak community, where maps of $L_{c,w}$ are compared to the PWI pattern, generated by RMPs in order to optimise the current in the coils [27, 72]. Such a comparison for RFX-mod is reported in Fig. 5.3.
In Fig. 5.3a the image of the interaction already shown in Fig. 3.1 has been projected in the φ-θ plane. The red zones represent the two stripes of the PWI, i.e. those characterised by a higher intensity of the emitted Carbon radiation. The data plotted come directly from the output of the CCD electronics, so the scale is in arbitrary units. Instead, the graph shown in 5.3b is the same as the one shown in Fig. 5.2. The toroidal angles where the red zones are centered are shifted, this can be mainly associated to the image wrapping from which the Fig. a has been obtained.

The patterns in experiment and simulation are qualitatively the same, being divided into the three main regions already described in the previous Section. The two black lines show that the helicity of each interaction stripe almost coincides with that of the related red zone in the $L_{c,w}$ map. This is a further confirmation of the fact the two stripes are the consequence of the interaction towards the first wall of the $m = 0$ island, and the locking of the secondary $m = 1$ modes, respectively.

To conclude, the PWI stripe associated with the secondary $m = 1$ modes locking is located in the red zone to the right where $L_{c,w}$ is low. The zone occupied by the 'unstable manifold' of a homoclinic tangle, characterised by high $L_{c,w}$ and coloured in blue is in the central part of the map. On the left there is a second red region with low $L_{c,w}$ which corresponds to the PWI stripe of the $m = 0$, $n = 7$ island.

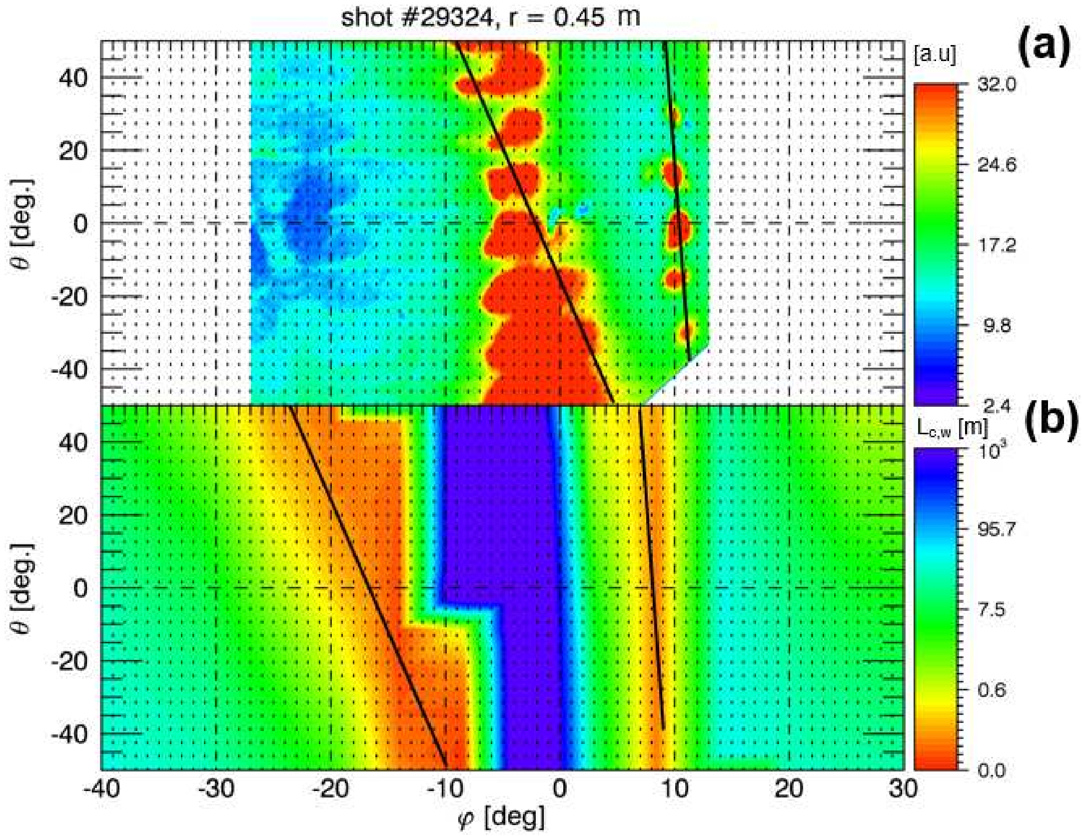

Figure 5.3: Comparison between **(a)** the PWI image taken with the OCS of RFX-mod in #29324 at $t = t_{PWI}$ and visualised through image wrapping [73] and **(b)** the $L_{c,w}$ map in the φ-θ plane, at $r = 45.1$ cm. In **(a)**, the red regions are those characterised by more intense radiation. In **(b)** red and blue regions represent respectively low and high connection lengths, such that regions with the same colours coincide in the two graphs. The black lines follow the inclination of the stripes in both **(a)** and **(b)**. They are added to help the comparison between the two patterns.

Summary and conclusions

This thesis is devoted to the study of the Plasma Wall Interaction (PWI) observed with the fast cameras system of the RFX-mod device (Fig. 3.1), during the shot #29324 at time $t_{PWI} = 218$ ms. Such an image of the PWI was already reported in a paper by Scarin *et al.* [73]. The discharge is characterised by two footprints located at $\varphi_1 = 352°$ and $\varphi_2 = 7°$. The main goal has been to estimate which modes are the most involved in determining the PWI pattern. The techniques used are the same as those used in the tokamak community to analyse the PWI footprints left by the Resonant Magnetic Perturbations (RMPs). The topic is relevant in the nuclear fusion community in perspective of ITER.

A preliminary analysis aims at providing an overall description of the discharge characteristics at the PWI time instant. It has been found that the shot #29324 is a high plasma current regime with a long lasting flat-top with a duration of almost 200 ms (Fig. 3.2). The plasma shows a strong helical state (QSH) with poloidal and toroidal mode numbers $m = 1$, $n = 7$ (Fig. 2.5). However, several back transition from the helical state to magnetic chaos are observed (Fig. 3.4) due to discrete reconnection events (DRE). During these events, the secondary modes with $m = 1$ and $n > 7$ align their phases in a bulge protruding towards the wall, called Locked Mode (LM, see Fig. 3.5d). The LM causing the PWI of interest is correlated with a minor crash, since the QSH state survives despite the secondary mode increase. This is obviously of interest for studies in the reversed-field pinch configuration, since the QSH state is a high-confinement condition which is foreseen for a possible RFP reactor [14, 38].

The original analysis presented in this thesis is structured along three levels of increasing complexity:

- The first part of the analysis introduces a simplified description of the LM as the sum of the secondary mode ideal displacements Δ_{sec}. In particular, it was possible to compare the toroidal positions of the PWI stripes with the Locking Strength parameter, defined as in Equation (3.7). The comparison of the LS with Δ_{sec}, (Fig. 3.8), leads to the conclusion that more modes are needed to explain the PWI shape than those observed experimentally, $0 < n \leq 23$. Toroidal mode numbers up to $n_{max} = 41$ (3.16) need to be included.
- The Poincaré plot obtained with the guiding center code Orbit (Fig. 4.3) provides a further level of analysis, through the direct visualisation of the magnetic field line topology. This improves the previous description by taking into account the presence of *magnetic islands*. Some features of previous analysis are confirmed: the persistence of the QSH state despite the crash, the occurrence of the secondary mode LM, and the presence of two "bundles" of field lines protruding from the chaotic sea to the plasma boundary. The envelope of the two bundles follows quite well the profile of Δ_{sec} (Fig. 4.4), consistently with the previous analysis. At the same time, more information is added: the first stripe of PWI at φ_1, which is broader than the second one at φ_2 in Fig. 3.1, is caused by a tail of the nearest $m = 0$, $n = 7$ magnetic island.
- The third level of description involves the Connection Length to the wall $L_{c,w}$. This is calculated with Orbit and mapped on the equatorial plane at $\theta = 0$ together with the Poincaré plot. In this way, a complete description of the magnetic topology at $t_{PWI} = 218$ ms is provided in Fig. 5.1. This plot, complemented with the contour of $L_{c,w}$ in the φ-θ plane, allows to draw the following conclusions:
    - The region related to the first large stripe of PWI at $\varphi_1 = 352°$ in the camera image is

characterised by short connection lengths (of the order of 10^{-1} m), and it is associated with the $m = 0$, $n = 7$ island;

- The region related to the second stripe at $\varphi_2 = 7°$, is also characterised by short connection lengths, and it is associated with the secondary mode locking (LM). It is found to correspond to the second maximum of Δ_{sec} in Fig. 3.8b at $\varphi > 0$;
- The region in between the two stripes in the camera image is on the contrary characterised by long connection lengths, $L_{c,w} \approx 1$ km. We associate it with the 'unstable manifold' of the homoclinic tangle generated by the LM. It corresponds to the first maximum of Δ_{sec} in Fig. 3.8b at $\varphi < 0$.

The analysis presented in this thesis can be improved in the future RFX-mod2 device [48] which is expected to operate starting from mid 2024. In particular, the pattern of $L_{c,w}$ calculated with ORBIT is systematically wider than the stripes in the camera image, see Figure 5.3. This has been explained in the thesis as being due to the limited resolution of the 48-element array of pickup probes installed on RFX-mod [49]: the present system allows to calculate a spectrum of tearing modes with $0 \leq n \leq 23$ [64]. In the RFX-mod2 device a set of 6 (poloidal) × 72 (toroidal) pickup sensors will be available [86], allowing for calculating modes with $m = 0, 1, 2$ and $0 \leq n \leq 35$. In addition to this, an improved optical camera system (OCS) of 7 fast cameras covering 70% of the wall will be installed, allowing for a better experimental characterization of the PWI.

Finally, it is planned to improve ORBIT simulations by adding a module that calculates the power load pattern of thermal ions at $r = a$, considering the motion of thermal ions instead of magnetic field lines. This will allow a direct comparison of maps of power load (in $\mathrm{MW/m^2}$) with the camera images.

Bibliography

[1] The demonstration power plant: DEMO (EUROfusion official website), URL `https://www.euro-fusion.org/programme/demo/`.

[2] R. B. White and M. S. Chance, The Physics of Fluids **27**, 2455 (1984), `http://aip.scitation.org/doi/pdf/10.1063/1.864527`, URL `http://aip.scitation.org/doi/abs/10.1063/1.864527`.

[3] N. Ghaharamany, S. Gharaati, and G. M., Journal of Theoretical and Applied Physics **6** (2012), URL `https://doi.org/10.1186/2251-7235-6-3`.

[4] J. Freidberg, *Plasma Phusucs and Fusion Energy* (Cambridge University Press, The Edinburgh Building, Cambridge CB2 8RU, UK, 2007), chap. 2.3, pp. 23–24, ISBN 978-0-521-85107-7, URL `www.cambridge.org/9780521851077`.

[5] S. Glasstone and R. Lovberg, *Controlled Thermonuclear Reactions* (Robert E. Krieger Publishing, New York, 1975), chap. 2.6, pp. 16–19, ISBN 0-88275-326-6.

[6] J. Freidberg, *Plasma Physics and Fusion Energy* (Cambridge University Press, The Edinburgh Building, Cambridge CB2 8RU, UK, 2007), chap. 1.3.1, pp. 16–18, ISBN 978-0-521-85107-7, URL `www.cambridge.org/9780521851077`.

[7] M. Rubel, Journal of Fusion Energy **38**, 315 (2019), URL `https://doi.org/10.1007/s10894-018-0182-1`.

[8] J. Wesson, *Tokamaks* (Oxford University Press, Great Clarendon Street, Oxford OX2 6DP, 2004), chap. 1.4, pp. 8–10, 3rd ed., ISBN 0-19-8509227.

[9] M. Kikuchi, K. Lackner, and M. Q. Tran, *Fusion Physics* (International Atomic Energy Agency (IAEA), P. O. Box 100, 1400 Vienna, Austria, 2012), chap. 1.3.2, pp. 17–20, ISBN 978-92-0-130410-0, URL `http://www-pub.iaea.org/MTCD/Publications/PDF/Pub1562_web.pdf`.

[10] J. Wesson, *Tokamaks* (Oxford University Press, Great Clarendon Street, Oxford OX2 6DP, 2004), chap. 1.5, pp. 10–15, 3rd ed., ISBN 0-19-8509227.

[11] T. Fujita, Y. Kamada, S. Ishida, Y. Neyatani, T. Oikawa, S. Ide, S. Takeji, Y. Koide, A. Isayama, T. Fukuda, et al., Nuclear Fusion **39**, 1627 (1999), URL `https://dx.doi.org/10.1088/0029-5515/39/11Y/302`.

[12] H. Alfvén, *Cosmical Electrodynamics* (Clarendon Press, Oxford, 1950), chap. 2, pp. 13–36, URL `https://archive.org/details/AlfvenCosmicalElectrodynamics/mode/2up`.

[13] J. Freidberg, *Plasma Physics and Fusion Energy* (Cambridge University Press, The Edinburgh Building, Cambridge CB2 8RU, UK, 2007), chap. 8.3.3, pp. 146–147, ISBN 978-0-521-85107-7, URL `www.cambridge.org/9780521851077`.

[14] L. Marrelli, P. Martin, M. Puiatti, J. Sarff, B. Chapman, J. Drake, D. Escande, and S. Masamune, Nuclear Fusion **61**, 023001 (2021), URL `https://doi.org/10.1088/1741-4326/abc06c`.

[15] A. H. Boozer, Physics of Plasmas **5**, 1647 (1998), `https://doi.org/10.1063/1.872833`, URL `https://doi.org/10.1063/1.872833`.

[16] YouJun Hu's Homepage, URL https://youjunhu.github.io/.

[17] J. Wesson, *Tokamaks* (Oxford University Press, Great Clarendon Street, Oxford OX2 6DP, 2004), chap. 3.4, pp. 111–115, 3rd ed., ISBN 0-19-8509227.

[18] J. Freidberg, *Ideal MHD* (Cambridge University Press, The Edinburgh Building, Cambridge CB2 8RU, UK, 2014), chap. 8.11.4, pp. 373–374, ISBN 978-1-107-00625-6.

[19] G. Bateman, *MHD instabilities / Glenn Bateman* (MIT Press, Cambridge, Mass. : USA, 1978), p. 192, ISBN 0262021315.

[20] M. Rosenbluth, R. Sagdeev, J. Taylor, and G. Zaslavski, Nuclear Fusion **6**, 297 (1966), URL http://stacks.iop.org/0029-5515/6/i=4/a=008.

[21] F. Troyon, R. Gruber, H. Sauremann, S. Semenzato, and S. Succi, Plasma Physics and Controlled Fusion **26**, 209 (1984), URL https://doi.org/10.1088/0741-3335/26/1a/319.

[22] M. Greenwald, J. Terry, S. Wolfe, S. Ejima, M. Bell, S. Kaye, and G. Neilson, Nuclear Fusion **28**, 2199 (1988), URL https://doi.org/10.1088/0029-5515/28/12/009.

[23] M. Puiatti, P. Scarin, G. Spizzo, M. Valisa, M. Agostini, A. Alfier, A. Canton, L. Carraro, E. Gazza, R. Lorenzini, et al., Nuclear Fusion **49**, 045012 (2009), URL https://doi.org/10.1088/0029-5515/49/4/045012.

[24] T. Pütterich, E. Wolfrum, R. Dux, and C. F. Maggi (ASDEX Upgrade Team), Phys. Rev. Lett. **102**, 025001 (2009), URL https://link.aps.org/doi/10.1103/PhysRevLett.102.025001.

[25] F. Wagner, G. Becker, K. Behringer, D. Campbell, A. Eberhagen, W. Engelhardt, G. Fussmann, O. Gehre, J. Gernhardt, G. v. Gierke, et al., Phys. Rev. Lett. **49**, 1408 (1982), URL https://link.aps.org/doi/10.1103/PhysRevLett.49.1408.

[26] F. Nguyen, P. Ghendrih, and A. Grosman, Nuclear Fusion **37**, 743 (1997), URL http://stacks.iop.org/0029-5515/37/i=6/a=I03.

[27] O. Schmitz, M. Jakubowski, H. Frerichs, D. Harting, M. Lehnen, B. Unterberg, S. Abduallaev, S. Brezinsek, I. Classen, T. Evans, et al., Nuclear Fusion **48**, 024009 (2008), URL http://stacks.iop.org/0029-5515/48/i=2/a=024009.

[28] T. E. Evans, R. K. W. Roeder, J. A. Carter, and B. I. Rapoport, Contributions to Plasma Physics **44**, 235 (2004), URL http://dx.doi.org/10.1002/ctpp.200410034.

[29] T. E. Evans, Plasma Physics and Controlled Fusion **57**, 123001 (2015), URL https://dx.doi.org/10.1088/0741-3335/57/12/123001.

[30] H. Moffatt, Journal of Fluid Mechanics **35**, 117 (1969).

[31] L. Woltjer, Proceedings of the National Academy of Sciences **44**, 489 (1958), http://www.pnas.org/content/44/6/489.full.pdf+html, URL http://www.pnas.org/content/44/6/489.short.

[32] V. Antoni and S. Ortolani, The Physics of Fluids **30**, 1489 (1987), https://aip.scitation.org/doi/pdf/10.1063/1.866262, URL https://aip.scitation.org/doi/abs/10.1063/1.866262.

[33] M. Abramowitz and I. A. Stegun, *Handbook of Mathematical Functions* (National Bureau of Standards, Washington D.C., USA, 1972), p. 361, Applied Mathematics Series, tenth ed., URL http://people.math.ubc.ca/~cbm/aands/page_361.htm.

[34] S. Ortolani, in *Proceedings of the International School of Plasma Physics, Course on Mirror-based and Field-reversed Approaches to Magnetic Fusion, Varenna, Italy*, edited by R. Pozzoli and E. Sindoni (Monotypia Franchi, Città di Castello, 1983), vol. 2, p. 513.

[35] D. F. Escande, S. Cappello, F. D'Angelo, P. Martin, S. Ortolani, and R. Paccagnella, Plasma Physics and Controlled Fusion **42**, B243 (2000), URL https://doi.org/10.1088/0741-3335/42/12b/319.

[36] S. Ortolani and D. D. Schnack, *Magnetohydrodynamics of Plasma Relaxation* (World Scientific Publishing Co. Pte. Ltd., P. O. Box 128, Farrer Road, Singapore 9128, 1993), ISBN 981-02-0860-X.

[37] R. Lorenzini, M. Agostini, A. Alfier, V. Antoni, L. Apolloni, F. Auriemma, O. Barana, M. Baruzzo, P. Bettini, D. Bonfiglio, et al., Physics of Plasmas **16**, 056109 (2009), URL https://doi.org/10.1063/1.3082821.

[38] R. Lorenzini, E. Martines, P. Piovesan, D. Terranova, P. Zanca, M. Zuin, A. Alfier, D. Bonfiglio, F. Bonomo, A. Canton, et al., Nature Physics **5**, 570 (2009), URL https://doi.org/10.1038/nphys1308.

[39] M. Gobbin, D. Bonfiglio, D. F. Escande, A. Fassina, L. Marrelli, A. Alfier, E. Martines, B. Momo, and D. Terranova, Phys. Rev. Lett. **106**, 025001 (2011), URL https://link.aps.org/doi/10.1103/PhysRevLett.106.025001.

[40] G. Spizzo, G. Pucella, O. Tudisco, M. Zuin, M. Agostini, E. Alessi, F. Auriemma, W. Bin, P. Buratti, L. Carraro, et al., Nuclear Fusion **55**, 043007 (2015), URL http://stacks.iop.org/0029-5515/55/i=4/a=043007.

[41] M. Gobbin, M. Agostini, F. Auriemma, L. Carraro, R. Cavazzana, A. Fassina, P. Franz, L. Marrelli, B. Momo, R. Piovan, et al., Nuclear Fusion **62**, 026030 (2022), URL https://doi.org/10.1088/1741-4326/ac39f2.

[42] L. Piron, L. Grando, G. Marchiori, L. Marrelli, P. Piovesan, A. Soppelsa, and D. Terranova, Nuclear Fusion **51**, 063012 (2011), URL https://doi.org/10.1088/0029-5515/51/6/063012.

[43] G. Rostagni, Fusion Engineering and Design **25**, 301 (1995), ISSN 0920-3796, URL http://www.sciencedirect.com/science/article/pii/092037969400362B.

[44] F. Gnesotto, P. Sonato, W. Baker, A. Doria, F. Elio, M. Fauri, P. Fiorentin, G. Marchiori, and G. Zollino, Fusion Engineering and Design **25**, 335 (1995), ISSN 0920-3796, URL https://www.sciencedirect.com/science/article/pii/092037969400280K.

[45] L. Marrelli, P. Zanca, M. Valisa, G. Marchiori, A. Alfier, F. Bonomo, M. Gobbin, P. Piovesan, D. Terranova, M. Agostini, et al., Plasma Physics and Controlled Fusion **49**, B359 (2007), URL http://stacks.iop.org/0741-3335/49/B359.

[46] P. Sonato, G. Chitarin, P. Zaccaria, F. Gnesotto, S. Ortolani, A. Buffa, M. Bagatin, W. Baker, S. Dal Bello, P. Fiorentin, et al., Fusion Engineering and Design **66-68**, 161 (2003), 22nd Symposium on Fusion Technology, URL https://www.sciencedirect.com/science/article/pii/S0920379603001777.

[47] S. C. Prager, A. F. Almagri, S. Assadi, J. A. Beckstead, R. N. Dexter, D. J. Den Hartog, G. Chartas, S. A. Hokin, T. W. Lovell, T. D. Rempel, et al., Physics of Fluids B: Plasma Physics **2**, 1367 (1990), https://doi.org/10.1063/1.859557, URL https://doi.org/10.1063/1.859557.

[48] L. Marrelli, R. Cavazzana, D. Bonfiglio, M. Gobbin, G. Marchiori, S. Peruzzo, M. Puiatti, G. Spizzo, D. Voltolina, P. Zanca, et al., Nuclear Fusion **59**, 076027 (2019), URL https://doi.org/10.1088/1741-4326/ab1c6a.

[49] P. Fiorentin and N. Pomaro, Fusion Engineering and Design **66-68**, 871 (2003), ISSN 0920-3796, 22nd Symposium on Fusion Technology, URL https://www.sciencedirect.com/science/article/pii/S0920379603003685.

[50] *Basler ace aca720-520um* data sheet (Basler official website), URL https://www.baslerweb.com/en/products/cameras/area-scan-cameras/ace/aca720-520um/.

[51] R. G. Littlejohn, Physics of Fluids **24**, 1730 (1981), URL `http://scitation.aip.org/content/aip/journal/pof1/24/9/10.1063/1.863594`.

[52] A. H. Boozer, The Physics of Fluids **24**, 1999 (1981), `https://aip.scitation.org/doi/pdf/10.1063/1.863297`, URL `https://aip.scitation.org/doi/abs/10.1063/1.863297`.

[53] R. B. White, G. Spizzo, and M. Gobbin, Plasma Physics and Controlled Fusion **55**, 115002 (2013), URL `http://stacks.iop.org/0741-3335/55/i=11/a=115002`.

[54] R. B. White, *The theory of toroidally confined plasmas* (Imperial College Press, 57 Shelton Street, Covent Garden, London WC2H 9HE, 2014), pp. 79–80, 3rd ed., ISBN 978-1-78326-363-9, URL `https://doi.org/10.1142/p916`.

[55] H. Goldstein, *Classical mechanics* (Addison-Wesley, Reading, Massachussets, 1980), pp. 392–393, 2nd ed., ISBN 0201029693.

[56] R. B. White, *The theory of toroidally confined plasmas* (Imperial College Press, 57 Shelton Street, Covent Garden, London WC2H 9HE, 2014), p. 78, 3rd ed., ISBN 978-1-78326-363-9, URL `https://doi.org/10.1142/p916`.

[57] R. B. White, *The theory of toroidally confined plasmas* (Imperial College Press, 57 Shelton Street, Covent Garden, London WC2H 9HE, 2014), pp. 77–79, 3rd ed., ISBN 978-1-78326-363-9, URL `https://doi.org/10.1142/p916`.

[58] M. H. Redi, R. V. Budny, D. C. McCune, C. O. Miller, and R. B. White, Physics of Plasmas **3**, 3037 (1996), `https://doi.org/10.1063/1.871640`, URL `https://doi.org/10.1063/1.871640`.

[59] R. B. White, E. Fredrickson, D. Darrow, M. Zarnstorff, R. Wilson, S. Zweben, K. Hill, Y. Chen, and G. Fu, Physics of Plasmas **2**, 2871 (1995), `https://doi.org/10.1063/1.871452`, URL `https://doi.org/10.1063/1.871452`.

[60] R. B. White, A. Bierwage, and S. Ethier, Physics of Plasmas **29**, 052511 (2022), `https://doi.org/10.1063/5.0094458`, URL `https://doi.org/10.1063/5.0094458`.

[61] R. B. White, Physics of Plasmas **20**, 022105 (2013), URL `http://scitation.aip.org/content/aip/journal/pop/20/2/10.1063/1.4791661`.

[62] R. B. White, Physics of Plasmas **20**, 042116 (2013), URL `http://scitation.aip.org/content/aip/journal/pop/20/4/10.1063/1.4802094`.

[63] S. Cappello and D. Biskamp, Nuclear Fusion **36**, 571 (1996), URL `http://stacks.iop.org/0029-5515/36/i=5/a=I05`.

[64] P. Zanca and D. Terranova, Plasma Physics and Controlled Fusion **46**, 1115 (2004), URL `https://doi.org/10.1088/0741-3335/46/7/011`.

[65] G. Ciaccio, M. Veranda, D. Bonfiglio, S. Cappello, G. Spizzo, L. Chacón, and R. B. White, Physics of Plasmas **20**, 062505 (2013), `https://doi.org/10.1063/1.4811380`, URL `https://doi.org/10.1063/1.4811380`.

[66] J. M. Finn and L. Chacón, Physics of Plasmas **12**, 054503 (pages 4) (2005), URL `http://link.aip.org/link/?PHP/12/054503/1`.

[67] R. B. White, *The theory of toroidally confined plasmas* (Imperial College Press, 57 Shelton Street, Covent Garden, London WC2H 9HE, 2014), pp. 105–107, 3rd ed., ISBN 978-1-78326-363-9, URL `https://doi.org/10.1142/p916`.

[68] M. Gobbin, L. Marrelli, and R. B. White, Plasma Physics and Controlled Fusion **51**, 065010 (14pp) (2009), URL `http://stacks.iop.org/0741-3335/51/065010`.

[69] G. Spizzo, R. B. White, S. Cappello, and L. Marrelli, Plasma Physics and Controlled Fusion **51**, 124026 (2009), URL https://doi.org/10.1088/0741-3335/51/12/124026.

[70] G. Spizzo, R. White, M. Maraschek, V. Igochine, G. Granucci, and The ASDEX Upgrade Team, Nuclear Fusion **59**, 016019 (2019), URL http://stacks.iop.org/0029-5515/59/i=1/a=016019.

[71] G. Spizzo, N. Vianello, R. B. White, S. S. Abdullaev, M. Agostini, R. Cavazzana, G. Ciaccio, M. E. Puiatti, P. Scarin, O. Schmitz, et al., Physics of Plasmas **21**, 056102 (2014), https://doi.org/10.1063/1.4872173, URL https://doi.org/10.1063/1.4872173.

[72] Y. Feng, M. Kobayashi, T. Lunt, and D. Reiter, Plasma Physics and Controlled Fusion **53**, 024009 (2011), URL http://stacks.iop.org/0741-3335/53/i=2/a=024009.

[73] P. Scarin, M. Agostini, G. Spizzo, M. Veranda, P. Zanca, and the RFX-mod team, Nuclear Fusion **59**, 086008 (2019), URL https://doi.org/10.1088/1741-4326/ab2071.

[74] T. Bolzonella and D. Terranova, Plasma Physics and Controlled Fusion **44**, 2569 (2002), URL https://doi.org/10.1088/0741-3335/44/12/306.

[75] K. Kusano, T. Tamano, and T. Sato, Nuclear Fusion **31**, 1923 (1991), URL https://doi.org/10.1088/0029-5515/31/10/010.

[76] J.-A. Malmberg, J. Brzozowski, P. Brunsell, M. Cecconello, and J. Drake, Physics of Plasmas **11**, 647 (2004), https://doi.org/10.1063/1.1639016, URL https://doi.org/10.1063/1.1639016.

[77] L. Frassinetti, Y. Yagi, H. Koguchi, T. Shimada, Y. Hirano, and H. Sakakita, Physics of Plasmas **13**, 042502 (2006), https://doi.org/10.1063/1.2188397, URL https://doi.org/10.1063/1.2188397.

[78] L. Marrelli, P. Zanca, P. Martin, S. Martini, and A. Munari, Journal of Nuclear Materials **266–269**, 877 (1999), URL https://doi.org/10.1016/S0022-3115(98)00554-6.

[79] P. Innocente, P. Zanca, M. Zuin, T. Bolzonella, and B. Zaniol, Nuclear Fusion **54**, 122001 (2014), URL https://doi.org/10.1088/0029-5515/54/12/122001.

[80] M. Valisa, T. Bolzonella, L. Carraro, E. Casarotto, S. Costa, L. Garzotti, P. Innocente, S. Martini, R. Pasqualotto, M. Puiatti, et al., Journal of Nuclear Materials **241-243**, 988 (1997), ISSN 0022-3115, URL http://www.sciencedirect.com/science/article/pii/S0022311597801791.

[81] B. Momo, H. Isliker, R. Cavazzana, M. Zuin, L. Cordaro, D. Lopez-Bruna, E. Martines, I. Predebon, C. Rea, M. Spolaore, et al., Nuclear Fusion **60**, 056023 (2020), URL https://doi.org/10.1088/1741-4326/ab7d4e.

[82] P. Fitzpatrick and P. Zanca, Physics of Plasmas **9**, 2707 (2002), URL https://aip.scitation.org/doi/10.1063/1.1481057.

[83] H. Zohm, *Magnetohydrodynamic Stability of Tokamaks* (Wiley-VCH Verlag GmbH & Co. KGaA, 2014), chap. 8.2, pp. 127–134, ISBN 978-3-527-67737-5, URL http://dx.doi.org/10.1002/9783527677375.

[84] J. Barrow-Green, *Poincaré and the Three Body Problem* (American Mathematical Society, P. O. Box 6248, Providence, Rhode Island (USA), 1997), vol. 11 of *History of Mathematics*, chap. 3, p. 38, ISBN 978-0-8218-0367-7, URL https://bookstore.ams.org/hmath-11.

[85] B. V. Chirikov, Physics Reports **52**, 263 (1979), URL https://www.sciencedirect.com/science/article/pii/0370157379900231.

[86] N. Marconato, P. Bettini, R. Cavazzana, L. Grando, G. Marchiori, L. Marrelli, S. Peruzzo, and N. Pomaro, Fusion Engineering and Design **146**, 906 (2019), ISSN 0920-3796, sI:SOFT-30, URL https://www.sciencedirect.com/science/article/pii/S092037961930122X.

[87] G. Spizzo, S. Cappello, A. Cravotta, D. F. Escande, I. Predebon, L. Marrelli, P. Martin, and R. B. White, Physical Review Letters **96**, 025001 (pages 4) (2006), URL http://link.aps.org/abstract/PRL/v96/e025001.